

Title	Development of ASICs for multi-readout X-ray CCDs
Author(s)	Matsuura, Daisuke
Citation	大阪大学, 2009, 博士論文
Version Type	VoR
URL	https://hdl.handle.net/11094/23460
rights	
Note	

Osaka University Knowledge Archive : OUKA

<https://ir.library.osaka-u.ac.jp/>

Osaka University

Development of ASICs for multi-readout X-ray CCDs

Daisuke Matsuura

Department of Earth and Space Science, Graduate School of Science,
Osaka University, Japan

March 6, 2009

Development of ASICs for multi-readout X-ray CCDs

Daisuke Matsuura

Department of Earth and Space Science, Graduate School of Science,
Osaka University, Japan

March 6, 2009

Abstract

An X-ray Charge-Coupled Device (CCD) is a 2 dimensional array of small pixels whose size of $10 \sim 150 \mu\text{m}^2$. We can determine the energy of incident X-ray photons if we can restrict the X-ray flux not to occur the pile up. The combination of an X-ray telescope and CCD enables us to simultaneously obtain an X-ray image and spectrum. Therefore, we can precisely perform spatially resolved spectral analyses. X-ray CCDs significantly contribute to discoveries of important results and progress of astrophysics. They are the fundamental imaging detectors employed onboard the present astronomical satellites and for future missions.

We have developed an Application Specific Integrated Circuits (ASIC) for a CCD readout system in order to make a circuit size small and its power consumption low. For the progress of the semiconductor technology, we can implement both of analog and digital circuits in one chip. Our ASIC with a size of $3 \text{ mm} \times 3 \text{ mm}$ has four channels, each channel converts a CCD analog signal to 12-bit data. We employ a fabrication process of a $0.35 \mu\text{m}$ Complementary Metal-Oxide Semiconductor (CMOS) technology provided by Taiwan Semiconductor Manufacturing Company (TSMC). The equivalent input noise of our ASIC achieved is $41 \mu\text{V}$ and the power consumption is 90 mW per chip at the pixel readout rate of 156 kHz .

We are presently developing the Soft X-ray Imager (SXI), the X-ray CCD camera system, for ASTRO-H using our ASICs. ASTRO-H is the Japanese sixth X-ray astronomical satellite and will be launched into the low earth orbit of 550 km on 2013. The devices onboard the satellite will be damaged mainly by protons during passing through the South Atlantic Anomaly (SAA). We tested the total ionization dose effect of the ASIC by using 200 MeV proton beam. We verified that the radiation tolerance was more than 17 krad and the ASIC surrounded by Al with the thickness of 1 mm met the requirement for ASTRO-H. The X-ray CCDs for the SXI prototype models presently have been developed. We evaluated the performance of the camera system using the ASIC and these CCDs. The readout noise and energy resolution (Full Width at Half Maximum (FWHM)) using single events at 5.9 keV were $7.5 e^-$ and 150 eV at the pixel rate of 40 kHz , respectively. Since the noise component from the ASIC was dominant in the total readout noise, we developed the revised ASIC that implemented the low noise preamplifier. We achieved that the equivalent input noise was $29 \mu\text{V}$ at the pixel readout rate of 156 kHz .

We are also developing a new X-ray CCD camera system (*C-link system*) utilizing the ASIC and Camera Link to realize a multi-readout of CCD signals at a high pixel rate of up to 1 MHz . We obtained a proper frame image and spectrum at the pixel rate of 40 kHz . The readout noise and energy resolution (FWHM) using single events at 22.1 keV

are $9.9 e^-$ and $518 eV$, respectively. We expect that *C-link system* enables anyone to easily construct a compact readout system for X-ray CCDs with low noise and high pixel rate.

Contents

1	Introduction	1
2	X-ray CCDs	5
2.1	Output signal of an X-ray CCD	5
2.1.1	FDA	5
2.1.2	N-channel and p-channel CCD signals	8
2.2	Noise of an X-ray CCD	9
2.2.1	White noise	9
2.2.2	1/f noise	10
2.3	Concept of the signal process for X-ray CCDs	11
2.3.1	Preamplifier	11
2.3.2	Band-pass filter	12
2.3.3	ADC	16
2.4	Energy resolution	17
3	ASICs	19
3.1	Overview of ASICs	19
3.2	Preamplifier	20
3.2.1	Operational amplifier	22
3.3	5-bit DAC	24
3.4	$\Delta\Sigma$ ADC	29
3.4.1	Concept of $\Delta\Sigma$ ADCs	29
3.4.2	$\Delta\Sigma$ ADC implemented in our ASICs	34
3.5	Chain	41
3.5.1	Integral Non-Linearity (INL)	41
3.5.2	Noise performance	42
3.6	Interface	44
3.7	Development process of our ASICs	46

4	Performance of ASICs	47
4.1	Evaluation test system	47
4.2	Integral Non-Linearity (INL)	49
4.3	Noise performance	52
4.4	Power consumption	53
4.5	Highest pixel rate	54
4.6	Radiation test	60
4.6.1	Motivation	60
4.6.2	Test condition	60
4.6.3	Test results	61
4.7	Test summary	70
5	Performance of CCD camera systems using ASICs	75
5.1	Evaluation test setup	75
5.1.1	CCD-NeXT2	76
5.1.2	Pch2k4k	78
5.2	Test results	78
5.3	Test results using 4 average method	89
6	High speed drive and readout system for X-ray CCDs	91
6.1	<i>C-link system</i>	91
6.1.1	Camera Link board	91
6.1.2	DE I/F and ARM processor boards	92
6.1.3	Driver, drain and video boards	94
6.2	Performance of <i>C-link system</i>	95
6.2.1	Unit testing	95
6.2.2	Test using an X-ray CCD	95
7	Summary	101
	Acknowledgments	105
	References	107

List of Tables

3.1	Hierarchy of our ASIC.	21
4.1	Performance summary of ASICs.	70
4.2	Average and deviation of noise, INL and gain.	70
5.1	Specification of X-ray CCDs.	79
5.2	Test condition and results (CCD-NeXT2) by MD01.	86
5.3	Test condition and results (CCD-NeXT2) by <i>MiKE</i> system.	86
5.4	Test condition and results (Pch2k4k) by MD01.	87
5.5	Test condition and results (Pch2k4k) by <i>MiKE</i> system.	87
6.1	Specification for the support signals of <i>C-link system</i>	96
6.2	Test condition and results by <i>C-link system</i>	100

List of Figures

2.1	Schematic view of a CCD device.	6
2.2	Block diagram of the FDA.	7
2.3	Signal waveforms of a n-channel and p-channel CCDs.	8
2.4	Equivalent circuit of the FDA and its simulation result.	9
2.5	Square wave of the frequency = 100 kHz and its Fourier-transform result.	10
2.6	CCD noise spectrum density.	11
2.7	Signal process diagram for a readout of X-ray CCD signals.	11
2.8	Concept of an iCDS method.	13
2.9	Equivalent noise charge in an iCDS method as a function of a pixel rate.	14
2.10	Concept of a multi-sampling method.	15
2.11	Equivalent noise charge in the multi-sampling method as a function of the pixel rate.	16
3.1	Data flow diagram of the readout system employing our ASIC.	20
3.2	A photograph of the bare chip.	21
3.3	Block diagram of the preamplifier.	23
3.4	Simulation result of the preamplifier.	23
3.5	Block diagram of the operational amplifier.	24
3.6	Block diagram of the operational amplifier.	25
3.7	AC analysis results of the operational amplifiers.	26
3.8	Block diagram of 5-bit DAC.	27
3.9	Data formats for the serial register of 5-bit DAC and preamplifier gain.	28
3.10	Simulation result of 5-bit DAC.	28
3.11	Block diagram of a basic first-order $\Delta\Sigma$ ADC.	30
3.12	Simulation results of $\Delta\Sigma$ ADC.	31
3.13	z-domain model for the first-order $\Delta\Sigma$ ADC shown in Fig. 3.11.	32
3.14	NTFs of first, second, third and fourth-order $\Delta\Sigma$ ADCs.	32
3.15	STFs of sinc, sinc2 and sinc3 filters.	35

3.16	Theoretical resolution as a function of a data length.	35
3.17	Block diagram of the $\Delta\Sigma$ ADC in our ASICs.	36
3.18	Impulse responses of sinc, sinc2 and sinc3 filters with N=32.	37
3.19	STFs of sinc, sinc2 and sinc3 filters No.2.	38
3.20	Block diagram for the explanation of the premodulator.	39
3.21	Data process diagram of the $\Delta\Sigma$ ADC in our ASICs.	39
3.22	Filter coefficient of our ASICs.	40
3.23	Decimal value as a function of the sample number.	41
3.24	Block diagram of a chain.	42
3.25	Simulation results of the chain.	43
3.26	Linearity of the chain.	43
3.27	Noise simulation results of the preamplifiers.	44
3.28	Noise calculation results.	45
3.29	Calculated noise from the preamplifier in MD02 and MND02 as a function of the pixel rate.	46
4.1	Photograph of the test board.	48
4.2	Block diagram of the evaluation test system.	48
4.3	Signal waveforms of the chain.	49
4.4	Scatter plots of the filtered ASIC outputs (MD02).	50
4.5	Histograms of the filtered ASIC outputs (MD02).	51
4.6	Linearity of 4 ASICs.	52
4.7	Equivalent input noise as a function of the pixel rate.	54
4.8	Power consumption of ASICs per chip as a function of the pixel rate.	55
4.9	Rise and fall times of Dout signals in MD01 and MND01.	57
4.10	Output signals of the LVDS drivers in MD01 and MND01.	58
4.11	Scatter plots of channel-2 in MND01.	59
4.12	TID as a function of the radiation time.	61
4.13	Monitors of analog and digital currents during the radiation test.	63
4.14	Linearity of MD01 at the TID of 0, 22 and 25 krad.	64
4.15	Relative gain of each readout channel as a function of the TID.	65
4.16	Scatter plots of channel-0 and channel-1 at the TID of 22 krad.	66
4.17	Relative sigma of each readout channel as a function of the TID.	67
4.18	Simulation results of the preamplifier as the threshold voltage shift = 0 V and 0.6 V.	68
4.19	Simulation result of the TID as a function of a thickness of Al shield.	69
4.20	Integrated fluence of proton and electron defined in the simulation.	69

4.21	Noise distributions of 4 ASICs.	71
4.22	INL distributions of 4 ASICs.	72
4.23	Gain distributions of 4 ASICs.	73
5.1	Block diagram of the readout system for X-ray CCDs.	76
5.2	Photographs of <i>MiKE</i> system and DP.	77
5.3	Photographs of the video board and CCD-NeXT2.	77
5.4	Photographs of the video board and Pch2k4k.	79
5.5	Frame image with a metal mesh obtained by using CCD-NeXT2.	81
5.6	X-ray spectra (g0) of ^{55}Fe obtained by using CCD-NeXT2.	82
5.7	X-ray spectra(g02346) of ^{55}Fe obtained by using CCD-NeXT2.	83
5.8	X-ray spectra (g0) of ^{55}Fe obtained by using Pch2k4k.	84
5.9	X-ray spectra (g02346) of ^{55}Fe obtained by using Pch2k4k.	85
5.10	Relation between energy resolution or event count and split threshold.	88
5.11	Block diagram of readout method which takes the average of 4 outputs.	89
5.12	X-ray spectra of ^{55}Fe by CCD-NeXT2 and Pch2k4k in 4 average method.	90
6.1	Block diagram of <i>C-link system</i>	92
6.2	Data format of Camera Link in 1 data transfer cycle.	93
6.3	Signal diagram for the explanation of FVAL, LVAL and DVAL signals.	93
6.4	Photograph of the DE I/F board and its block diagram.	94
6.5	Block diagram of the pixel data buffer.	94
6.6	Photographs of the driver and drain boards.	97
6.7	Equivalent input noise of <i>C-link system</i> without CCDs as a function the pixel rate.	98
6.8	Whole frame image and its partial closeup.	98
6.9	Spectrum of ^{109}Cd obtained by <i>C-link system</i> at the pixel rate of 39 kHz.	99
6.10	Comparison between the energy resolution by <i>MiKE</i> system and by <i>C-link</i> <i>system</i>	99

Chapter 1

Introduction

X-ray Charge-Coupled Devices (CCDs) are superior imaging detectors with excellent positional resolution ($\sim 20 \mu\text{m}$) and high quantum efficiency in an energy band of $0.2 \text{ keV} \sim 10 \text{ keV}$, where conventional X-ray mirrors are available as focusing devices. The X-ray CCD can also work as spectrometers with moderate energy resolution ($\sim 130 \text{ eV}$ Full Width at Half Maximum (FWHM) at 5.9 keV), when they are operated in the photon-counting mode.

The Solid state Imaging Spectrometers (SIS) on board the Japanese 4th X-ray astronomy satellite, ASCA (Tanaka et al. 1994), were the first X-ray CCDs that were placed in the focal plain of the X-ray focusing mirrors and worked as X-ray imaging spectrometers. The ASCA SIS opened a new window in the field of X-ray astronomy, *i.e.*, spatially resolved spectroscopy of cosmic plasma with enough quality to diagnose elemental abundances and ionization states, for which energy resolution of previous gas detectors were not sufficient. For example, X-ray spectra of each position of a supernova remnant (SNR) tell us not only the plasma temperatures but also their elemental abundances and ionization states. These information are crucial to identify the origin of the plasmas and to examine the progenitor of the remnant. Spatially resolved X-ray spectroscopy of diffuse hot plasmas filled in elliptical galaxies and clusters of galaxies reveals the origin of heavy elements in the universe. Spatial distribution of the plasma in these objects provides evidence of dark matter which gravitationally binds those hot plasmas. Compact X-ray sources, such as, neutron stars, black hole binaries, active galactic nuclei are also important targets for X-ray CCD imaging spectrometers. Subsequent X-ray astronomy satellites after ASCA employ the X-ray CCD, the Chandra ACIS (Garmire et al. 2003), the XMM-Newton EPIC (Strüder et al. 2001), (Turner et al. 2001) and the Suzaku XIS (Koyama et al. 2007). Observations with these X-ray satellites have made progress in the X-ray imaging spectroscopy of cosmic plasma, in its quality and variety, with many unprecedented results.

A weak point of the X-ray CCD systems is, however, in their time resolution. Most of the X-ray CCD systems mentioned above has a frame time of a few seconds, which can be regarded as the time resolution of those systems.¹ The time resolution of the X-ray CCDs is significantly lower than that of other photon counting X-ray detectors, such as gas proportional counters, solid state detectors (typically $1\ \mu\text{s}$ or less), or micro calorimeters ($\sim\ \text{ms}$). Rapid variabilities with time scales down to milliseconds are observed in compact X-ray sources (black hole binaries, neutron star binaries) and have been an important subjects in X-ray astronomy. Although various kinds of X-ray emitting pulsars have wide range of pulsation periods, it ranges from a few milliseconds to several hundreds seconds. Pulse phase resolved spectroscopy is a powerful tool to investigate those sources. The time resolution of a few seconds will significantly restricts the targets for these kinds of studies.

Another issue we have to consider for X-ray CCDs (and other photon-counting detectors) is pile-up effects. In order to measure the energy of each X-ray photon with X-ray CCDs, the number of photons entered into a pixel of the CCD during a frame time must be one or zero. If two or more photons enter a pixel, i.e., pile-up, we cannot distinguish the event from that of a single photon with a higher energy, resulting in incorrect spectra. This pile-up effect limits the maximum intensity of the targets which can be observed in the photon-counting mode. The limit gets severer for the focusing mirrors with better imaging quality and larger effective area. In fact, the pile-up effect hampers observations of some bright sources with currently working X-ray satellites, Chandra, XMM-Newton, and Suzaku. The condition will be much severer in future missions with larger effective area, such as the International X-ray Observatory (IXO). This project supersedes both National Aeronautics and Space Administration's (NASA's) Constellation-X (Bookbinder et al. 2008) and European Space Agency's (ESA's) X-ray Evolving Universe Spectroscopy (XEUS) (Parmar et al. 2006) mission concepts. In order to reduce this pile-up effect, i.e., to raise the intensity limit, we have to reduce the frame-time of the X-ray CCD. It will be enabled by speeding up the readout time and/or increasing the number of readout nodes. These two options are also needed to catch up with increasing size of the X-ray CCD chips, reflecting the increasing size of the X-ray satellites.

These requirements are accelerating the development of fast X-ray CCD systems. The noise level of the current X-ray CCD systems (e.g. Koyama et al. 2007, Miyata et al. 2006)

¹ASCA SIS and most of other X-ray CCDs on board X-ray astronomy satellites can be operated in a special observation mode for fast timing observations. In the case of the ASCA SIS, Fast mode prepared for that purpose could realize 16ms time resolution. Nevertheless, imaging information in this mode is one dimensional and the target is limited to a bright point-like source.

realizes energy resolution as good as the theoretical limit (Fano limit). However, the pixel rate is limited up to about 100 kHz without degradation of the readout noise. Since current X-ray CCDs have typically $\sim 10^5$ pixels per readout node, we cannot expect reducing the frame time by an order magnitude with current systems. Increasing the number of readout nodes to, for example, 100 will be a solution. However, in this case, the size and electric power needed is unrealistic for space use, if we simply employ 100 units of the current CCD electronics systems which are constructed with discrete electronic components.

We thus have started developing of an Application Specific Integrated Circuits (ASIC) for multi-readout X-ray CCDs. An ASIC is a key technology to realize multi-channel readout systems for pixel and strip detectors. Another reason behind present ASIC developments is that foundries provide a multi-project wafer run with relatively low price.

Some institutes have been developing ASICs for the readout of CCDs. In X-ray region, the CMOS Amplifier and MultipLEXer (CAMEX) chip was employed as the readout system for pnCCDs onboard XMM-Newton (Strüder et al. 2001). The revised CAMEX will be employed for the eROSITA X-ray telescope (Herrmann et al. 2007). The ASIC with the size of 9 mm \times 6 mm has 128 analog readout channels. Each channel consists of a Junction Field Effect Transistor (JFET)-amplifier, low-pass filter, 8-fold Correlated Double Sampling (CDS) circuit and sample & hold circuit. A multiplexer is connected to each channel and transmits the analog data of 128 channels to an Analog-to-Digital Converter (ADC) off the chip. An image area of the CCD is 384 \times 384 pixels, and each column has a readout node that is connected to the CAMEX chip. Its frame rate of a full image mode is 20 Hz. In visible region, a team in the Lawrence Berkeley National Laboratory developed an ASIC for the Super Nova-Acceleration Probe (SNAP) satellite (Karcher et al. 2007). The number of channel is 4 and each channel consists of a preamplifier, CDS circuit and pipeline ADC. This chip has an excellent low noise of 6.2 μ V at the pixel rate of 100 kHz and low power consumption of 121 mW.

Our first ASIC had two readout channels and each channel consisted of an integrated Correlated Double Sampling (iCDS) circuit and slope ADC (Matsuura et al. 2007). A noise level of this ASIC was about 10 times worse than our requirement of several electrons. We decided to develop a new type of ASIC that employed a $\Delta\Sigma$ ADC (Inose et al. 1962) instead of the iCDS circuit and slope ADC (Doty patent 2006a), (Doty et al. 2006b). An outline of our ASICs is described in Chapter 3. Their test results by using pseudo signals are summarized in Chapter 4.

We are presently designing an X-ray CCD camera system for the Soft X-ray Imager (SXI) (Tsunemi et al. 2008) onboard ASTRO-H (Takahashi et al. 2008) employing our ASICs. ASTRO-H is the Japanese sixth X-ray astronomical mission following to

Suzaku (Mitsuda et al. 2007), and will be launched in 2013. In the SXI, all components of the CCD camera system, such as CCDs, cooling device, drive and readout systems, are developed in Japan. We evaluated performances of camera systems using the ASIC and X-ray CCDs of prototype models for the SXI in Chapter 5. We are also developing another readout system with low noise and high pixel rate using the ASIC for ground experiments as shown in Chapter 6.

Chapter 2

X-ray CCDs

2.1 Output signal of an X-ray CCD

A CCD is a two dimensional pixel array, which is separated by electric potential, as shown in Fig. 2.1. Signal charges generated in a depletion layer are collected in the electric potential well under the individual pixel. As shown in Fig. 2.1, the signal charges are regularly transported to the adjacent pixel and finally converted to the signal voltage by an Floating Diffusion Amplifier (FDA).

The amount of signal charge generated in a Si wafer is given by $\frac{E_x}{W_{Si}}$, where E_x is the incident photon energy and W_{Si} is the energy to generate an electron-hole pair for Si (3.65 eV). In the case of optical application, the amount of signal charge per photon is a few electrons. CCDs are operated in a flux-mode and only measure the energy flux. On the other hand, an X-ray photon in the energy range from 0.2 to 10 keV generates the amount of signal charges from 55 to 2740 electrons. Since the signal is larger than the readout noise, X-ray CCDs operated in the photon-counting mode can measure the incident photon energy. However, the output signal level of X-ray CCDs in the photon-counting mode is generally fainter than that of the flux mode. We should cool a device to about -100°C to reduce the thermal noise, and design a low noise readout system in order to precisely measure the photon energy.

2.1.1 FDA

The FDA consists of Output Gate (OG), 2 MOS FETs and load resistance as shown in Fig. 2.2. MOS FET1 functions as a reset switch and MOS FET2 configures a source follower amplifier. The load resistance for the source follower amplifier is not generally included in CCDs and placed outside devices. The charge transfer is performed by clocking

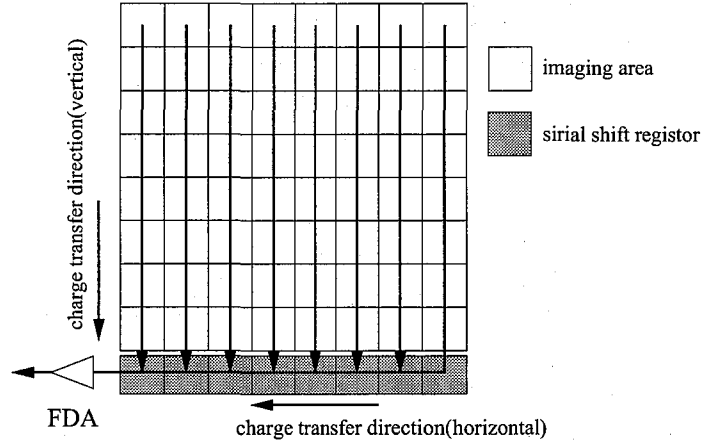


Figure 2.1: Schematic view of a full-frame CCD device.

gate voltages such as the horizontal transfer gate (P1H) and Summing Gate (SG). We supply a Direct-Current (DC) voltage to OG for the separation between SG and Floating Gate (FG) when SG is clocked high. Sense capacitance (C_s) converts the transferred charges to the voltage signal. C_s is determined from a node capacitance of FG, gate capacitance of MOS FET2 and neighboring parasitic capacitances (Janesick, J. R. 2001). The conversion factor of CCDs can be described as

$$S_v = \frac{q}{C_s} \quad (2.1)$$

where S_v is the conversion factor ($\mu\text{V}/e^-$) and q is the elementary electric charge (1.6×10^{-19} coulombs). Since S_v is a order of several ($\mu\text{V}/e^-$), we find that C_s is designed to be an order of several 10 fF.

Fig. 2.2(1)~(3) illustrate the operation of the FDA including Reset Gate (RG), SG and P1H during 1 pixel readout time. Signal waveforms of CCDs after an amplifier with a gain of 10 are shown in Fig. 2.3. There are 3 voltage levels in a CCD signal, which we call a reset, floating and signal levels. These voltage levels are generated in each operation of the FDA shown in Fig. 2.2(1)~(3). Fig. 2.2(1)(2) show the reset operation of FG. There are the signal charges of the previous pixel in FG in Fig. 2.2(1). These charges are passed through MOS FET1 when RG is clocked high, and FG is reset as shown in Fig. 2.2(2). Figure 2.4 shows the equivalent circuit of the FDA and its simulation. Since C_s and a gate to source capacitance of MOS FET1 (C_{rg}) shown in Fig. 2.4 (left) divides the clock signal of RG, the voltage of FG is determined by the drain voltage of MOS FET1 (RD) and the RG feed-through pulse as shown in Fig. 2.4 (right) during the reset operation. These voltage levels of FG correspond to the reset and floating levels in Fig. 2.3. As shown in Fig. 2.2(c), the signal charges in SG are transferred to FG when SG is clocked low. The

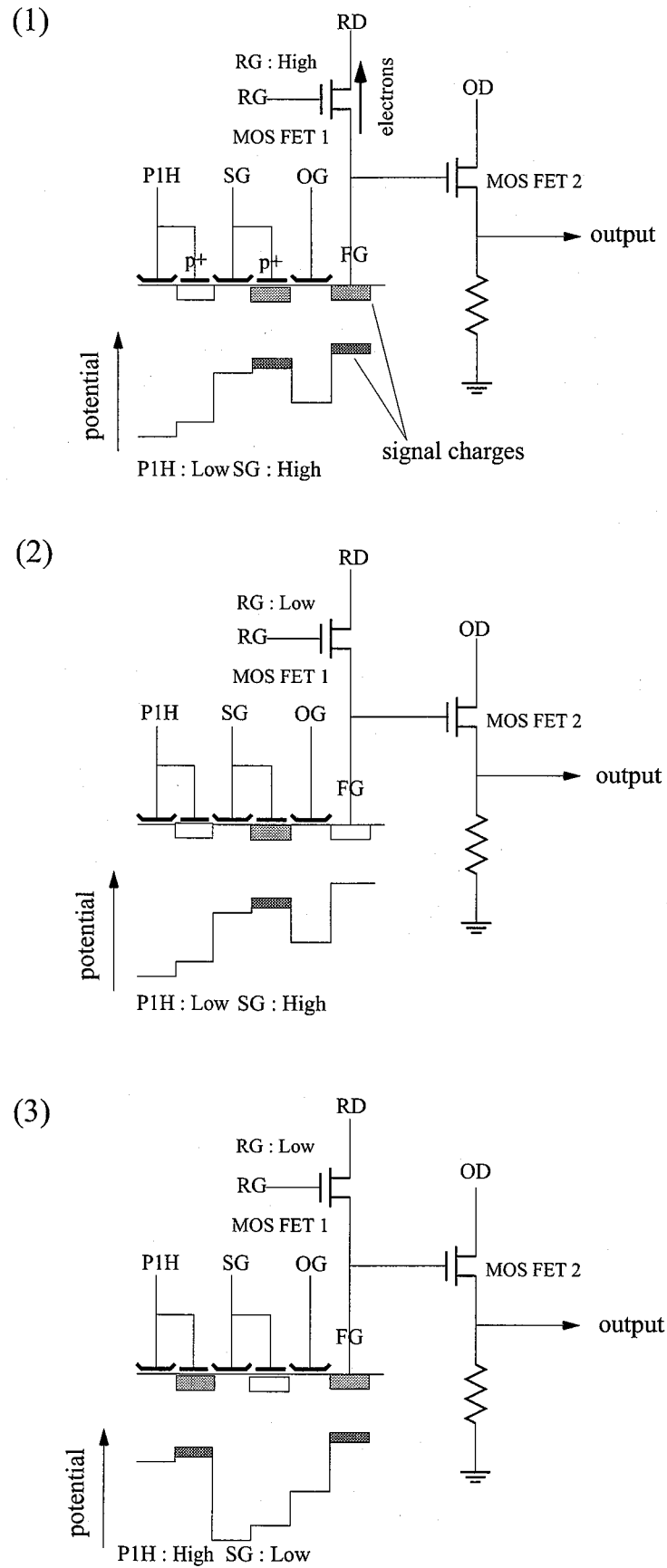


Figure 2.2: Block diagram of the FDA and its operation.

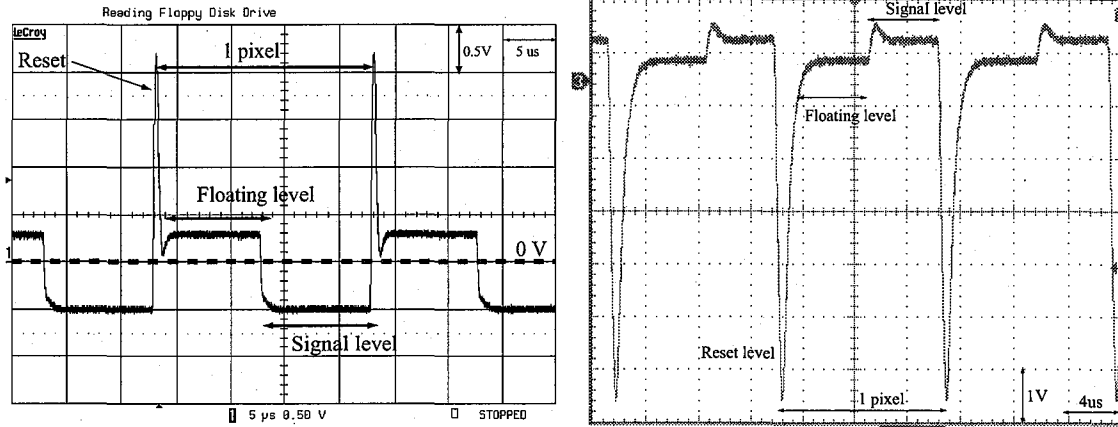


Figure 2.3: Signal waveforms of a n-channel (left) and p-channel CCDs (right) after the amplifier with the gain of 10.

voltage change of FG is proportional to the amount of charges as given by $S_v \times \frac{E_x}{3.65(\text{eV})}$. Assuming $S_v=3.5(\mu\text{V}/e^-)$ and $E_x=5900\text{eV}$, we estimated that the voltage change was 5.6mV . The feed-through pulse of SG clock signal also appears in the CCD signal as that of RG, which yields a voltage difference ($10\sim 50\text{mV}$) between the floating and signal levels shown in Fig. 2.4 (right) when there is not signal charges in the pixel.

We need to precisely obtain the voltage difference to measure the incident X-ray energy. The reset level is unnecessary for the data process. Therefore, a CCD signal can be considered to appear as a square wave shown in Fig. 2.5 (left). A normalized square wave is described as

$$g(t) = \frac{4}{\pi} \sum_{n=1}^{\infty} \frac{\sin((2n-1)2\pi f_0 t)}{(2n-1)} \quad (2.2)$$

where f_0 is frequency of a square wave. Fourier transform gives the frequency characteristic of the square wave. Fig. 2.5(right) shows the square wave of $f_0=100\text{kHz}$ in frequency region.

2.1.2 N-channel and p-channel CCD signals

X-ray CCDs are classified into 2 groups by the type of silicon wafer employed that are p-type Si and n-type Si. CCDs fabricated on p-type and n-type silicon wafers are called n-channel and p-channel CCDs, respectively. Because the major and minor carriers are different between n-type and p-type silicon wafers, the polarity of their CCD signals is opposite each other. Figure 2.3 shows signal waveforms of n-channel (left) and p-channel CCDs (right). However, the signal process for each CCD is quite similar to each other.

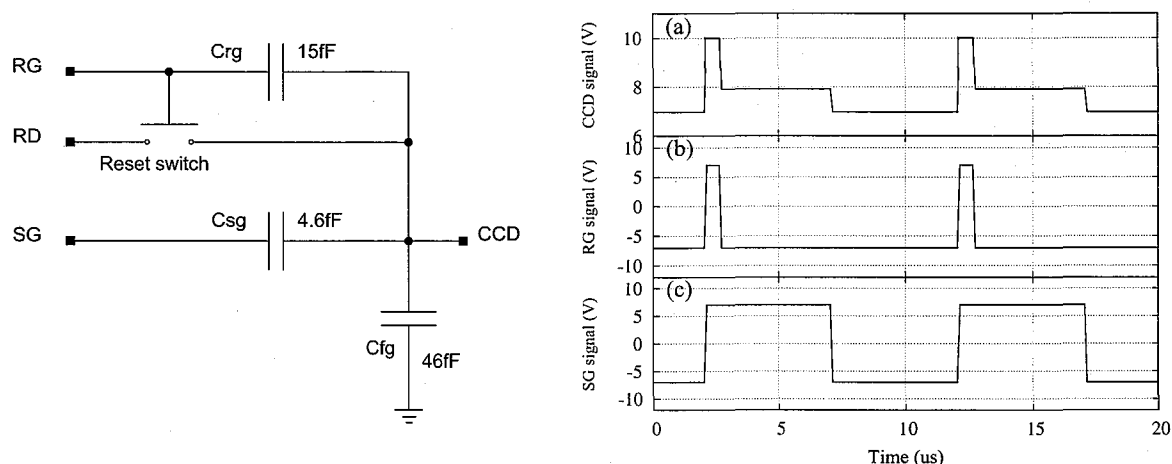


Figure 2.4: Equivalent circuit of the FDA (left) and its simulation result(right). Note that the capacitance shown here has a typical value. (right:a) is the simulated CCD signal. In this simulation, we set $RG = \pm 7V$ (right:b), $SG = \pm 7V$ (right:c) and the drain voltage of MOS FET1 (RD) = 10 V.

2.2 Noise of an X-ray CCD

A CCD signal contains some noise components such as the dark noise, transfer noise, white noise and $1/f$ noise. We focus on the electronic noise generated by the FDA in this section.

2.2.1 White noise

White noise is generated by a random signal with the flat power spectral density, its noise intensity is independent of the broad range of frequency. The Johnson white noise is generated by the fluctuation of the current flow through a resistance. The characteristic of this noise was first measured by John B. Johnson and its principle was explained by Harry Nyquist. When the carriers pass through the resistance, they collide with the lattice of the resistance, which causes an erratic carrier motion. Since the cross section of the lattice increases as the temperature, the Johnson white noise depends on the temperature of the device. The power spectrum density of this white noise (V/\sqrt{Hz}) is given by

$$N_{\text{white}} = \sqrt{4k_B T R_{\text{eff}}} \quad (2.3)$$

where k_B is Boltzmann's constant ($1.38 \times 10^{-23} \text{ J/K}$), T is absolute temperature (K) and R_{eff} is a effective resistance value (Ω). For the FDA, white noise is generated by the

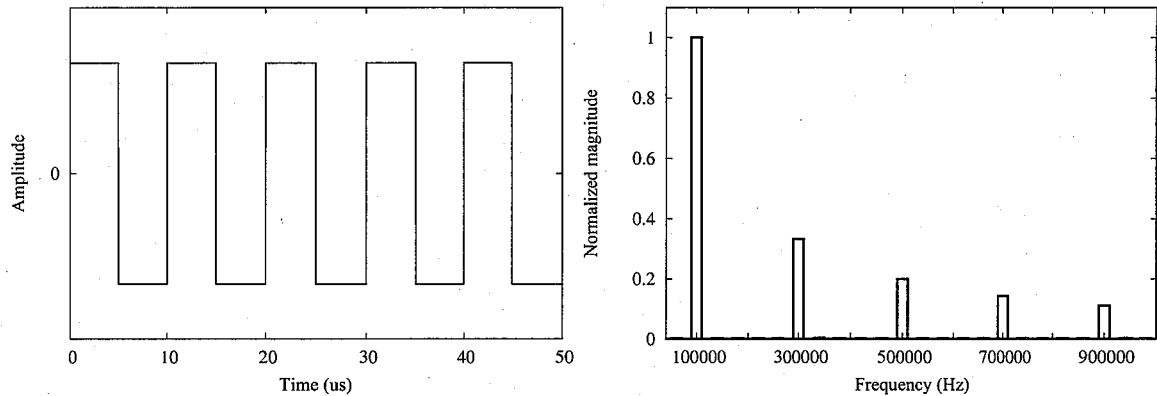


Figure 2.5: Square wave of the frequency = 100 kHz(left) and its Fourier-transform result(right).

channel resistance of MOS FET1 and MOS FET2, and the load resistance shown in Fig. 2.2.

2.2.2 1/f noise

The noise power of 1/f noise is proportional to the inverse of frequency. The disruption of the silicon lattice and the impurity in the conductive channel lead to the energy level in the forbidden gap. 1/f noise is generated by the fluctuation of the number of carriers due to the trapping and the release by these energy levels. This noise is generally dominant in the readout system noise. For the FDA, 1/f noise is generated by MOS FETs. The power spectrum density of 1/f noise ($V/\sqrt{\text{Hz}}$) from a MOS FET can be described as

$$N_{1/f}(f) = \left(\frac{K}{C_{\text{ox}} L W f} \right)^{\frac{1}{2}} \quad (2.4)$$

where K is a noise constant that is the fabrication process-dependent constant, C_{ox} is a gate oxide capacitance per unit area, W and L are a gate width and length of a FET.

A total noise of the FDA (V^2/Hz) composed of white noise and 1/f noise is given by

$$N_{\text{CCD}}(f)^2 = N_{\text{white}}^2 \left(1 + \left(\frac{f_C}{f} \right)^A \right) \quad (2.5)$$

where N_{white} is white noise ($V/\sqrt{\text{Hz}}$), f_C is the corner frequency (Hz) where the noise level of 1/f noise is comparable to that of white noise, and A is a constant value with the range of $1 < A < 2$ (Janesick, J. R. 2001). Assuming $N_{\text{white}} = 25$ ($nV/\sqrt{\text{Hz}}$), $f_C = 50$ kHz and $A=1$,

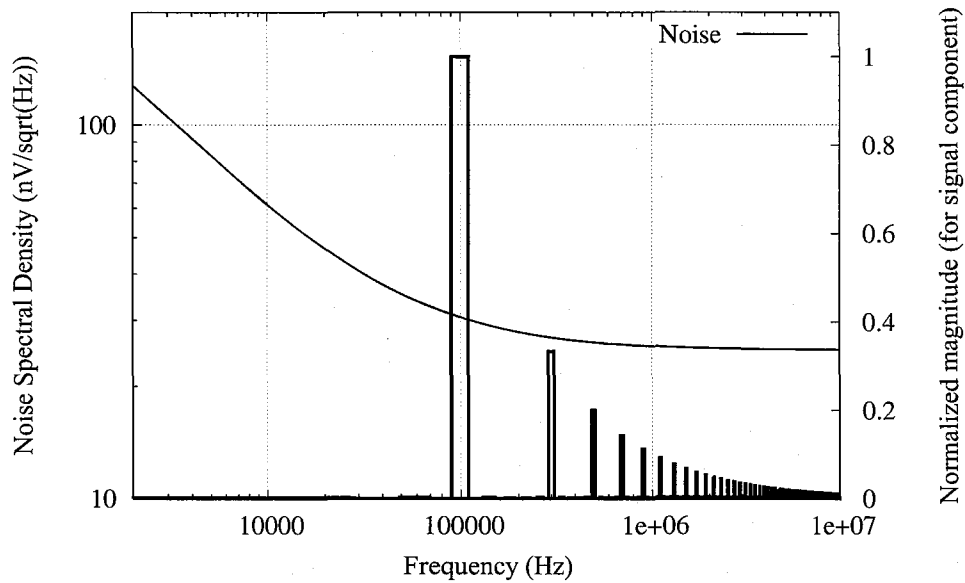


Figure 2.6: Power spectrum density of the example CCD noise and the square wave of the frequency = 100 kHz.



Figure 2.7: Signal process diagram for a readout of X-ray CCD signals.

we show the power spectrum density of the example CCD noise in Fig. 2.6. The square wave of the frequency = 100 kHz is shown together with the CCD noise in Fig. 2.6 as the signal component.

2.3 Concept of the signal process for X-ray CCDs

We show the signal process diagram between a CCD and a digital processor (DP) in Fig. 2.7. Each process is briefly explained in the following subsections.

2.3.1 Preamplifier

CCD signals have a large DC offset of about 10 V. A CCD signal is input to a preamplifier through an Alternating-Current (AC) coupling to remove the DC offset. We need to take account into the noise of the preamplifier in order not to degrade the faint CCD signal as

much as possible. Since the preamplifier amplifies the CCD signal by a factor of ~ 10 , the signal is hardly affected by the extrinsic noise and the following readout circuit noise.

2.3.2 Band-pass filter

An output signal of the preamplifier is composed of a signal and noise components as shown in Fig. 2.6. We need to eliminate the noise at the frequency where the signal component is not contained in order to improve a Signal-to-Noise (SN) ratio. Therefore, we generally implement a band-pass filter before an ADC. The band-pass filters utilized in CCD readout systems are explained in next subsections.

iCDS method

An iCDS method is widely employed in readout systems for X-ray CCDs such as the XIS and the Solid-state Slit Camera (SSC) onboard the Monitor of All-sky X-ray Image (MAXI). In the iCDS method, the voltage of the floating and signal levels are integrated for the equal time duration as shown in Fig. 2.8. We, additionally, obtain the correlation between these integration values by a CDS process. These signal processes of the integration and CDS correspond to the low-pass and high-pass filters, respectively.

The normalized Signal Transfer Functions (STFs) of the integration, CDS and iCDS in s-domain are given as

$$H_{\text{integ}}(s) = \frac{-1}{RCs} \frac{RC}{T_i} (1 - \exp(-sT_i)) \quad (2.6)$$

$$H_{\text{cds}}(s) = 1 - \exp(-sT_g) \quad (2.7)$$

$$H_{\text{icds}}(s) = H_{\text{integ}}(s) \times H_{\text{cds}}(s), \quad (2.8)$$

where R and C are the resistance and capacitance in the integrator, T_i is the integration time and T_g is the time between the start of the integration for the floating level and that for the signal level. s-domain models (Laplace transform) are widely used for analyses of linear time-invariant systems such as electrical circuits. We can easily calculate STFs and convolutions of systems by using s-domain models rather than the time-domain model. The parameter “s” corresponds to “ $j2\pi f$ ”, where j is the imaginary unit and f is frequency. Substituting $s=j2\pi f$ to the STFs, eq.(2.6)~eq.(2.8) in the frequency domain can be described as

$$|H_{\text{integ}}(f)|^2 = \left(\frac{1}{RC\pi f} \frac{RC}{T_i} \sin(\pi f T_i) \right)^2 \quad (2.9)$$

$$|H_{\text{cds}}(f)|^2 = (2 \sin(\pi f T_g))^2 \quad (2.10)$$

$$|H_{\text{icds}}(f)|^2 = |H_{\text{integ}}(f)|^2 \times |H_{\text{cds}}(f)|^2 = \left(\frac{2}{\pi f T_i} \sin(\pi f T_i) \times \sin(\pi f T_g) \right)^2. \quad (2.11)$$

These equations are shown in Fig. 2.9 (left) when $T_{\text{pixel}}=3T_i=3T_g=10\mu\text{s}$, where T_{pixel} is 1 pixel readout time.

The noise spectral density of the filtered CCD noise is calculated by

$$|N_{\text{iCDS}}(f)|^2 = |N_{\text{CCD}}(f)|^2 \times |H_{\text{iCDS}}(f)|^2, \quad (2.12)$$

where $N_{\text{CCD}}(f)^2$ is the CCD noise given by eq.(2.5). An integration of Eq. 2.12 with respect to frequency is an equivalent input noise, given by

$$\begin{aligned} N_{\text{iCDS}} &= \frac{1}{S_v} \left(\int_0^\infty |N_{\text{iCDS}}(f)|^2 df \right)^{1/2} \\ &= \frac{2}{S_v \pi f T_i} \left(\int_0^\infty N_{\text{white}}(f)^2 \left(1 + \left(\frac{f_C}{f} \right)^A \right) \cdot \sin^2(\pi f T_i) \cdot \sin^2(\pi f T_g) df \right)^{1/2} \end{aligned} \quad (2.13)$$

For example, assuming $S_v = 3.5 (\mu\text{V}/e^-)$, $N_{\text{white}} = 25 (\text{nV}/\sqrt{\text{Hz}})$, $f_C = 50 \text{ kHz}$, $A=1$ and $T_{\text{pixel}}=3T_i=3T_g$, we show the calculated noise charge for the iCDS method as a function of the pixel rate in Fig. 2.9 (right).

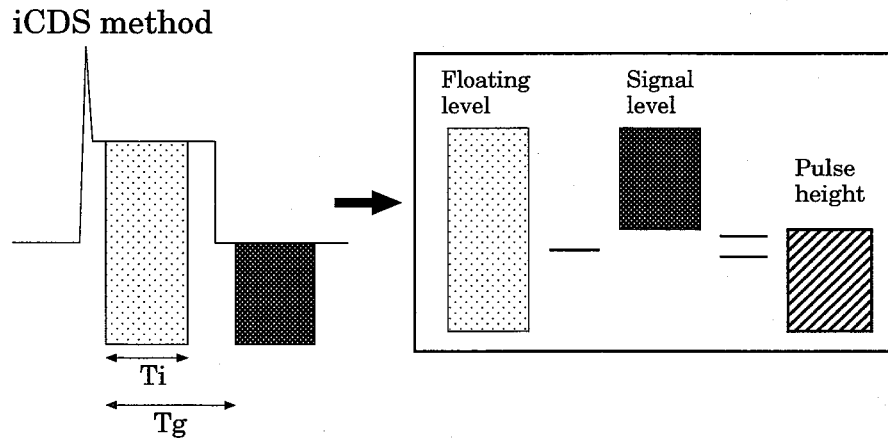


Figure 2.8: Concept of the iCDS method.

Multi-sampling method

A multi-sampling method is applied to the CAMEX chip onboard XMM-Newton and our ASICs. In the multi-sampling method, the floating and signal levels are sampled many times as shown in Fig. 2.10. We, next, take the correlation between the sums of the sampled voltages. The sampling process corresponds to the low-pass filter. The STFs of

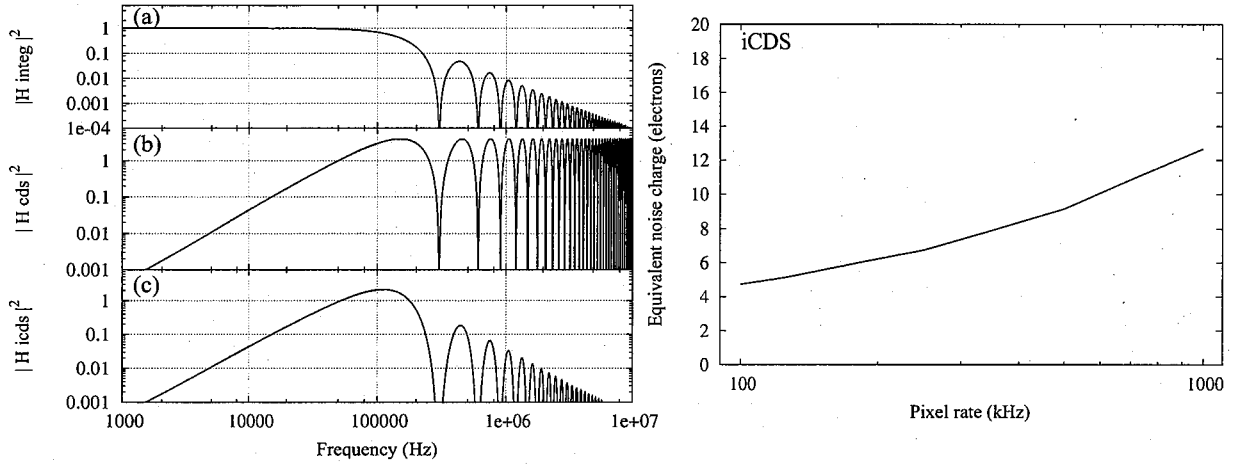


Figure 2.9: STFs of the integration, CDS and iCDS at the pixel rate of 100 kHz ($T_{\text{pixel}} = 10 \mu\text{s}$) (left). Example equivalent noise charge in the iCDS method as a function of the pixel rate (right).

the sampling, CDS and multi-sampling processes in s-domain are given as

$$H_{\text{sample}}(s) = \frac{1}{m} \sum_{n=0}^{m-1} \exp(-sT_s n) \quad (2.14)$$

$$H_{\text{cds}}(s) = 1 - \exp(-sT_g) \quad (2.15)$$

$$H_{m\text{-sample}}(s) = H_{\text{sample}}(s) \times H_{\text{cds}}(s), \quad (2.16)$$

where m is the number of samples, T_s is the sample-to-sample time and T_g is the time between the start of the sampling for the floating level and that for the signal level. These equations in the frequency domain can be described as

$$|H_{\text{sample}}(f)|^2 = \left(\frac{1}{m} \frac{2 \sin(m\pi f T_s)}{2 \sin(\pi f T_s)} \right)^2 \quad (2.17)$$

$$|H_{\text{cds}}(f)|^2 = (2 \sin(\pi f T_g))^2 \quad (2.18)$$

$$|H_{m\text{-sample}}(f)|^2 = |H_{\text{sample}}(f)|^2 \times |H_{\text{cds}}(f)|^2 = \left(\frac{2 \sin(m\pi f T_s)}{m \sin(\pi f T_s)} \sin(\pi f T_g) \right)^2. \quad (2.19)$$

These equations are shown in Fig. 2.11(left) when $m=40$, $T_{\text{pixel}}=3 T_g=3 \times 40 T_s= 10 \mu\text{s}$. The noise spectral density of the filtered CCD noise is given by

$$|N_{m\text{-sample}}(f)|^2 = |N_{\text{CCD}}(f)|^2 \times |H_{m\text{-sample}}(f)|^2. \quad (2.20)$$

We can write an equivalent noise charge in the multi-sampling method by

$$\begin{aligned} N_{m\text{-sample}} &= \frac{1}{S_v} \left(\int_0^\infty |N_{m\text{-sample}}(f)|^2 df \right)^{1/2} \\ &= \frac{2}{m S_v} \left(\int_0^\infty N_{\text{white}}(f)^2 \left(1 + \left(\frac{f_C}{f} \right)^A \right) \frac{\sin^2(m\pi f T_s)}{\sin^2(\pi f T_s)} \sin^2(\pi f T_g) df \right)^{1/2} \end{aligned} \quad (2.21)$$

For example, assuming $S_v = 3.5 (\mu\text{V}/e^-)$, $N_{\text{white}} = 25 (\text{nV}/\sqrt{\text{Hz}})$, $f_C = 50 \text{ kHz}$, $A=1$, $m=40$, $T_{\text{pixel}} = 3 T_g = 3 \times 40 T_s$, we show the calculated noise charge for a 40th-sample method as a function of the pixel rate in Fig. 2.11 (right).

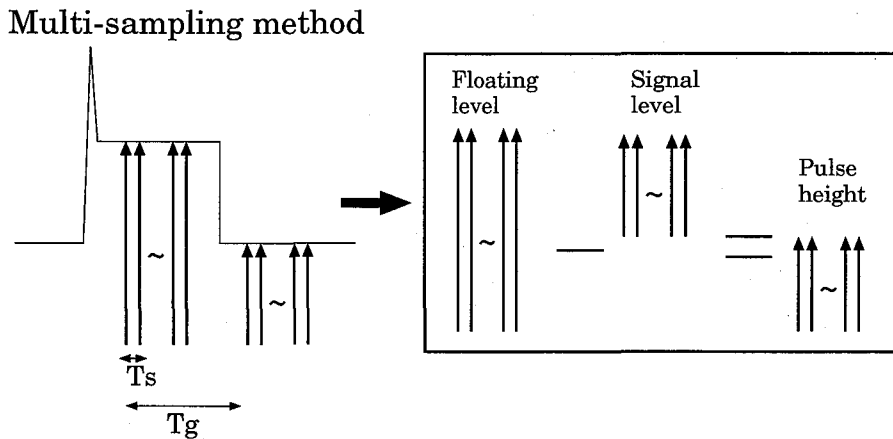


Figure 2.10: Concept of the multi-sampling method.

Comparison between the iCDS method and the multi-sampling method

Based on Figs 2.9 and 2.11, we can see that the performance of the multi-sampling method is comparable to that of the iCDS method. In the case of the iCDS method, we need a relatively large resistance of $\sim \text{M}\Omega$ or capacitance of $\sim 100 \text{ pF}$ to match a time constant ($R \times C$) of $\sim \mu\text{s}$ for the integrator. The typical integration time is $\sim 5 \mu\text{s}$, and the gain of the integrator is constrained up to 5 from the dynamic range of the following ADC. A resistor using poly silicon in the TSMC $0.35 \mu\text{m}$ CMOS process is $40 \Omega/\square$ (\square stands for $0.35 \mu\text{m}^2$). A poly-insulator-poly (PIP) capacitor in the same process is $0.89 \text{ fF}/\mu\text{m}^2$. When using $R=1 \text{ M}\Omega$ and $C=1 \text{ pF}$, the resistor size of $1 \text{ M}\Omega$ is $55 \mu\text{m}^2$. When using $R=10 \text{ k}\Omega$ and $C=100 \text{ pF}$, the capacitor size of 100 pF becomes $350 \mu\text{m}^2$. The large resistance and capacitance in ASICs require a large area, which prevents us from equipping many channels in small area.

A multi-sampling method, however, can easily realize by utilizing a small capacitance of $\sim \text{pF}$. The gain of the multi-sampling circuit is determined by the number of sample

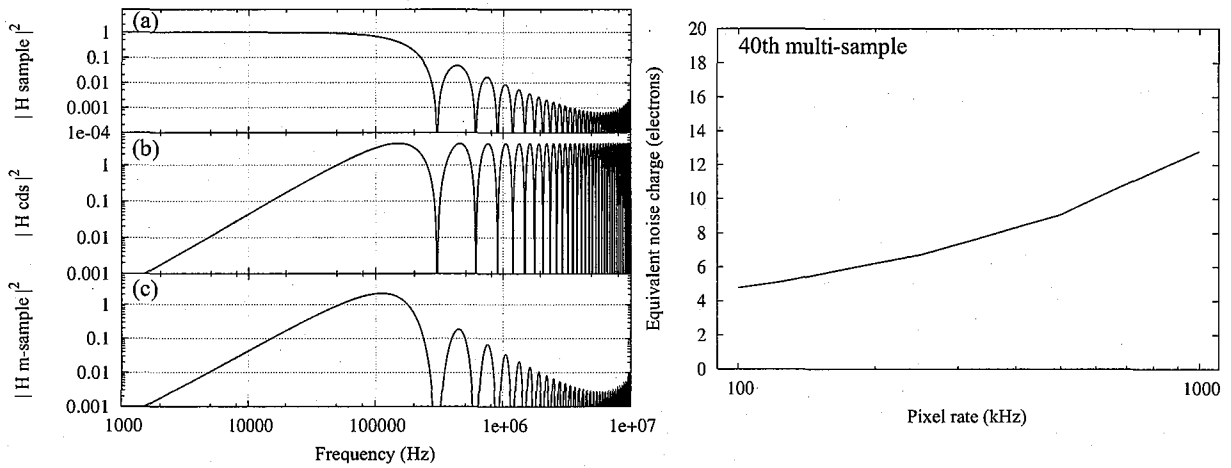


Figure 2.11: STFs of the sampling ($m=40$), CDS and multi-sampling method ($m=40$) at the pixel rate of 100 kHz (left). Equivalent noise charge in the multi-sampling method ($m=40$) as a function of a pixel rate (right).

and the ratio of the capacitance. We think that the multi-sampling method is better than the iCDS method in the term of a circuit architecture for ASICs.

2.3.3 ADC

An ADC converts a filtered analog signal to a digital signal for data acquisition. A conventional readout system for X-ray CCDs employ 12~14-bit ADC. Assuming the quantization noise (rms) = $\frac{1}{\sqrt{12}}$ Least Significant Bit (LSB), ADC resolution = 12-bit and dynamic range = 20 keV, we can calculate that the equivalent noise charge of the quantization noise is

$$\text{Noise}_{12\text{-bitADC}} = \frac{20 \text{ keV}}{4096 \times \sqrt{12} \times 3.65(\text{eV/e}^-)} \approx 0.4 \text{ e}^-. \quad (2.22)$$

It is too small to affect the total noise of the readout system. Because a typical pixel rate of X-ray CCDs is from 10 kHz to 1 MHz, the required specification of the ADC is a moderate conversion rate (a few MHz) and resolution (12~14-bit). A flash, pipeline and successive-approximation type ADCs are generally employed in readout systems for X-ray CCDs.

2.4 Energy resolution

Energy resolution in FWHM is generally applied to exhibit a spectroscopic capability for X-ray detectors. The theoretical energy resolution (eV) of CCDs (other Si detectors) including noise is described as

$$\text{FWHM} = 2.35 \times 3.65(\text{eV/e}^-) \sqrt{F \frac{E_x(\text{eV})}{3.65(\text{eV/e}^-)} + \sigma(\text{e}^-)^2} \quad (2.23)$$

where F is the Fano factor of Si, and σ is the equivalent noise charge derived from the readout noise, dark noise, transfer noise and so on. The readout noise is generated by the FDA and by the front-end electronics. The dark noise derived from carriers that are thermally generated. We can suppress the dark noise by cooling devices. The transfer noise (spurious charge) is caused by charges generated by impact ionization when transfer signals are clocked into inversion. This noise is reduced with decreasing the voltage swing of the clocks and with slowing the voltage change of the clock signals. (Janesick 2001) illustrates about these noises in detail. The measured energy resolution is better than the statistical value assuming a Poisson process because a part of an incident photon energy is expended by non-electron-hole processes (e.g., thermal). The Fano factor is utilized to compensate the difference between the statistical value and the measured value. We employed the Fano factor of 0.115 shown in (Janesick 2001) in this paper. The theoretical limit of energy resolution at 5.9 keV, Manganese (Mn) $K\alpha$, by using silicon detectors is given as

$$\begin{aligned} \text{FWHM at 5.9 keV} &= 2.35 \times 3.65(\text{eV/e}^-) \sqrt{0.115 \frac{5900(\text{eV})}{3.65(\text{eV/e}^-)}} \\ &= 117 \text{ eV}, \end{aligned} \quad (2.24)$$

which we call the Fano limit.

Chapter 3

ASICs

3.1 Overview of ASICs

We have been developing ASICs for X-ray CCD use. They contain four analog channels each of which consists of preamplifier, band-pass filter and ADC. Therefore, they receive analog inputs and send digital outputs. Since the ASIC is quite small, it can be placed very near the X-ray CCD output node so that we can reduce the length of the analog line to reduce the external noise. With taking into account the performance required and the maximum CCD output range of 40 mV, we set our goal of equivalent input noise level to be $30\ \mu\text{V}$ at 100 kHz pixel rate. We also expect it to function properly up to 1 MHz. Our ASIC project will enable anyone to easily construct the CCD camera system with very low noise and high pixel rate, which eliminates difficulties of tuning the analog electronics.

We have developed 4 types of ASICs that are named as Matsuura-Doty (MD01), Matsuura-Nakajima-Doty (MND01), MD02 and MND02. They are divided into 2 groups: one, a first group, contains MD01, MND01 and MD02 while the other contains MND02. MD01, the first ASIC developed in our series, properly functions as we designed, but there are some problems. They are the malfunction of LVDS circuit and the low maximum pixel rate as explained in Chap. 4. We designed the second ASIC, MND01, in order to solve these problems. We confirmed that they are properly solved, however, we encountered another problem that caused the degradation of INL and signal-to-noise ratio. The third ASIC developed, MD02, cleared these problems. Based on ASIC developments of the first group, we reached the ASIC, MND02, in which we reduced the noise figure of the preamplifier by 50% and improved the speed of LVDS receiver.

The circuit architectures of these ASIC are almost the same that will be briefly explained here. One ASIC chip has four readout channels as shown in Fig. 3.1. One readout channel consists of a preamplifier, 5-bit digital-to-analog converter (DAC) and two $\Delta\Sigma$

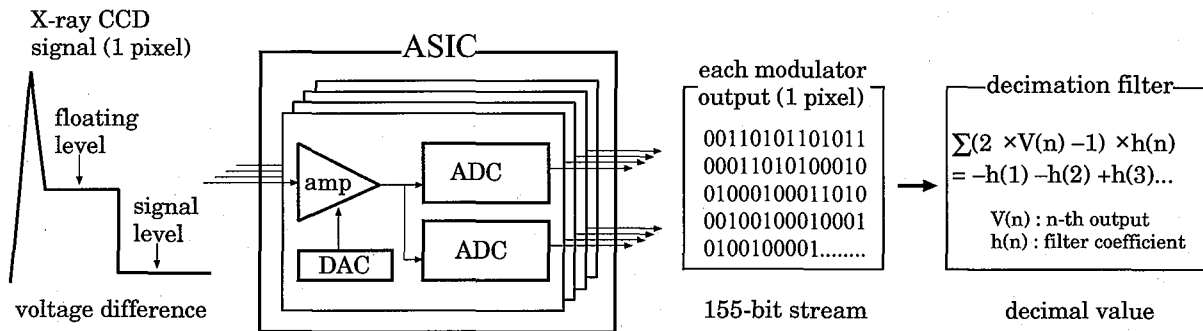


Figure 3.1: Data flow diagram of the readout system employing our ASIC.

ADCs that we call an odd ADC and an even ADC. The CCD signals are fed into ASIC through capacitors to remove DC component and converted from analog signals to digital bit-streams. Since the digital bit-streams are produced from the $\Delta\Sigma$ ADC, they have to be converted to the decimal values through the decimation filter. The following digital processor (DP) performs data acquisition and the decimation process.

The conventional circuit configuration for the readout of CCD signals consists of a preamplifier, band-pass filter and ADC as shown in Fig. 2.7. In the case of our ASICs, the $\Delta\Sigma$ ADCs function as the band-pass filter as well as ADC, so that the circuit configuration can be relatively simple compared with the ordinary readout systems.

The hierarchy of our ASICs is summarized in Table 3.1. The main circuit components, such as the preamplifier, 5-bit DAC and $\Delta\Sigma$ ADC, are explained in the following section. We employed “OPEN IP” for some circuit components, such as PADS and logic gates, in our ASIC design. The OPEN IP is the circuit blocks including both of analog and digital circuits developed for the smooth and certain ASIC designs especially for the high-energy physics and astronomical applications and released to the public in (OPEN IP web page). The fabrication process of our ASIC is a Taiwan Semiconductor Manufacturing Company (TSMC) 0.35 μm mixed signal CMOS technology. The power is a single-supply of 3.3 V. The chip size is 3 mm \times 3 mm and the chip is assembled into a quad flat package (QFP) with the size of 15 mm \times 15 mm as shown in Fig. 3.2.

3.2 Preamplifier

The preamplifier installed at the first stage of our ASIC is a differential voltage amplifier as shown in Fig. 3.3. It amplifies an AC-coupled CCD signal up to a factor of 10. The amplification factor can be controlled so that we can expand the dynamic range of the input of our ASIC. Our ASICs can process signals both of n-channel and of p-channel

Table 3.1: Hierarchy of our ASIC.

Top	Chain $\times 4$	Preamplifier	Operational amplifier
			DPST* switch
			Inverter and etc.
		5-bit DAC	D flip-flop
			DPST* switch
			NAND
			Inverter and etc.
		$\Delta\Sigma$ ADC $\times 2$	Switched capacitor circuit
			Comparator
			D flip-flop
			NAND
			Inverter and etc.
		Control signal generator	logic gates
		LVDS receivers, LVDS drivers, Bias circuit, Sync circuit [†] , PADs and etc.	

*dual pole single throw

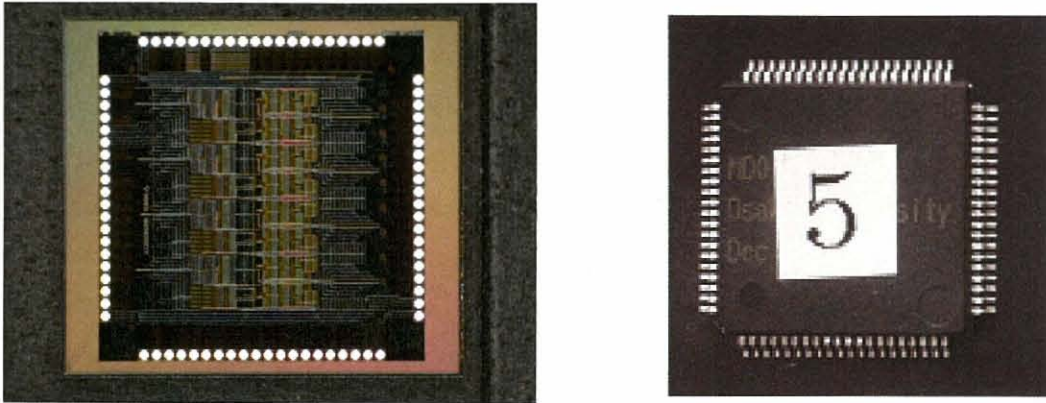
[†] Sync circuit synchronizes the control signals to sampling clock.

Figure 3.2: Photographs of the bare chip (left) and the assembled chip into a QFP (right).

CCDs by changing the input node of the preamplifier. The n-channel CCD signal shown in Fig. 2.3 (left) is fed into IN_+ node, while the p-channel CCD signal shown in Fig. 2.3 (right) is fed into IN_- node. Five-bit DAC signals through DAC_+ and DAC_- nodes are fed to adjust the offset voltage to the preamplifier output as explained in Sec. 3.3. Each output

can be described as

$$\text{OUT}_+ = -\frac{1\text{pF}}{1\text{pF}}\text{DAC}_+ \quad (3.1)$$

$$\text{OUT}_- = \frac{-3.6\text{pF}}{1\text{pF}} \left(\frac{3.6\text{pF}}{1\text{pF}}(\text{IN}_+ - \text{IN}_-) \right) - \frac{1\text{pF}}{1\text{pF}}\text{DAC}_- \quad (3.2)$$

$$\text{OUT}_+ - \text{OUT}_- = 12.96 (\text{IN}_+ - \text{IN}_-) - (\text{DAC}_+ - \text{DAC}_-) \quad (3.3)$$

Figure 3.4 is the simulation results of the preamplifier when the DAC signal is 0 mV and 100 mV. We confirmed the gain to be about 10 by the simulation result of Fig. 3.4 (left). This value is a little smaller than that of the simulation result in eq. (3.3). This is due to the fact that we treated the open loop gain of the operational amplifier and inverter as infinity. Through these simulation results, we confirmed that the DAC signal is properly subtracted from the preamplifier output.

The gains of the preamplifier in MD01 and in MD02 are fixed, while those in MND01 and in MND02 can vary from 1 to 10. The switchable capacitors are equipped in parallel with the capacitance of 1 pF so that the gain can be adjusted by connecting these capacitors. Since the output signal of CCD operated in the flux mode is relatively large compared with that of the photon counting mode, we determine the preamplifier gain to meet the voltage difference between the floating level and the signal level within the input range of the following ADC (± 200 mV). Therefore, the input range of ASICs, MND01 and MND02, cover the full well of CCDs. We expect to employ our ASICs for a readout of CCD signals not only in a photon counting mode but also in a flux mode.

3.2.1 Operational amplifier

The operational amplifier in the preamplifier operates on a single-supply of Vdd (3.3 V). Figures 3.5 and 3.6 are the schematic of the operational amplifiers in the first group ASICs and MND02 (hereafter referred to OP and QOP), respectively. The circuit architecture of OP is a differential amplifier, which is the basic configuration to amplify the voltage difference between input signals. M1 and M2 receive the input signals on the gates and convert each voltage to drain current. M3 acquires the reference voltage provided by the bias circuit on gate in order to drive a constant current. M4 and M5 configure a current-mirror circuit, copying the signal current generated by M1 as the drain current of M5. The output voltage is given by

$$V_{\text{out}} = g_m \frac{r_2 r_5}{r_2 + r_5} (\text{In}_+ - \text{In}_-) \quad (3.4)$$

where g_m is the transconductance of M1 and M2, r_2 and r_5 are the resistance value between drain and source of M2 and M5, respectively. Figure 3.7(left) shows the AC analysis result

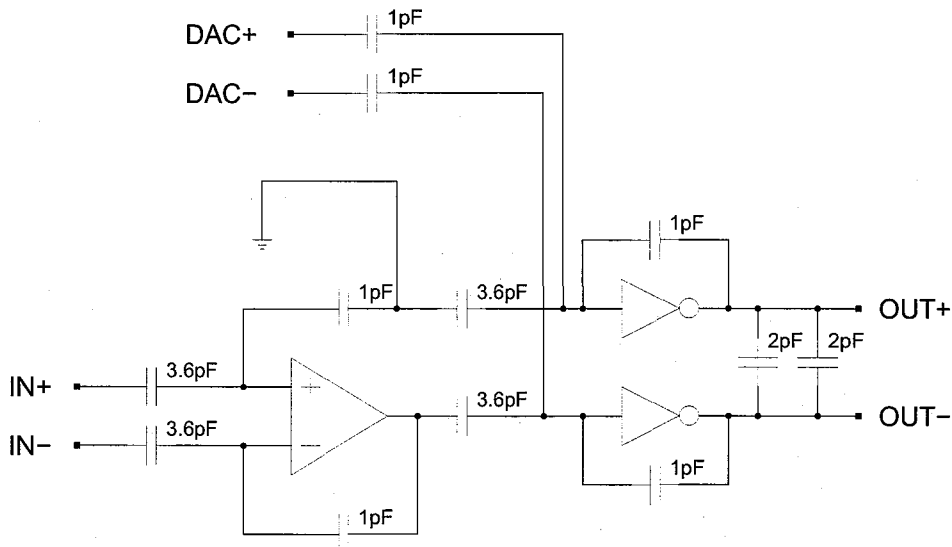


Figure 3.3: Block diagram of the preamplifier. The preamplifier consists of an operational amplifier and 2 inverters.

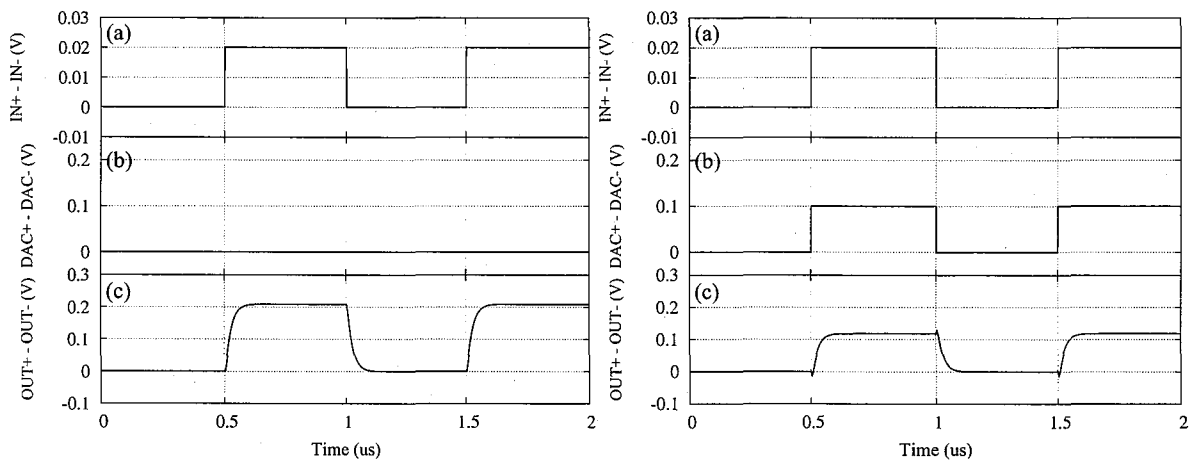


Figure 3.4: Simulation results of the preamplifier with DAC signals of 0 mV (left) and 100 mV (right). (a) is an input signal ($IN_+ - IN_-$), (b) is a DAC signal ($DAC_+ - DAC_-$) and (c) is an output signal ($OUT_+ - OUT_-$).

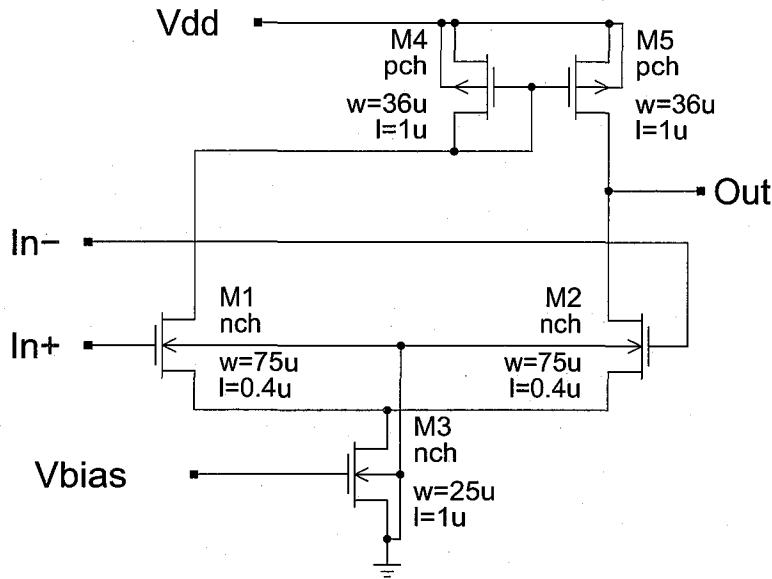


Figure 3.5: Schematic of the operational amplifier (OP) in first group ASICs.

of OP. The open loop gain of 33 dB is the typical value of this circuit architecture. Since the maximum pixel rate is about 1 MHz, the frequency characteristic sufficiently satisfies its requirement.

QOP is composed of the differential amplifier whose input MOSFETs are PMOSs, additional amplifier and capacitor for phase compensation. As shown in eq.(2.4), the flicker noise is proportional to the reciprocal of gate size ($W \times L$). We increased the total gate size from $75 \mu\text{m} \times 0.4 \mu\text{m}$ to $16 \times 25 \mu\text{m} \times 1 \mu\text{m}$. Additionally, the flicker noise of PMOS is a few times lower than that of NMOS. The expected noise of QOP decrease by 30~50% compared with that of OP by eq.(2.4). The noise characteristic of the preamplifier including OP and QOP is shown in Sec. 3.5.2.

3.3 5-bit DAC

There is a voltage difference of CCD signals between the floating and signal levels even no signal charge is fed. This comes from the feed-through of SG clock as shown in Sec. 2.1. We should eliminate it by a signal processing procedure. Assuming the input voltage difference of 50 mV, we calculated that the output signal of the preamplifier with the gain of 10 is 500 mV, which exceeds the input range of the ADC (± 200 mV). The output signal of 5-bit DAC is input into the preamplifier through DAC_+ and DAC_- nodes as shown

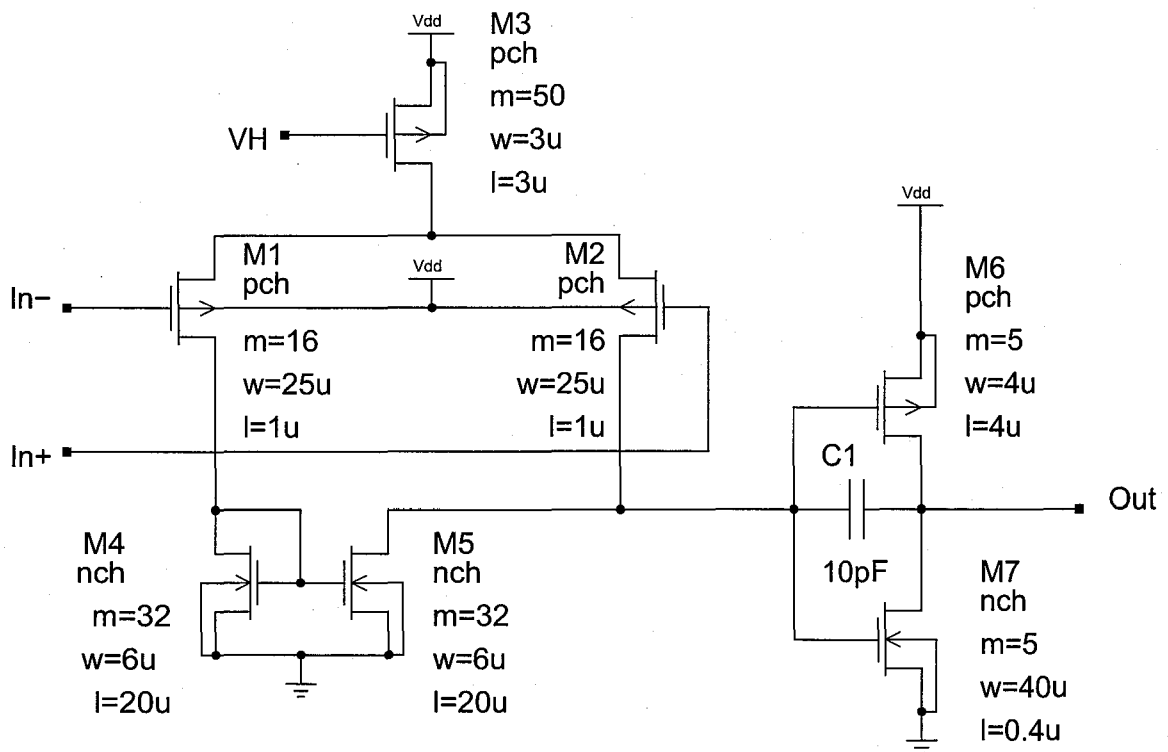


Figure 3.6: Schematic of the operational amplifier (QOP) in MND02.

in Fig. 3.3, eliminating such meaningless voltage difference in order to effectively use the dynamic range of following ADCs.

5-bit DAC in our ASICs is a capacitive binary-weighted DAC as shown in Fig. 3.8. This is the classic DAC first developed in 1920s (Rainey, P.M. patent 1921) and the backbone of the modern DACs. These are widely adapted to the circuit architecture of the successive-approximation ADCs. The circuit configuration of the binary-weighted DAC is very simple. Although it is difficult to fabricate the products with high resolution due to the precision of capacitance, its performance satisfies our requirements. The voltage of

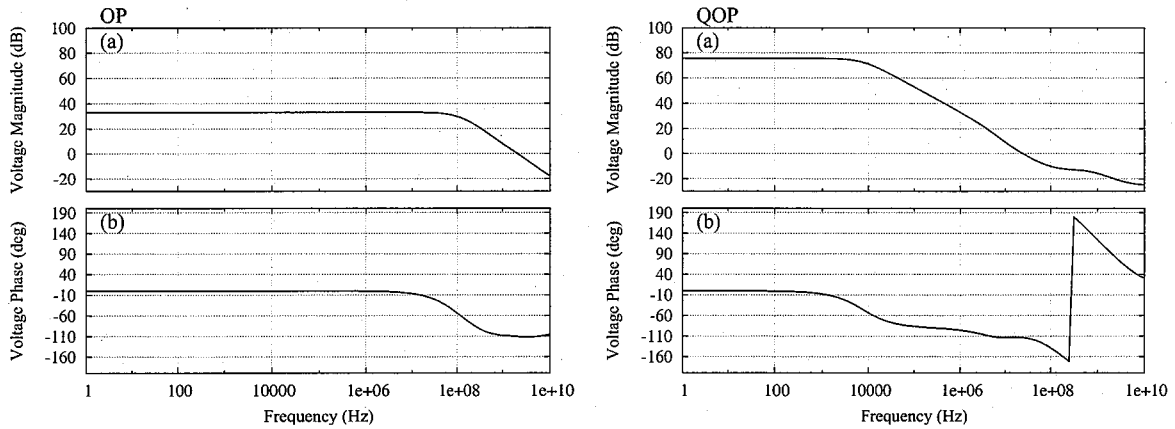


Figure 3.7: AC analysis results of the operational amplifiers (OP : left) and (QOP : right). (a) and (b) show the voltage magnitude and the voltage phase as a function of frequency, respectively.

each output is given by

$$\begin{aligned} \text{DAC}_+ = & \frac{(480 \text{ fF} \times V_1) + (240 \text{ fF} \times V_2) + (120 \text{ fF} \times V_3)}{1 \text{ pF}} \\ & + \frac{(60 \text{ fF} \times V_4) + (30 \text{ fF} \times V_5) + (30 \text{ fF} \times \text{VREF}_-)}{1 \text{ pF}} \end{aligned} \quad (3.5)$$

$$\text{DAC}_- = \frac{(960 \text{ fF} \times \text{VREF}_-)}{1 \text{ pF}} \quad (3.6)$$

where V_1 , V_2 , V_3 , V_4 and V_5 are the reference voltage for the capacitance string shown in Fig. 3.8. These voltage levels are determined to whether VREF_+ ($1.2 \text{ V} + \text{COM}$) or VREF_- (COM), where COM is the operating point voltage of the inverters. The DAC output can be finally described as

$$\text{DAC}_+ - \text{DAC}_- \sim \frac{\text{Din}}{32} \times 1.2 \text{ V} \quad (3.7)$$

where Din is the binary code loaded to the DAC register shown in Fig. 3.8. The DAC registers of 4 channels are cascaded so that we can set the DAC by only one data line (Din). Figure 3.9 (top) shows the format for Din of MD01 and MD02 which contains the 4 DAC codes of D4~D0 for channel-3, C4~C0 for channel-2, B4~B0 for channel-1 and A4~A0 for channel-0. In the case of MND01 and MND02, the register has both codes for the adjust of the preamplifier gain (Dp , Cp , Bp and Ap) and DAC (Dd , Cd , Bd and Ad) as shown in Fig 3.9 (bottom). Dclk is a serial clock to transfer Din into the serial shift register on the rising edge. Dload is a control input signal to latch the contents of the

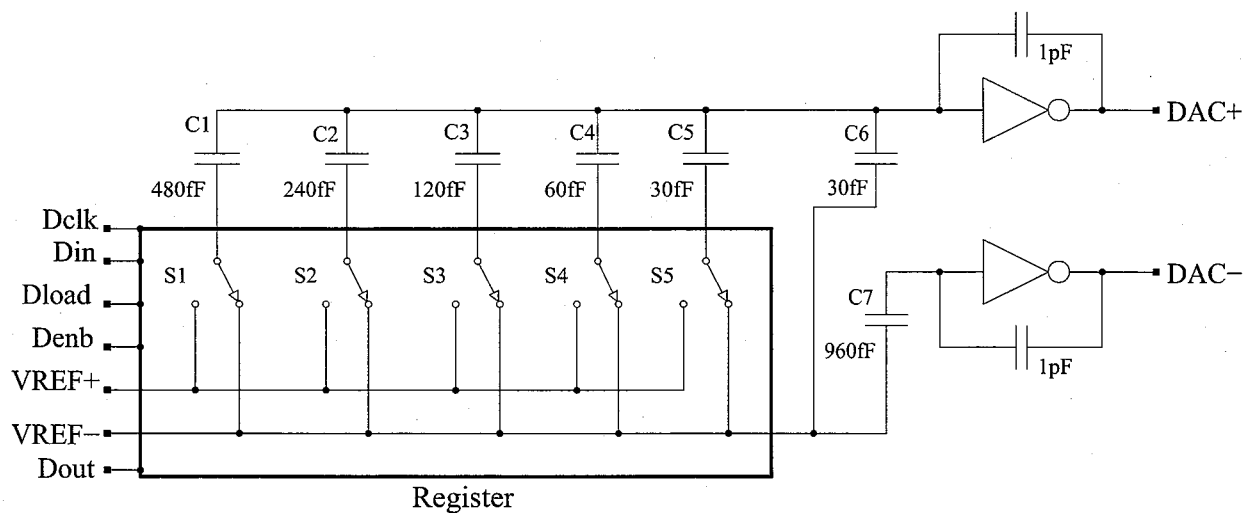


Figure 3.8: Block diagram of 5-bit DAC.

shift register on the rising edge of Dclk. Denb is a control input signal to power on the switches in the register, generating the setup voltage during the active level. Dout is the serial data out of Din through the register. The Dout of channel-0 is connected to the Din of channel-1 and the Dout of channel-3 is finally transferred outside an ASIC. Figure 3.10 shows the simulation result of 5-bit DAC with D_{in} (for 1 channel) = 16. The output voltage obtained by this simulation is 550 mV, which is comparable to the expected value of 600 mV from eq.(3.7).

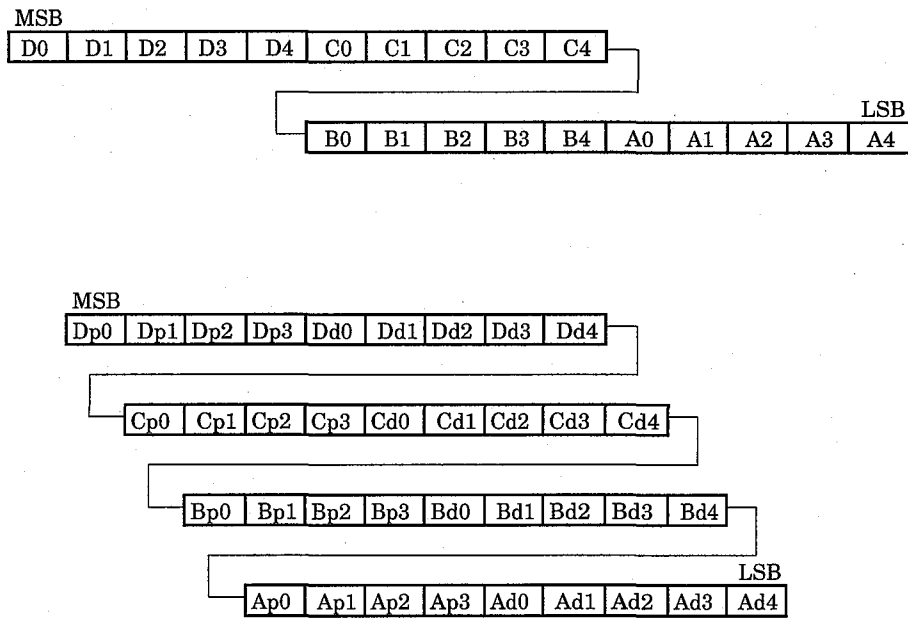


Figure 3.9: Data formats for the serial register for 5-bit DAC and preamplifier gain in MD01 and MD02 (top), and MND01 and MND02 (bottom).

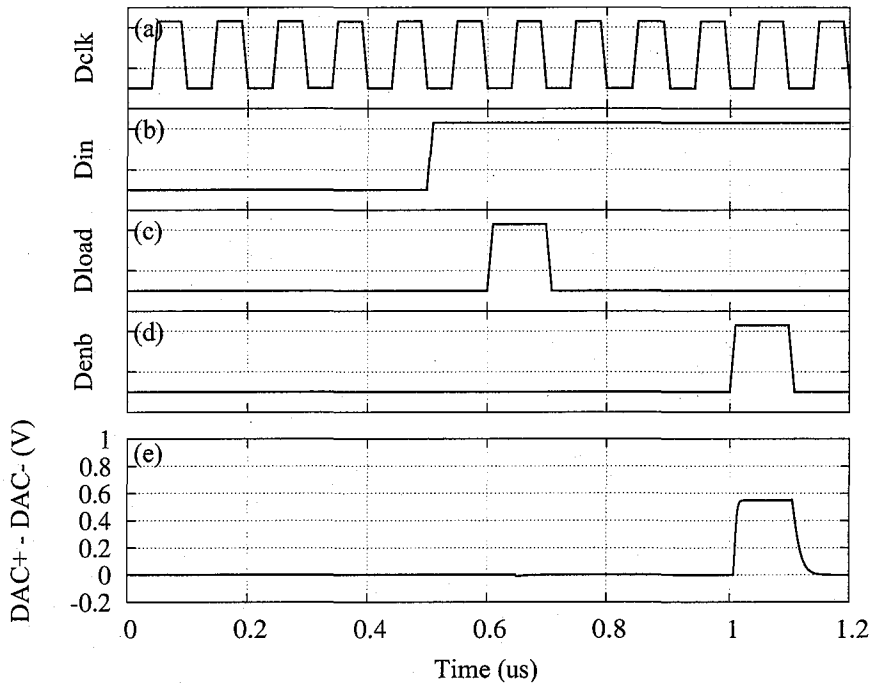


Figure 3.10: Simulation result of 5-bit DAC. (a) is Dclk, (b) is Din(for 1 channel) = 16, (c) is Dload, (d) is Denb and (e) is the DAC output ($DAC_+ - DAC_-$).

3.4 $\Delta\Sigma$ ADC

In general, there are two types of ADCs, a Nyquist-rate converter and an oversampled converter. The Nyquist-rate converters, such as flash ADC, slope ADC and cyclic ADC, perform Analog to Digital conversion by using a single sampled analog signal. The oversampled converters utilize a sequential data sampling at high frequency compared with that of the input signal. A decimal output of the oversampled ADC is obtained by the decimation process for noise and sample rate reduction.

We employed the oversampled converter, $\Delta\Sigma$ ADC, because this type of ADC

- can achieve a high resolution at a moderately short conversion time.
- does not need accurate circuit components.
- can be fabricated by a low cost CMOS process.
- functions not only as an ADC but also a band-pass filter.

The differential averaging function can be implemented in $\Delta\Sigma$ ADC as explained in Sec. 3.4.2, which is not automatically in Nyquist-rate converters. The $\Delta\Sigma$ ADC enables us to remove a band-pass circuits from the readout system and simplify the circuit configuration.

3.4.1 Concept of $\Delta\Sigma$ ADCs

Fig. 3.11 shows an example block diagram of a first-order $\Delta\Sigma$ ADC (a) and its signal diagram (b). The ADC consists of a sampling circuit (a switched-capacitor circuit), integrator, comparator (1-bit ADC), flip-flop and 1-bit DAC. The number of cascading pairs of sampling circuit and integrator represents the order of $\Delta\Sigma$ ADC. The sampling circuit outputs the charges to the integrator, the amount of which is proportional to the input voltage. The comparator followed by the D flip-flop compares the output of the integrator with a reference voltage and outputs the clocked bitstream. When the output of the integrator is higher than the reference voltage, the logic level of the output bit becomes high. The 1-bit DAC, subsequently, subtracts the reference charges from the integrator to regulate the output voltage of the integrator. Therefore, the frequency of high level in the output bitstream increases as the input signal gets larger. Figure 3.12 shows the simulation results of the $\Delta\Sigma$ ADC. The density of high level in the output bitstream in Fig.(b) is changing with the input signal voltage in Fig.(a).

noise shaping

Figure 3.13 shows the z-domain model of the first-order $\Delta\Sigma$ ADC shown in Fig. 3.11(a). The parameter "z" represents " $e^{sT_{\text{clk}}}=e^{j2\pi fT_{\text{clk}}}$ ", where j is imaginary unit, f is frequency

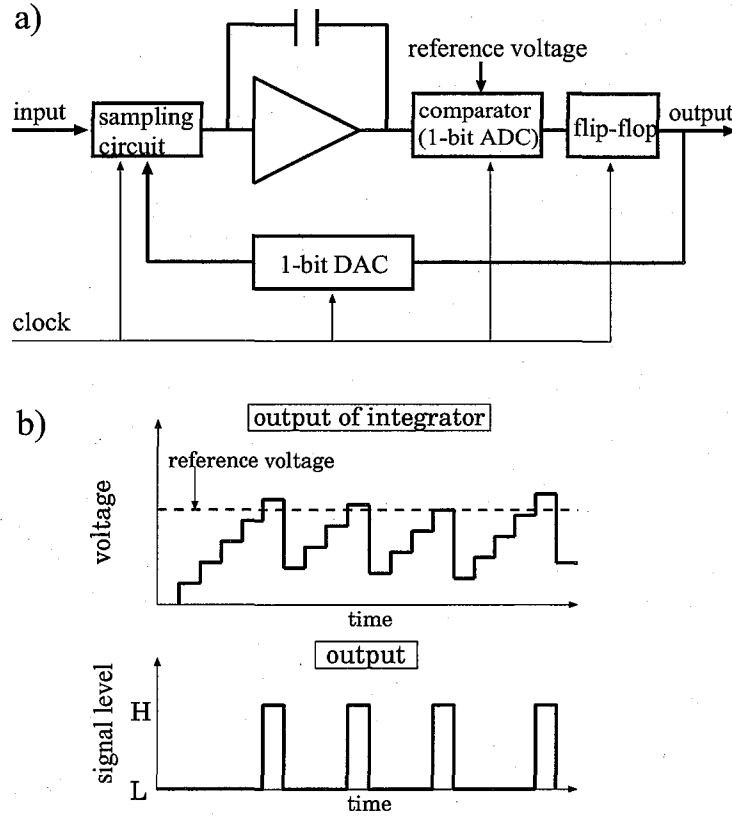


Figure 3.11: Block diagram of a basic first-order $\Delta\Sigma$ ADC (a) and its signal diagram (b).

and T_{clk} is the sampling-to-sample time. The z -domain model is utilized to describe a STF of a discrete time-domain system. An output of a first-order $\Delta\Sigma$ ADC in z -domain is given as

$$\begin{aligned}
 V(z) &= Y(z) + E(z) \\
 &= U(z) - V(z-1) + Y(z-1) + E(z) \\
 &= U(z) - Y(z-1) - E(z-1) + Y(z-1) + E(z) \\
 &= U(z) + (1 - z^{-1}) E(z),
 \end{aligned} \tag{3.8}$$

where $U(z)$ is an input signal, $Y(z)$ is an integrator output, $E(z)$ is a quantization noise and $V(z)$ is an ADC output. The term of “ $1 - z^{-1}$ ” is called the noise transfer function (NTF) (Richard, S. et al. 2005). Assigning $z^{-1} = e^{-j2\pi f T_{\text{clk}}}$ into eq. (3.8), the frequency response is described as

$$V(f) = U(f) + 2\sin(\pi f T_{\text{clk}}) E(f). \tag{3.9}$$

The noise power spectrum of a $\Delta\Sigma$ ADC ($E(f)$) becomes very large compared with that of Nyquist ADCs due to a 1-bit ADC employed in the circuit architecture. Since the factor

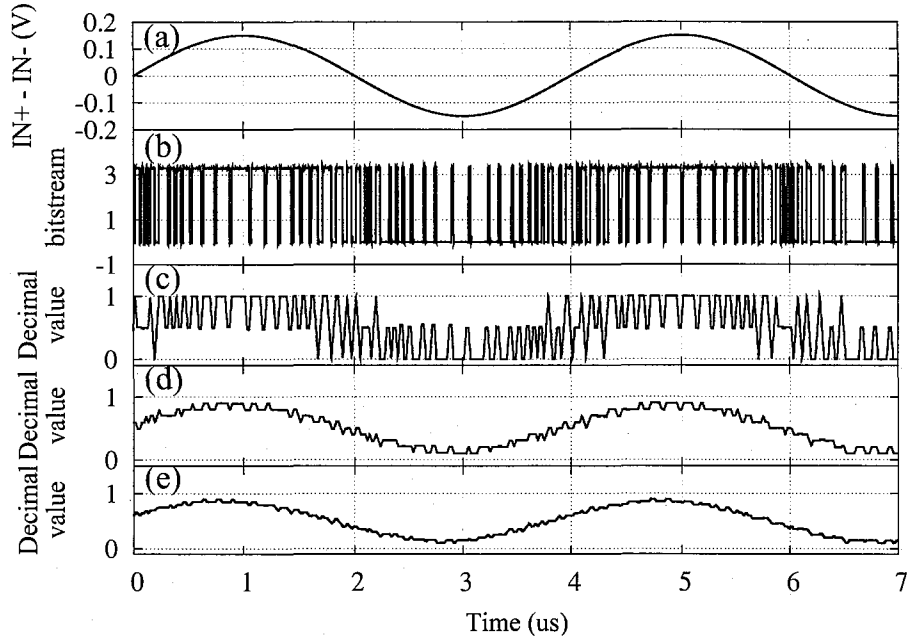


Figure 3.12: Simulation results of $\Delta\Sigma$ ADC. (a) is an analog input signal, (b) is an output bitstream. (c), (d) and (e) are the normalized decimal values by using a running average filter with the length of 100, 500 and 1000, respectively.

of $2 \sin(\pi f T_{\text{clk}})$ in eq.(3.9) functions as a high-pass filter, the $\Delta\Sigma$ ADC can attenuate the quantization noise at the low frequency, around signal frequency band. This is the main feature of the $\Delta\Sigma$ ADC, which is called “noise shaping”. In the case of the N-th order $\Delta\Sigma$ ADC, its frequency response is approximately expressed as

$$V(f) = U(f) + (2 \sin(\pi f T_{\text{clk}}))^N E(f). \quad (3.10)$$

Assuming $T_{\text{clk}}=1$ where Nyquist frequency is 0.5, Fig. 3.14 shows the magnitude of the NTFs of first-order (NTF1), second-order (NTF2), third-order (NTF3) and fourth-order (NTF4) $\Delta\Sigma$ ADCs. We can confirm that the noise shaping effect suppresses the quantization noise down to tiny level at the low frequency.

decimation filter

$\Delta\Sigma$ ADCs suppress the quantization noise at the low frequency compared to the sampling frequency. To obtain the pulse height with high precision, we should remove the quantization noise at high frequency from the output bitstream. A decimal value is obtained by the decimation process that calculates the weighted average of bitstream. A decimation process is considered as a digital low-pass filter and effectively removes the high

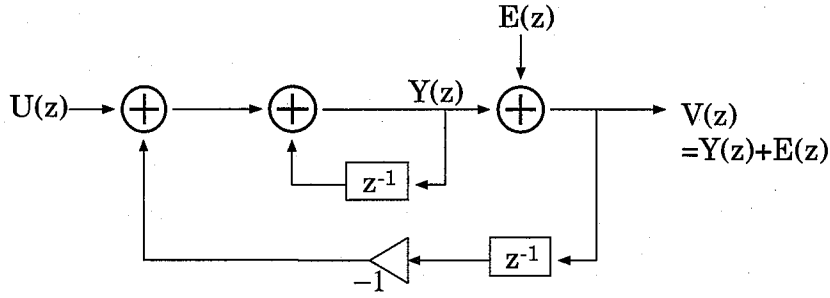


Figure 3.13: z-domain model for the first-order $\Delta\Sigma$ ADC shown in Fig. 3.11

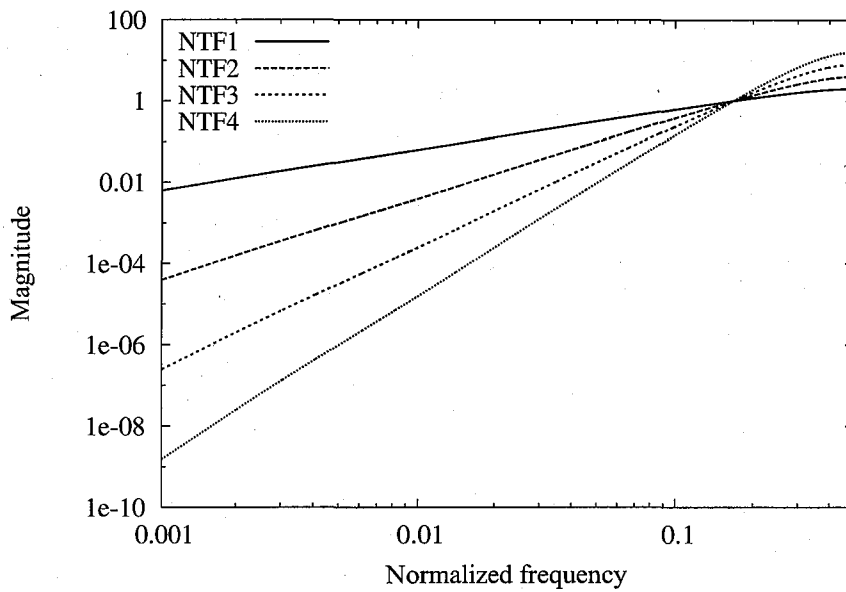


Figure 3.14: NTFs of first, second, third and fourth-order $\Delta\Sigma$ ADCs.

frequency part of the output noise. The combination of noise shaping and decimation process enables $\Delta\Sigma$ ADC to achieve higher resolution than other types of ADCs.

The simplest filter is to calculate a simple average of bitstream, which is called “sinc filter”. Its STF in z-domain is given as

$$H_{\text{sinc}}(z) = \frac{1}{N}(1 + z^{-1} + z^{-2} + \dots + z^{-(N-1)}) = \frac{1}{N} \frac{1 - z^{-N}}{1 - z^{-1}} \quad (3.11)$$

where N is the data length during one decimation process. This frequency response can be described as

$$H_{\text{sinc}}(f) = \frac{1}{N} \frac{2\sin(N\pi f T_{\text{clk}})}{2\sin(\pi f T_{\text{clk}})} \quad (3.12)$$

As shown in eq.(3.8), the quantization noise of the first order $\Delta\Sigma$ ADC is given as

$$P_{\text{ADC}}(z) = (1 - z^{-1})E(z). \quad (3.13)$$

The quantization noise after a sinc filter with the data length of N is calculated as

$$\begin{aligned} Q(z)_{\text{ADC sinc1}} &= \frac{1}{N} \sum_{i=0}^{N-1} P_{\text{ADC}}(z - i) \\ &= H_{\text{sinc}}(z) \times P_{\text{ADC}}(z) \\ &= \frac{1}{N} \frac{1 - z^{-N}}{1 - z^{-1}} \times (1 - z^{-1})E(z) \\ &= \frac{1}{N} (1 - z^{-N})E(z). \end{aligned} \quad (3.14)$$

Equation 3.14 in time domain can be described as

$$Q(n)_{\text{ADC sinc1}} = \frac{1}{N} (E(n) - E(n - N + 1)) \quad (3.15)$$

where n is the number of signal process. $E(n)$ and $E(n - N + 1)$ are the quantization noise of 1-bit ADC (σ_{rms}). Assuming $E(n)$ is not correlated with $E(n - N + 1)$, we can obtain the quantization noise power by

$$\begin{aligned} \sigma_{\text{ADC sinc1}}^2 &= \frac{2\sigma_{\text{rms}}^2}{N^2} \\ \frac{\sigma_{\text{ADC sinc1}}^2}{\sigma_{\text{rms}}^2} &= \frac{2}{N^2} \end{aligned} \quad (3.16)$$

Equation(3.16) shows the theoretical achievable resolution of the system composed of a first-order ADC and sinc filter. The quantization noise decreases with increasing the data length. For example, the normalized filtered values obtained by using the running average filters with various data length are shown in Fig. 3.12 (c)(d)(e). We confirmed that the accuracy of the decimal value by using the long filter is high as we expected from eq.(3.16).

Another method to improve the ADC resolution is to use a sinc M filter. The convolution of M sinc filters is written as ‘‘sinc M filter’’ in this paper. Its STF s in z -domain and in frequency domain are

$$H_{\text{sincM}}(z) = \left(\frac{1 - z^{-N}}{N(1 - z^{-1})} \right)^M \quad (3.17)$$

$$H_{\text{sincM}}(f) = \left(\frac{1 - 2\sin(N\pi f T_{\text{clk}})}{N \cdot 2\sin(\pi f T_{\text{clk}})} \right)^M \quad (3.18)$$

Figure 3.15 shows the STF s of sinc, sinc2 and sinc3 filters with $N=100$. For example, the noise power of the first-order ADC by using the sinc2 filter is calculated in the same way

as eq.(3.14);

$$\begin{aligned}
 Q(z)_{\text{ADC sinc2}} &= H_{\text{sinc2}}(z) \times P_{\text{ADC}}(z) \\
 &= H_{\text{sinc1}}(z) \times H_{\text{sinc1}}(z) \times P_{\text{ADC}}(z) \\
 &= H_{\text{sinc1}}(z) \times \frac{1}{N}(1 - z^{-N})E(z).
 \end{aligned} \tag{3.19}$$

The factor of $H_{\text{sinc1}}(z)$ means to calculate the average. Equation 3.19 in time domain is

$$Q^{(n)}_{\text{ADC sinc2}} = \frac{1}{N} \sum_{i=0}^{N-1} \left(\frac{1}{N} (E(n-i) - E(n-N+1-i)) \right). \tag{3.20}$$

The noise of the first-order ADC with sinc2 filter is

$$\begin{aligned}
 \sigma_{\text{ADC sinc2}}^2 &= \frac{N \times 2\sigma_{\text{rms}}^2}{N^4} \\
 &= \frac{2\sigma_{\text{rms}}^2}{N^3}.
 \end{aligned} \tag{3.21}$$

A sinc2 filter effectively reduces the quantization noise compared with a sinc filter in eq.(3.16). A sinc(L+1) filter is generally appropriate for the L-th order $\Delta\Sigma$ ADC (Richard, S. et al. 2005). The theoretical noise power of the system composed with the L-th order ADC and sincM filter is given by

$$\sigma_{\text{ADCL sincM}}^2 = \frac{2^L}{N^{L+M}} \sigma_{\text{rms}}^2. \tag{3.22}$$

The achievable resolution of a first-order and of a second-order ADC employing several decimation filters can be calculated by eq.(3.22). We show these results in Fig. 3.16. To realize the effective 12-bit resolution ($\frac{1}{4096}$) within the appropriate data length (~ 100 samples), we need a second-order system and a sinc2 or sinc3 filter.

3.4.2 $\Delta\Sigma$ ADC implemented in our ASICs

We need to design the ADC composed of a second-order ADC and a decimation filter of sinc2 or sinc3 to realize 12-bit resolution in a moderate data length of 100 as shown in Fig. 3.16. The $\Delta\Sigma$ ADC in our ASICs shown in Fig. 3.17 is a combination of the first-order and the second-order systems to increase the noise shaping effect and to stabilize the system. The circuit configuration of the ADC is a differential circuit to remove the common noise. A sampling circuit can change the output polarity and break the output charges by handling the logic level of D_+ and D_- nodes. The sampling circuit placed at the ADC input is "premodulaor" as explained below. The sampling circuit with $V_{\text{ref+}}$ and $V_{\text{ref-}}$ functions as a 1-bit DAC in feedback loop as shown in Fig. 3.11 (a). The reference

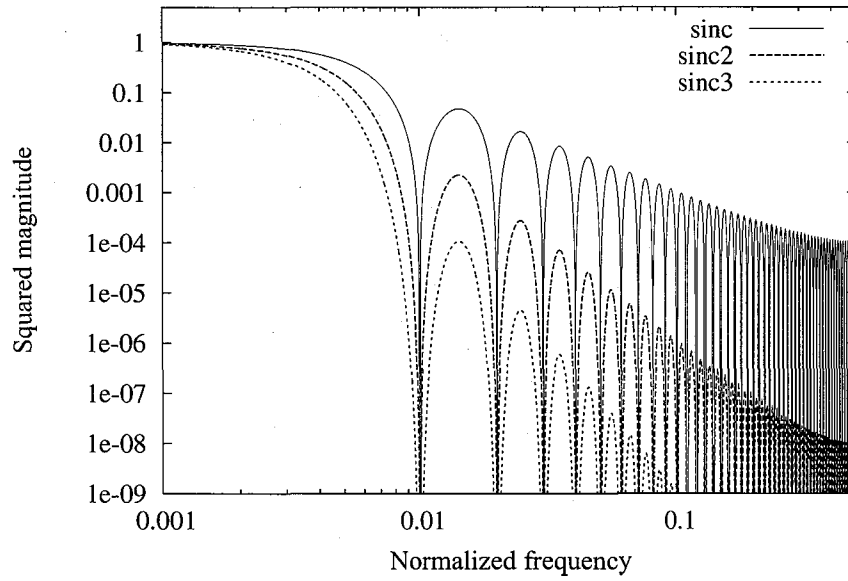


Figure 3.15: STFs of sinc, sinc2 and sinc3 filters calculated by eq.(3.18) with $N=100$.

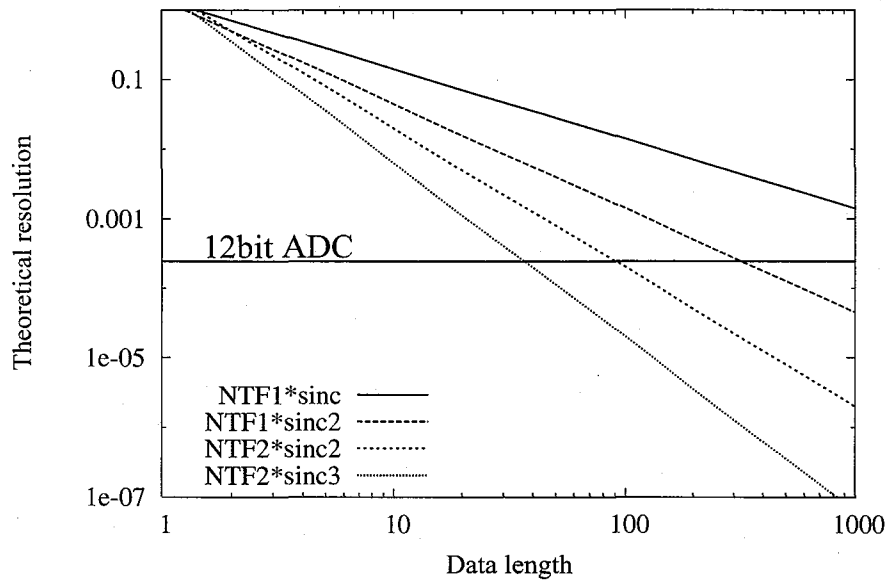


Figure 3.16: Theoretical resolution as a function of a data length. The resolution of 12-bit is also shown in this figure.

voltages of V_{ref+} ($0.2V+COM$) and V_{ref-} (COM) determine the input range of the $\Delta\Sigma$

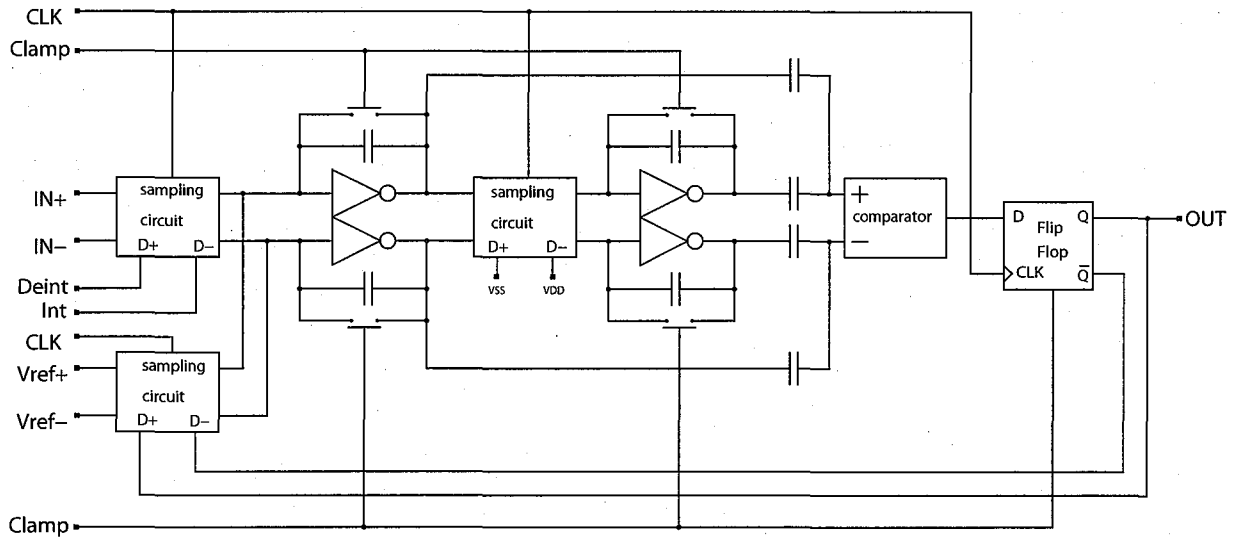


Figure 3.17: Block diagram of $\Delta\Sigma$ ADC in our ASICs. It consists of sampling circuits, a comparator, a D flip-flop, inverter and so on.

ADC (± 0.2 V), where COM is the operating point voltage of the inverters.

Figure 3.18 shows the impulse responses (filter coefficient) of sinc, sinc2 and sinc3 filters with $N=32$. For example, that of sinc2 is calculated by convolving two impulse responses of sinc filter with $N=32$. The data length of sinc2 filter with $N=32$ is $32 \times 2 = 64$. Therefore, we need to increase the data length when employing the high-order sinc filter. If we peg the data length of the filter coefficient to N , eqs. (3.17) and (3.18) can be rewritten as

$$H_{\text{sinc}M}(z) = \left(\frac{1}{(N/M)} \frac{1 - z^{-(N/M)}}{1 - z^{-1}} \right)^M \quad (3.23)$$

$$H_{\text{sinc}M}(f) = \left(\frac{1}{(N/M)} \frac{2\sin((N/M)\pi f T_{\text{clk}})}{2\sin(\pi f T_{\text{clk}})} \right)^M \quad (3.24)$$

Figure 3.19 shows the STFs of sinc, sinc2 and sinc3 with $N=100$ calculated by eq. (3.24). The functions of sinc2 and sinc3 as low-pass filter are clearly degraded compared with Fig. 3.15. In the readout system of CCDs, we can not extend the data length without the decrease of pixel readout rate or the increase of sample rate because a CCD output is a successive signal. We need to function the digital circuits at high speed as the sample rate increases, which makes the high pixel rate difficult.

We, consequently, implemented the gate which we called “premodulator” in the $\Delta\Sigma$ ADC as shown in Fig. 3.20 (Doty, J. P. patent 2006a, Doty, J. P. et al. 2006b). In our ASICs, premodulator restricts the input signal and enables us to extend the data length to 2-pixel length without being affected as mentioned above. Additionally, the premodulator

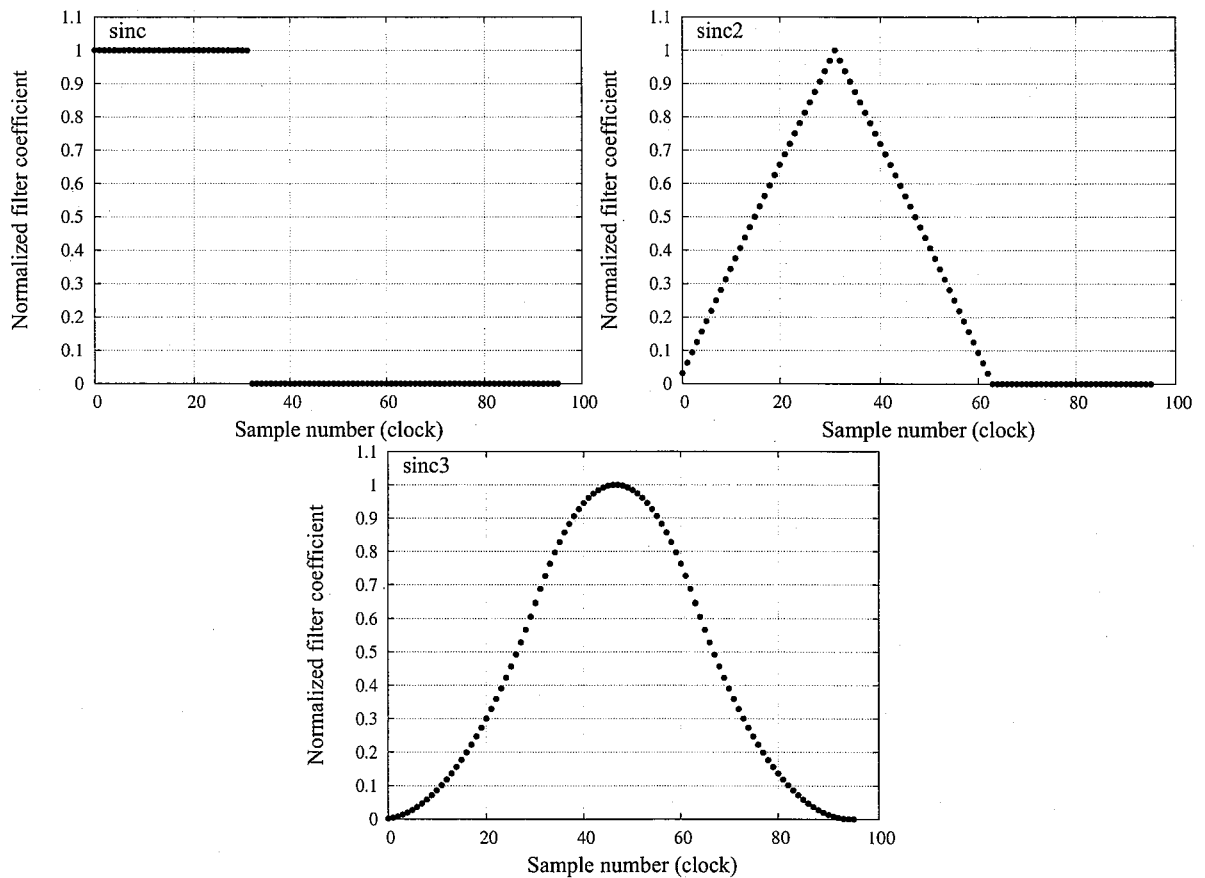


Figure 3.18: Impulse responses of sinc, sinc2 and sinc3 filters with $N=32$.

multiplies the CCD signal by the differential averaging function shown in Fig 3.20. The conventional $\Delta\Sigma$ ADC successively samples an input signal during the conversion time. While, the operation of the $\Delta\Sigma$ ADC in our ASICs transits 4 phases during 1 conversion time corresponding to 2-pixel readout time as shown in Fig. 3.21. We pegged the data length to $N=160$ and the numbers in Fig. 3.21 show each operation length. The weight for premodulator shown in Fig 3.20 changes with the operation phases of the ADC.

During Reset phase (when the control signal of Clamp shown in Fig. 3.17 is clocked high), the ADC is reset. During Deint phase (when Deint signal is clocked high), the ADC samples the voltage of the floating level. During Int phase (when Int signal is clocked high), the ADC samples the signal level with the premodulator weight of -1 in order to correlate the floating level with the signal level. Therefore, the ADC also functions as a band-pass filter. During Post phase (when Clamp, Deint and Int signals are clocked low), the ADC does not sample an input signal because premodulator isolates the input from the ADC, and continues to perform AD convention without an input signal. Since

the ADC output during Post phase also includes a quantization noise, we can improve the ADC resolution by utilizing these data. The two ADCs (even ADC and odd ADC) function one another at a time difference of 1 pixel readout time.

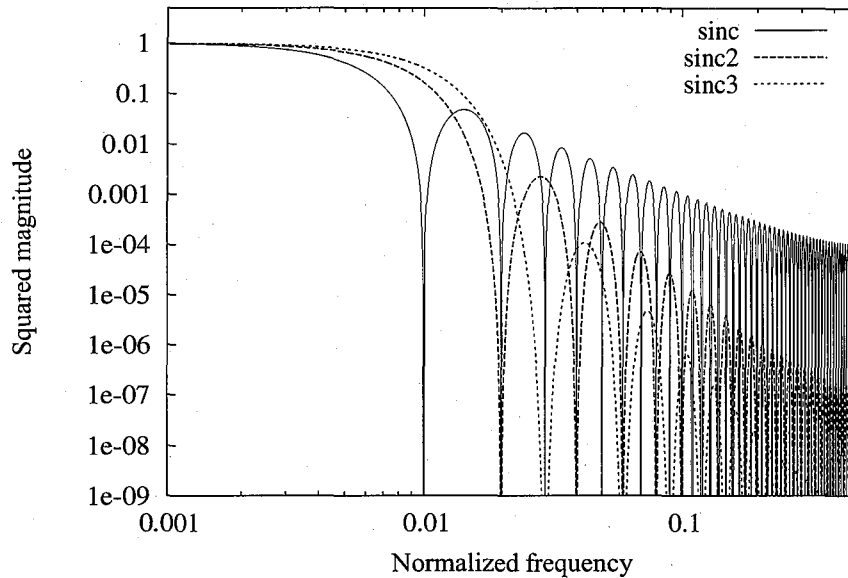


Figure 3.19: STFs of sinc, sinc2 and sinc3 filters calculated by eq.(3.24) as the length of the filter coefficient peg to 100.

decimation filter

The general decimation filters are sinc filters or Finite Impulse Response (FIR) filters which are calculated from the data length, cut-off frequency and attenuation factor. The responses of these filters are symmetric as shown in Fig. 3.18. The operation of our $\Delta\Sigma$ ADC, however, is different from that of the ordinary ones. Since the SN ratio decreases when using the symmetric filters, we designed the decimation filter by the least square method. The output of the $\Delta\Sigma$ ADC contains the input signal and quantization noise components shown in eq.(3.8). The weighted average of its output signal can be described as

$$\begin{aligned}
 \text{input} &= \sum_{i=1}^{155} V(i) \times h(i) \\
 &= \sum_{i=1}^{155} U(i) \times h(i) + \sum_{i=1}^{155} (1 - z^{-1})E(i) \times h(i) \\
 U(i) &= 0, \text{ if } (i > 70)
 \end{aligned} \tag{3.25}$$

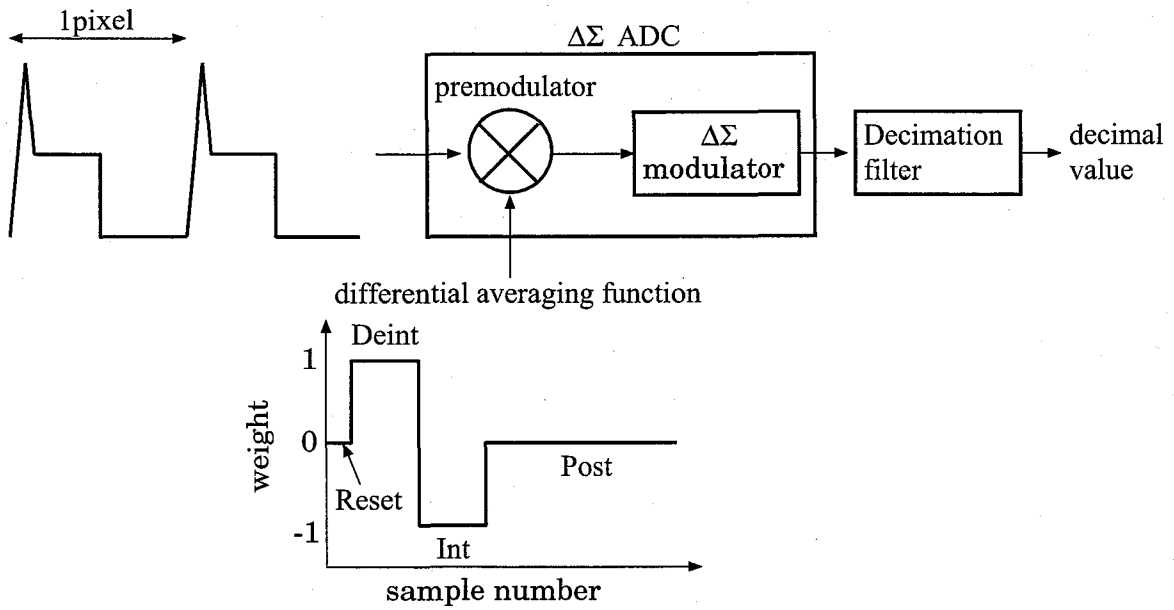


Figure 3.20: Block diagram for the explanation of the premodulator function.

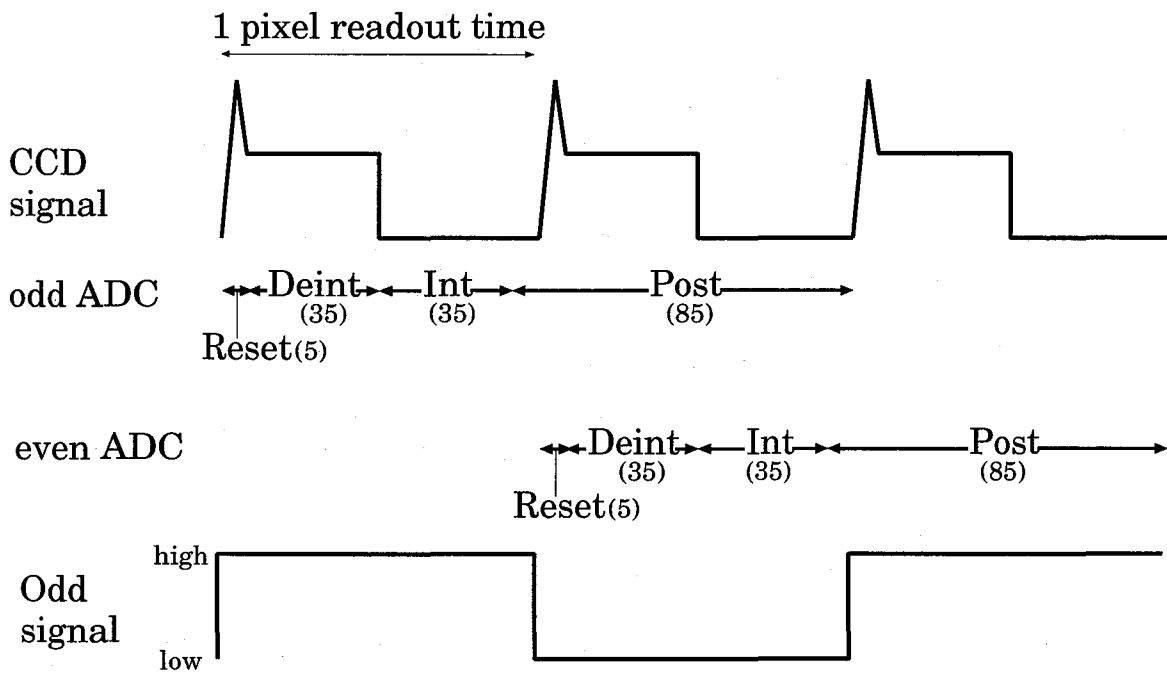


Figure 3.21: Data process diagram of the $\Delta\Sigma$ ADC in our ASICs.

where input is the voltage difference between the floating level and the signal level and $h(i)$ is the i -th filter coefficient. The error of quantization noise ($E(i)$), white noise, is considered as the normal distribution. We can calculate filter coefficients which minimizes the deviation between the model and data by the least square method. To perform

this calculation, we first constructed the $\Delta\Sigma$ ADC simulator employing *Mathematica*. The simulation using the input signals of 10,000 patterns yielded the decimation filter coefficient for our ASICs shown in Fig. 3.22. This filter coefficient is scaled as the dynamic range of the filtered value corresponds to ± 1 . The shape of the calculated filter is quite similar to the response of sinc3 except at the rising part. The decimal values of our ASIC output are obtained by

$$\text{Decimal value} = \sum_{i=1}^{155} (2 \times V(i) - 1) \times h(i). \quad (3.26)$$

Note that $V(i)$ is 1 when the logic level of output is high, while $V(i)$ is 0 when that is low in eq.(3.26). We show the decimal value obtained by eq.(3.26) as a function of the sample number in Fig. 3.23 when the voltage of the floating = 0 mV and that of the signal = -15 mV (filled circle) and noinput (open circle). From Fig. 3.23, we can verified that the decimal value is approximately determined during *Deint* and *Int* phases (up to 70 clocks) and converges during *Post* phase.

The decimation filter is not included in ASICs as shown in Fig. 3.1 in order to reduce the circuits size, power consumption and noise. The filter is implemented in a field programmable gate array (FPGA) to realize the real-time filtering. In future work, we plan to develop an ASIC for a decimation filter. We will assemble it with an readout ASIC into one package.

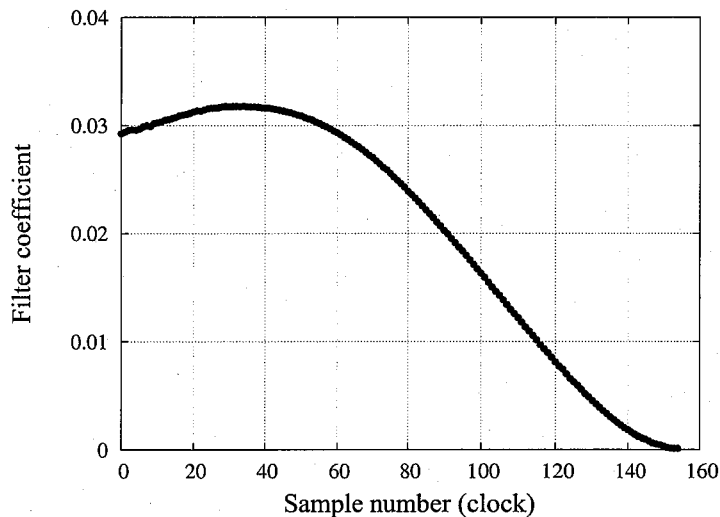


Figure 3.22: Filter coefficient of our ASIC as a function of sample number.

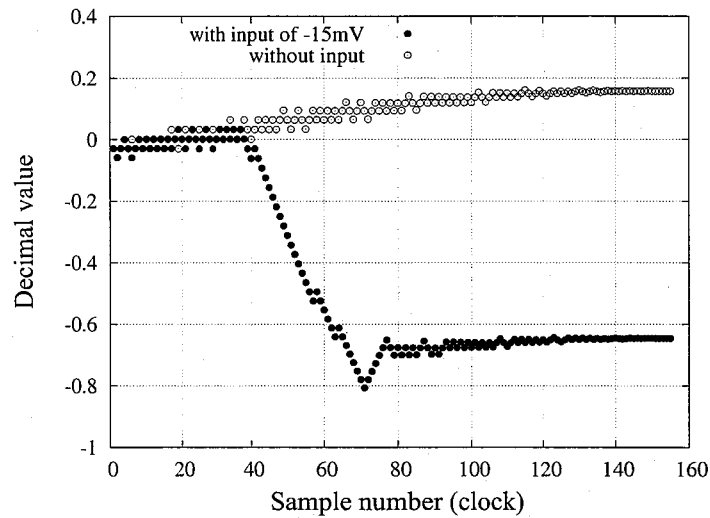


Figure 3.23: Decimal value as a function of the sample number. The filled circle shows the result with the input of -15 V and the open circle shows that without input.

3.5 Chain

The chain consists of a preamplifier, a 5-bit DAC, 2 $\Delta\Sigma$ ADCs and a control signal generator as shown in Table 3.1 and in Fig. 3.24. The signal generator that is composed of some logic gates transmits the control signals to 2 ADCs. Odd signal shown in Fig. 3.21 AND the control signals, such as *Clamp*, *Deint* and *Int* signals, yield the operation signals for odd ADC, while inverted *Odd* signal AND the control signals yield those for even ADC. *Odd* signal determines which ADC samples the input data. *Int* signal is also utilized for *Denb* signal in 5-bit DAC to generate the DAC signal during the AD conversion of the signal level. The test points are equipped with the output of the preamplifier to check the amplified signals outside the ASIC. The chain processes one CCD signal and there are 4 chain blocks in one chip as shown in table 3.1. The simulation results of the chain are shown in Fig. 3.25.

3.5.1 Integral Non-Linearity (INL)

Figure 3.26 shows decimal values as a function of the voltage difference between the floating level and the signal level. We fitted the simulation results with the model of linear function and constant. The integral non-linearity (INL) by the best-fit method is calculated as

$$\text{INL} = \frac{2(\text{maximum residual})}{\text{dynamic range}} \times 100. \quad (3.27)$$

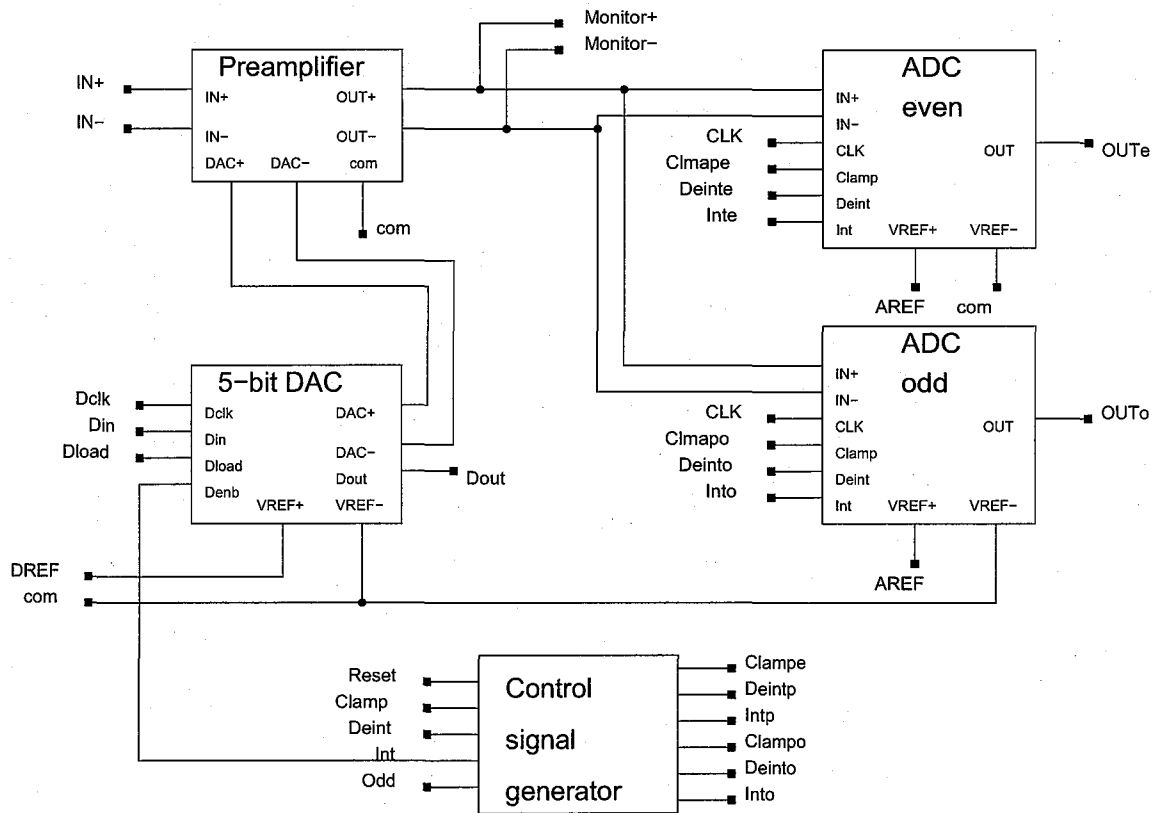


Figure 3.24: Block diagram of the chain.

INL is the important specifications to exhibit the ADC linearity. The simulation result of our ADC shows the INL $\sim 0.2\%$.

3.5.2 Noise performance

The noise from the preamplifier is generally dominant in that of the total readout system. We need to reduce the preamplifier noise in order to develop the readout system with low noise. Figure 3.27 shows the noise spectrum density of the preamplifiers in the first group ASICs and MND02 by the SPICE simulation. This result indicates that the flicker noise of the preamplifier in MND02 is 2 times lower than that of the first group ASICs because of the low noise operational amplifier (QOP) shown in Sec. 3.2.1. The open loop gain of QOP decreases at the frequency of more than 10 MHz shown in Fig. 3.7, which leads to the peak in the MND02 simulation result. This peak does not affect the noise calculation

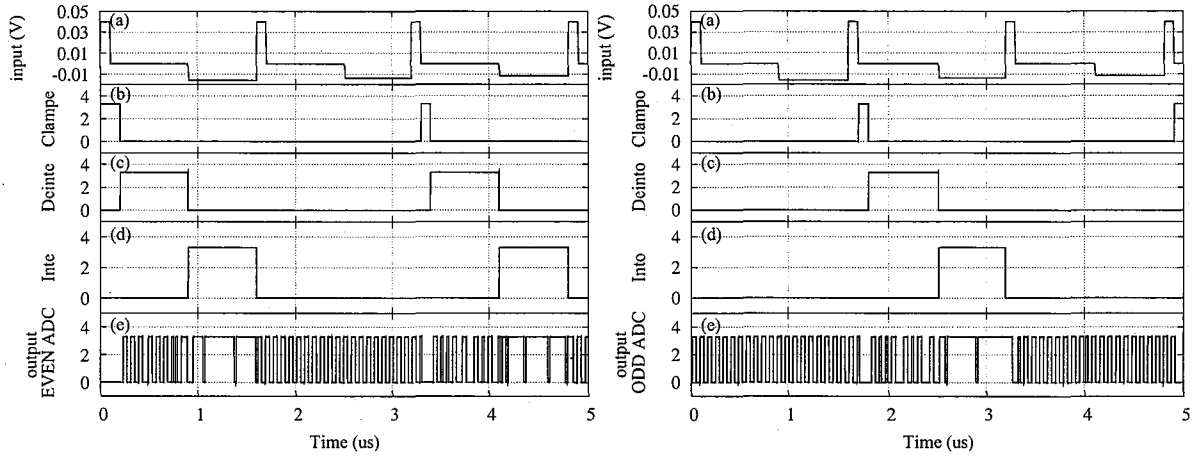


Figure 3.25: Simulation results of the chain. (a)~(e) are an input signal of the chain, Clamp, Deint, Int signals and bitstream (left : even ADC) and (right : odd ADC), respectively.

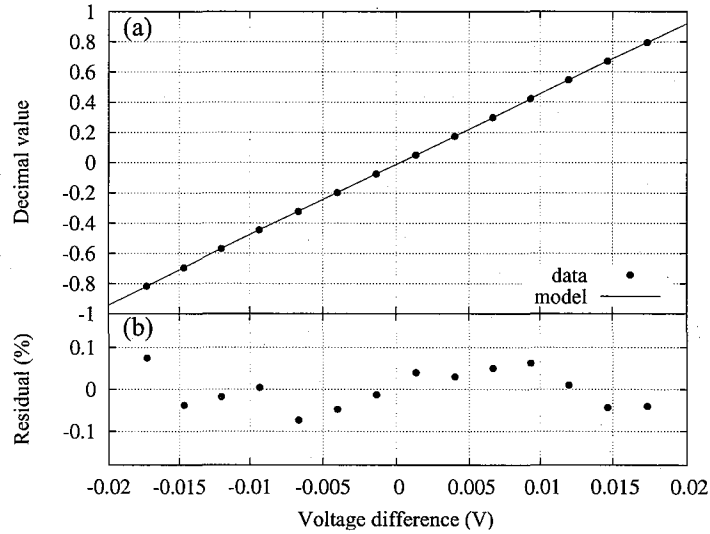


Figure 3.26: Linearity of the chain. The filled circle is simulation results and the solid line is the best fit model of the linear function in (a), and (b) shows the residual between the data and model.

because the noise at the frequency of less than 1 MHz is the dominant in the result.

The STF of the $\Delta\Sigma$ ADC can be considered as the multi-sampling method explained in Sec. 2.3.2

$$|H(f)_{\text{total}}|^2 = |H(f)_{\text{sample}}|^2 \times |H(f)_{\text{cds}}|^2 = \left(\frac{2 \sin(35\pi f T_{\text{clk}})}{35 \sin(\pi f T_{\text{clk}})} \sin(\pi f T_{\text{cds}}) \right)^2 \quad (3.28)$$

where 35 is the number of sample during Deint and Int phases, T_{cds} is the sample-to-

sample time for the correlation between the floating and signal levels ($T_{\text{cds}}=35 T_{\text{clk}}$). The equivalent input noise from the preamplifier is given as

$$N_{\text{preamp}} = \left(\int |H(f)_{\text{total}}|^2 \times |N(f)_{\text{input}}|^2 df \right)^{1/2} \quad (3.29)$$

where $N(f)_{\text{input}}$ is the (input)noise spectrum density of the preamplifier obtained by the simulation shown in Fig. 3.27.

Figure 3.28 shows the input noise of the preamplifier, the STF at the pixel rate = 19.5kHz given by eq.(3.28) and the calculation result of eq.(3.29). The noise at the frequency of ~ 10 kHz mainly contributes to the total noise from Fig. 3.28. The preamplifier noises of the first group and MND02 are estimated to $36 \mu\text{V}$ and $17 \mu\text{V}$ at the pixel rate of 19.5kHz, respectively. Figure 3.29 shows the expected noise from the preamplifier as a function of the pixel rate.

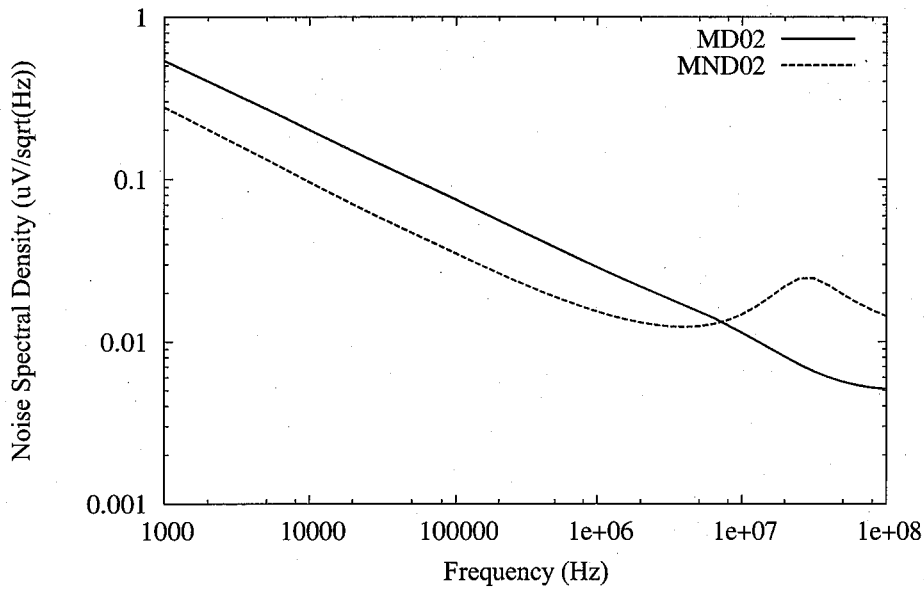


Figure 3.27: Noise simulation results of the preamplifiers in first group ASICs (solid line) and in MND02 (dashed line).

3.6 Interface

There are many digital signals for the 5-bit DAC setup, ASIC control and ADC outputs. We adapted the Low Voltage Difference Signaling (LVDS) level as the control signals and

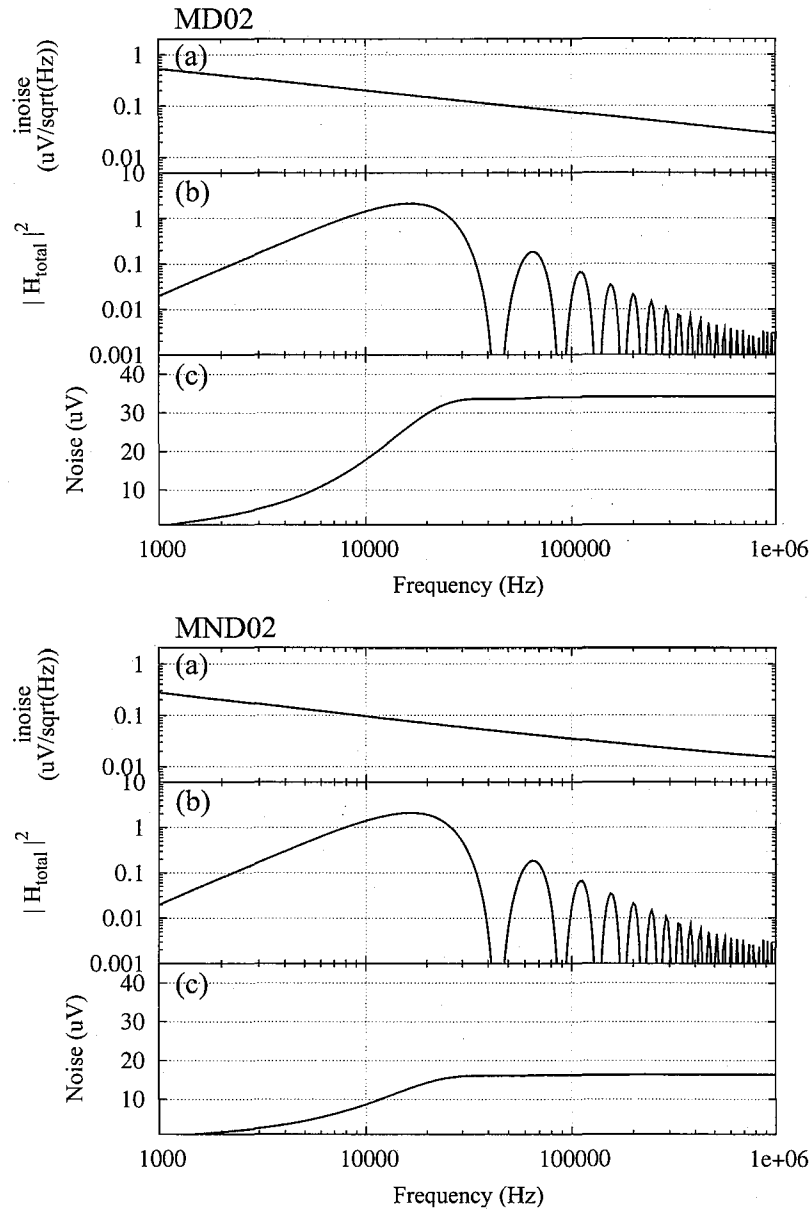


Figure 3.28: Noise calculation results of the preamplifiers in the first group ASICs (top) and MND02 (bottom). (a) is the input noise of the preamplifier obtained by the simulation shown in Fig 3.27, (b) is the STF of pixel rate = 19.5 kHz given by eq.(3.28) and (c) is the expected noise from the preamplifier given by eq.(3.29).

ADC outputs. The LVDS utilizes the current signal of 3.5 mA and voltage drop across the termination resistance of $100\ \Omega$. The LVDS reduces the effect of electro-magnetic radiation and effectively remove the common mode noise by the use of twisted-pair cable. A LVDS pair suppresses the digital-to-analog interface and improves data rate. The LVDS drivers and receivers are implemented in our ASICs.

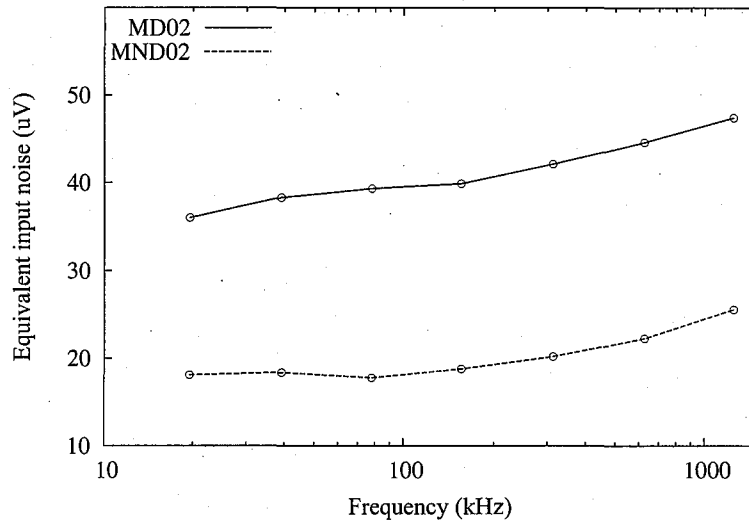


Figure 3.29: Calculated noise component from the preamplifier in MD02 (first group ASICs) and MND02 as a function of the pixel rate.

3.7 Development process of our ASICs

The development process of our ASICs is briefly summarized in the following itemization.

1. The determination of the ASIC specification that contains the required performance, fabrication process and development schedule.
2. The design of the circuit architecture. We utilized the software provided by gEDA project (gEDE web page), such as gschem, gnetlist and ngspice, and A division of Tanner Research, Inc. to draw the circuit layout and to run SPICE simulations.
3. We issued a request to Digian Technology, Inc. (Digian web page) for the design of the mask layout. It took about 6 weeks when the mask layout was completely new development.
4. The submission of the mask layout file to the agency of TSMC, MOSIS (MOSIS web page) or Cyber shuttle (Cyber Shuttle web page).
5. The ASIC fabrication in TSMC (TSMC web page) took about 2 months.
6. The assembly of bare chips by SUN-S Co., Ltd. (SUN-S web page) took about 2 weeks.
7. The evaluation test in our laboratory.

Chapter 4

Performance of ASICs

4.1 Evaluation test system

We first tested ASICs by using pseudo signals to study the basic function and the performance such as INL, equivalent input noise and power consumption before the readout test using X-ray CCDs. Figure 4.1 shows the photograph of the test board, and Fig. 4.2 illustrates the functional components of the evaluation test system. All the ASICs developed so far have the same pin configuration so that we can test them by using the same system. The test board mainly consists of a CCD simulator, first-in first-out memory (FIFO)(1), FIFO(2), clock divider and ASIC holder. These circuits on the test board are controlled by using NI6703 and NI6534 devices provided by National Instruments. These devices are operated by utilizing the device drivers developed by Comedi project (comedi web page) and LSE64 (LSE64 web page). NI6703 device has 16 analog outputs and 8 digital I/O lines. The analog output is variable between ± 10.1 V with the resolution of 16-bit. To generate the pseudo CCD signal, we prepare the 3 analog signals corresponding to the voltages of reset, floating and signal levels, respectively. The CCD simulator is composed of some analog switches and combines these analog signals, generating the CCD pseudo signal as shown in Fig. 4.3(a).

NI6534 device has 32 digital I/O lines. Its maximum speed of the data transmission is 20 MHz. This is not fast enough to continuously obtain the output data of the $\Delta\Sigma$ ADC when the pixel rate is faster than 250 kHz. We designed the non-real-time test system employing 2 FIFOs that memorized the control signals and output bitstreams, respectively. FIFO(1) receives the control signals, such as `Clamp`, `Int`, `Deint` and `Odd` signals, from NI6534 and provides them to the ASIC. The clock divider generates the sampling clock with the range from 1.5625 MHz to 100 MHz. The ASIC outputs, 160-bit data stream per pixel, are written into FIFO(2). Its memory size is 131072 bits \times 9 ports,

which corresponds to the data size of $819 \text{ pixels} \times 9 \text{ readout nodes}$. Since the ASICs do not have the decimation filter, the decimation process is performed by using software after data acquisition.

Figure 4.3 shows the signal waveforms obtained in this test. We can confirm both the basic function of the ASIC and the evaluation test system proper. We make the scatter plots and histograms from the filtered data of 819 pixels. The sample results of MD02 are shown in Fig. 4.4 and Fig. 4.5. The filtered values are shown as 12-bit equivalent in Chapter 4. We fit each histogram with a Gaussian function to measure the center value and noise.

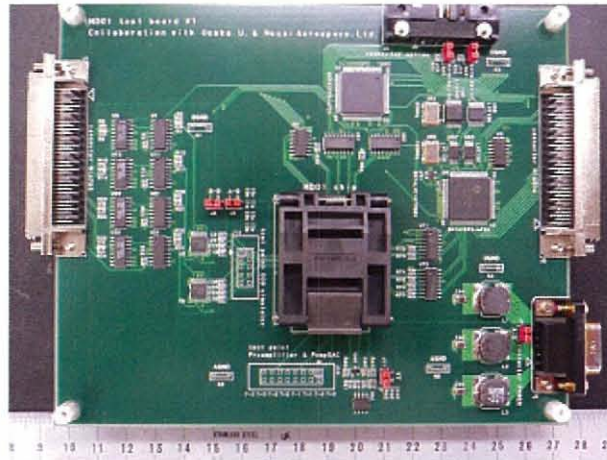


Figure 4.1: Photograph of the test board.

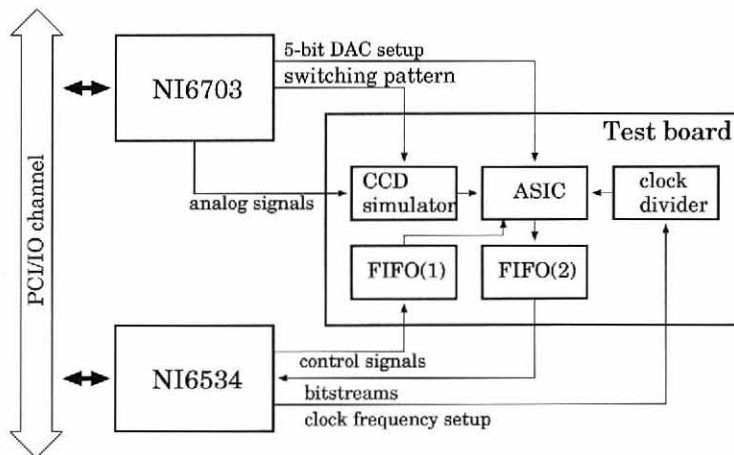


Figure 4.2: Block diagram of the evaluation test system using the CCD pseudo signals.

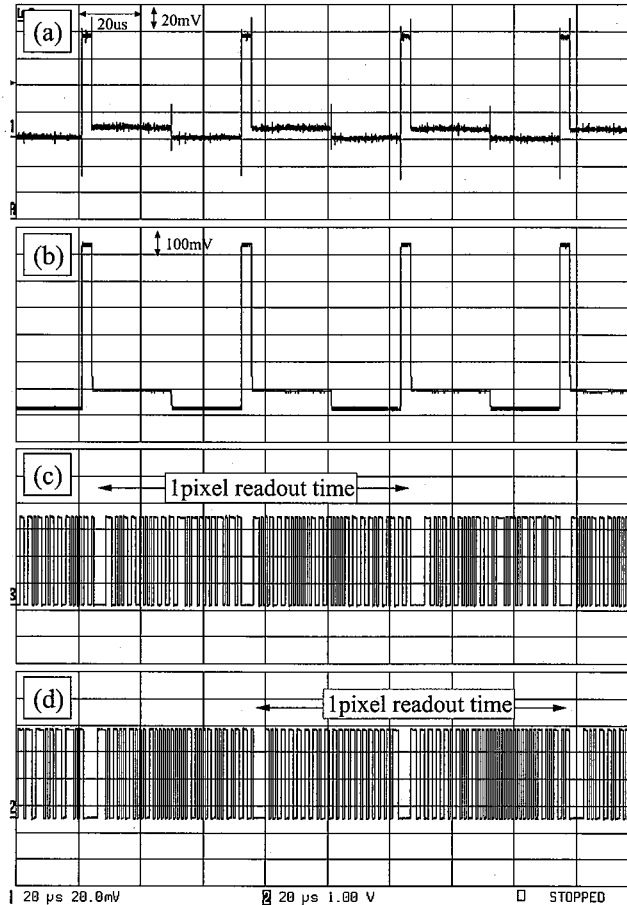


Figure 4.3: Signal waveforms obtained in this test. (a) is the CCD pseudo signal, (b) is the output of the preamplifier, (c) and (d) are bitstreams from the $\Delta\Sigma$ ADCs.

4.2 Integral Non-Linearity (INL)

In order to obtain the data of the various input voltages, we gradually changed the voltage of the signal level within the input range of the ASIC (± 20 mV). The voltage step of the DAC onboard NI6703, 16-bit DAC and output range of ± 10.1 V, is too large to measure the INL of our ASICs. We equipped an attenuator of 0.02 and could control the voltage between ± 20 mV with the accuracy of 13-bit. Figure 4.6 shows the linearity of one ADC output in MD01, MND01, MD02 and MND02. The INL distribution of all chips is shown in Sec. 4.7. Fig.4.6 (a) shows the decimal value and the model, a linear function and constant, as a function of input voltage difference between the floating and signal levels. Fig.4.6 (b) is the residual between the data and model.

The INL of MD01, MD02 and MND02 calculated by the best-fit method is 0.1~0.2% within the input voltage difference from -20 mV to 20 mV, which is comparable to the simulation result as shown in Sec. 3.5.1. Although the INL of MND01 is not good (0.7%),

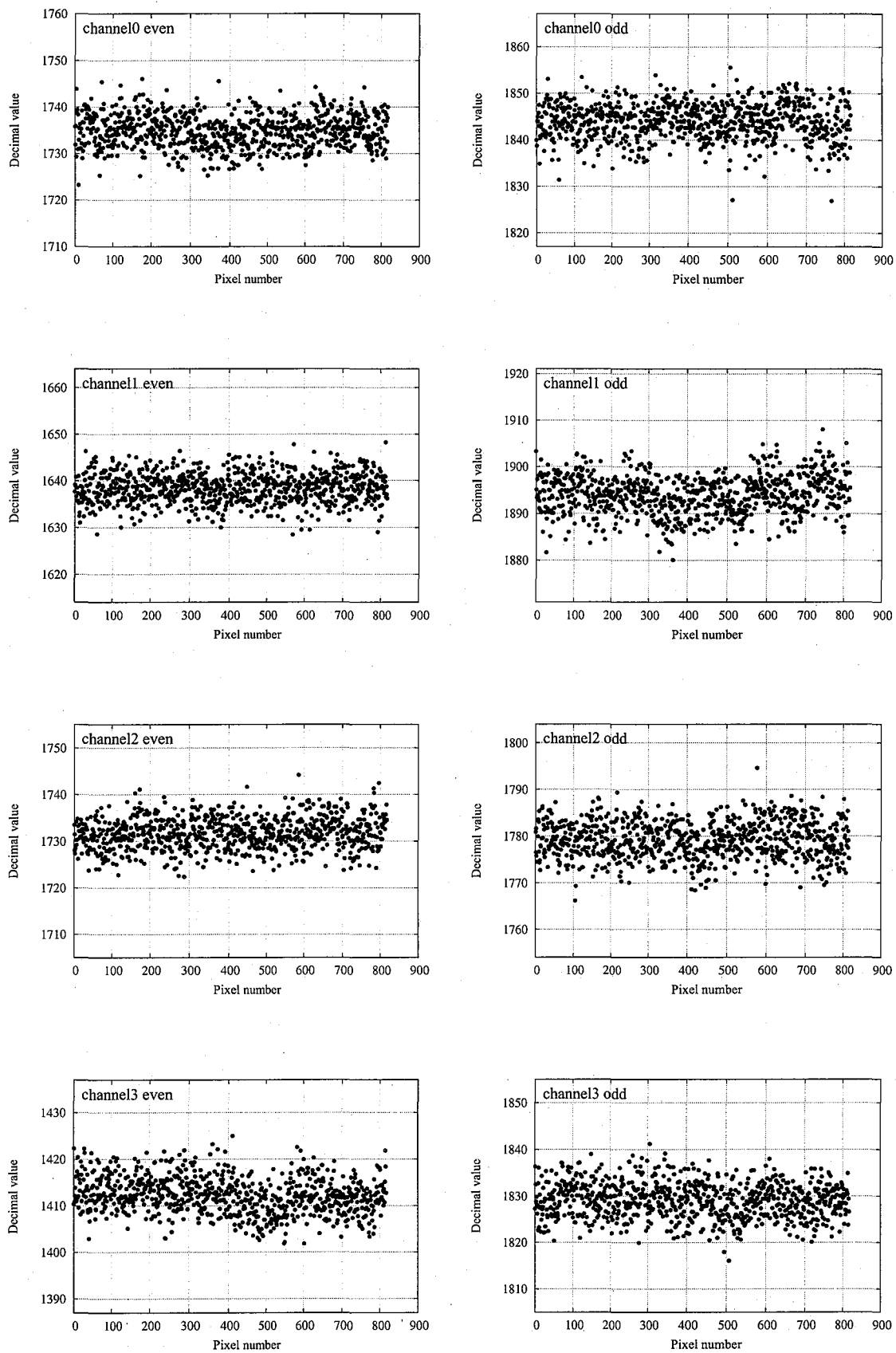


Figure 4.4: Scatter plots of the filtered ASIC outputs (MD02) at the pixel rate of 19.5 kHz.

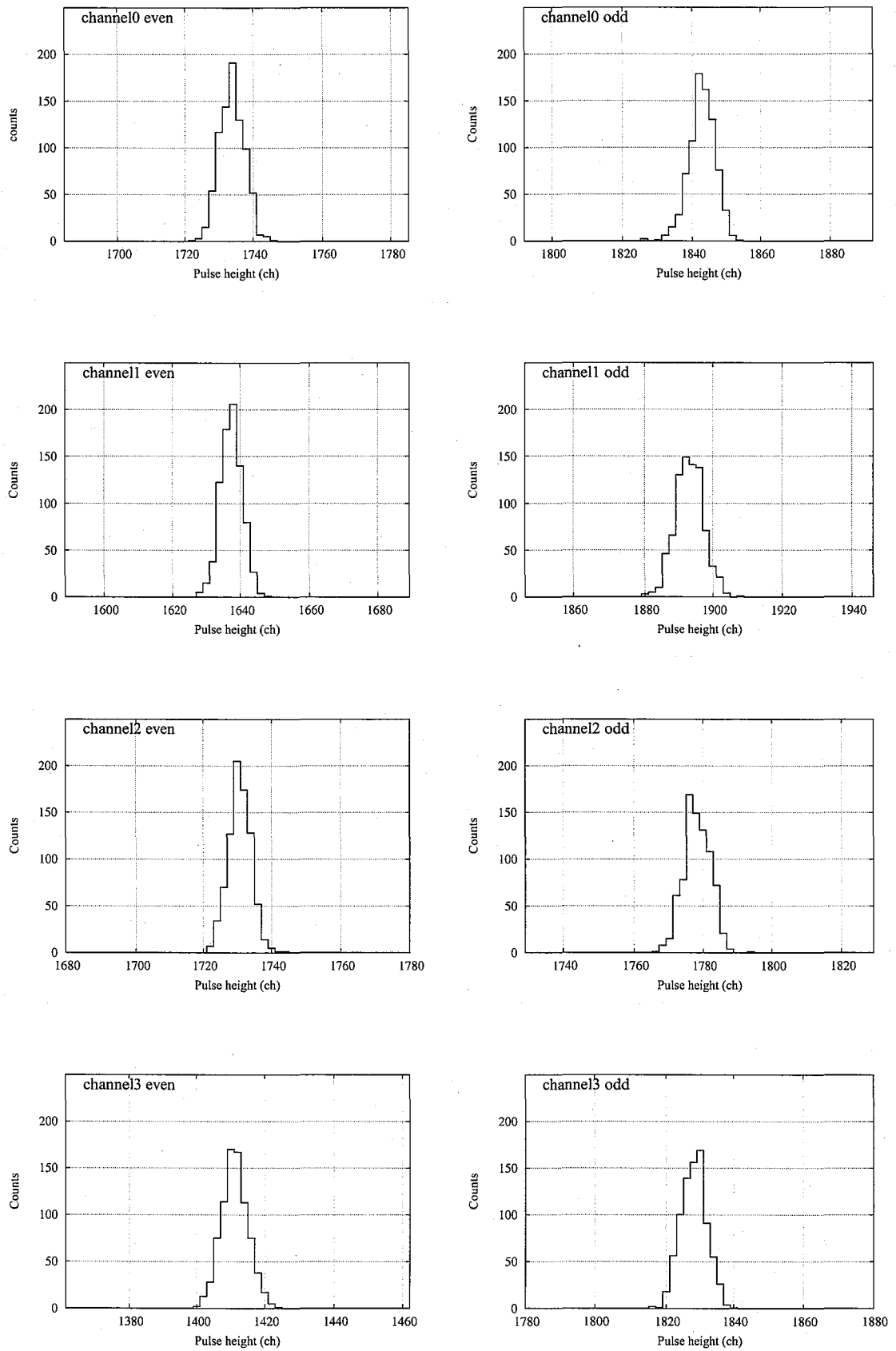


Figure 4.5: Histograms of the filtered ASIC outputs (MD02) at the pixel rate of 19.5 kHz.

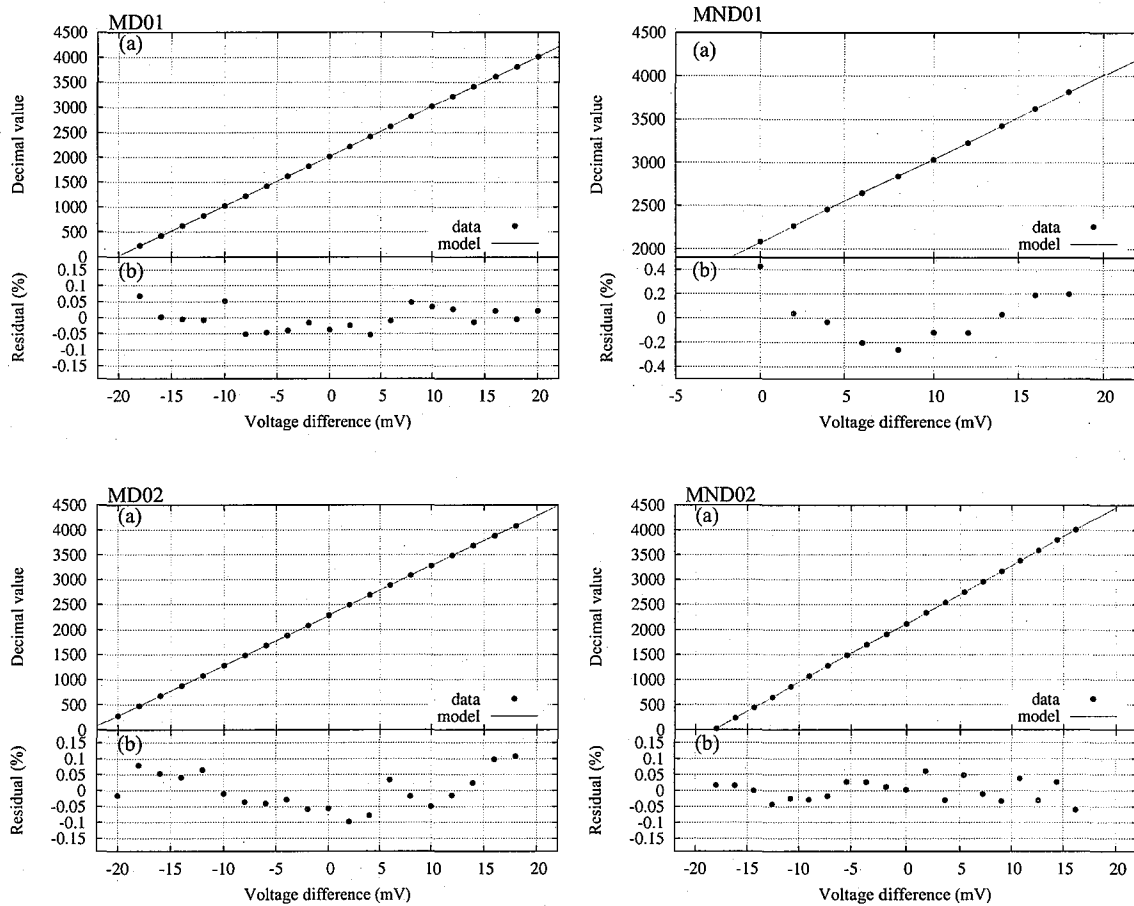


Figure 4.6: Linearity of one ADC output in MD01, MND01, MD02 and MND02. In the upper panel (a), the filled circle is the measured data and the solid line is the best fit model. The lower panel (b) shows the residual between the data and model. We should note that the residual of MND01 has different scale from others.

the residual of MND01 shown in Fig.4.6 (right top) is curved so predictable that we can compensate the degradation of INL by the calibration. Additionally, since we cannot obtain the proper data with the input voltage from -20 mV to 0 mV in MND01, its input range decreases by half compared with other ASICs. The reasons for the degraded INL and the decrease of the input range in MND01 are explained in Sec. 4.5. The input voltage range of 40 mV corresponds to ~ 30 keV for X-ray energy detected by the CCD when the gain of the preamplifier is 10 and the conversion factor is $5 \mu\text{V}/e^-$.

4.3 Noise performance

Figure.4.7 shows equivalent input noises from the ADC, preamplifier and the entire ASICs of MD01, MND01, MD02 and MND02 as a function of the pixel rate. Among these noises,

the noise from the preamplifier cannot be directly measured. We first obtain the noises from the ADC and the entire ASIC, and calculate the residual between these values as the preamplifier noise. The noise simulation results estimated in Sec. 3.5.2 are also shown in the figures of MD02 and MND02. The equivalent input noise of MD02 is $41.0 \pm 0.3 \mu\text{V}$, ADC = $20.5 \pm 0.2 \mu\text{V}$ and preamplifier = $35.5 \pm 0.5 \mu\text{V}$ at the pixel rate of 156 kHz. The preamplifier noise is dominant in the total noise of MD02 from the test results. The calculation value in Fig.4.7 agrees with the measured data. We succeeded in establishing the calculation method of the preamplifier noise.

We considered the flicker noise from the preamplifier as the main noise source in MD02 as shown in Fig. 3.28. We implemented the low noise operational amplifier in MND02 to suppress the flicker noise of the preamplifier. The calculated noise from the preamplifier in MND02 is $19 \mu\text{V}$ at the pixel rate of 156 kHz, which is about half that in MD02. The measured noise of MND02 is $29.4 \pm 0.3 \mu\text{V}$, ADC = $18.7 \pm 0.2 \mu\text{V}$ and preamplifier = $22.3 \pm 0.5 \mu\text{V}$ at the pixel rate of 156 kHz. We decreased the preamplifier noise by 40% as the calculation results. The noise distribution of all chips is shown in Sec. 4.7. The ADC noise has a tendency to rapidly increase at the pixel rate of more than 312 kHz. We are currently studying the source of this result. We will evaluate the frequency characteristic of the bitstreams by Discrete Fourier Transform (DFT), and change the decimation filter coefficient.

An Equivalent Noise Charge (ENC) depends on a conversion factor in the readout test using CCDs. The ENC can be described as

$$\text{ENC} = \frac{\text{Equivalent input noise } (\mu\text{V})}{\text{Conversion factor } (\mu\text{V}/e^-)} \quad (4.1)$$

Assuming the conversion factor of $5 \mu\text{V}/e^-$, the ENCs of MD02 and MND02 are expected to be about 7 and 5 electrons, respectively. The ratio of the ASIC noise to the total system noise decreases with increasing the conversion factor.

4.4 Power consumption

Figure 4.8 shows the power consumption per chip as a function of the pixel rate. The power consumption of MND01 and MD02 is about 90 mW/chip at the 156 kHz pixel rate. Note that the power of MD01 at the high pixel rate of more than ~ 200 kHz does not change due to the malfunction of the digital circuits as explained in § 4.5. The difference of the power consumption between MND02 and other chips is caused by the current of LVDS drive. The signal current and termination resistance in the normal LVDS level are 3.5 mA and 100Ω , respectively. In MD01, MND01 and MD02, we changed the signal current

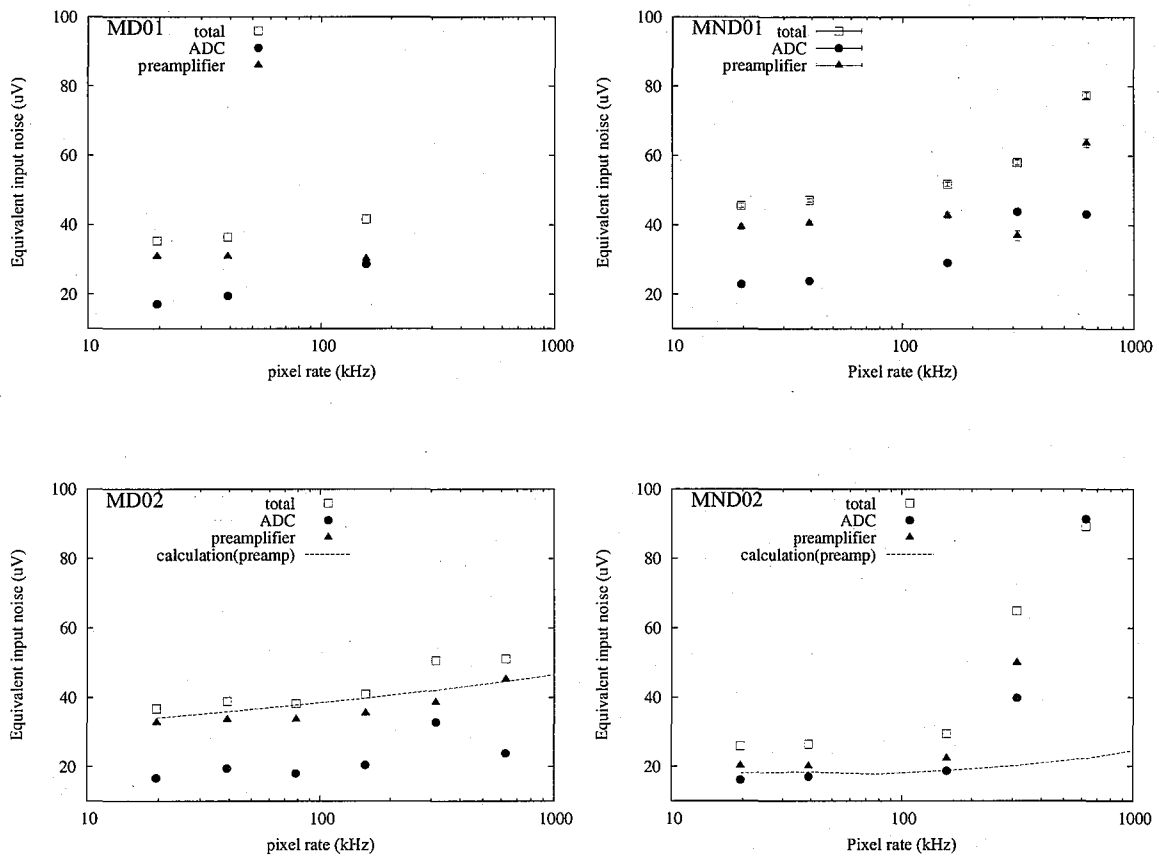


Figure 4.7: Equivalent input noises of the ADC, preamplifier and ASIC total as a function of the pixel rate.

to $350 \mu\text{A}$ and the resistance value to $1 \text{ k}\Omega$ in order to decrease the power consumption. While, we implemented the LVDS drivers with the standard level in MND02. Since there are 8 LVDS drivers in our ASICs, the expected increment of the power is $3 \text{ mA} \times 3.3 \text{ V} \times 8 = 79.2 \text{ mW}$ that explains the test results.

4.5 Highest pixel rate

We are developing an ASIC that can process a CCD signal at the pixel rate of up to 1 MHz, which is about 10 times faster than that of an ordinary system. We expect that we can apply our ASICs not only to X-ray fields but also optical applications.

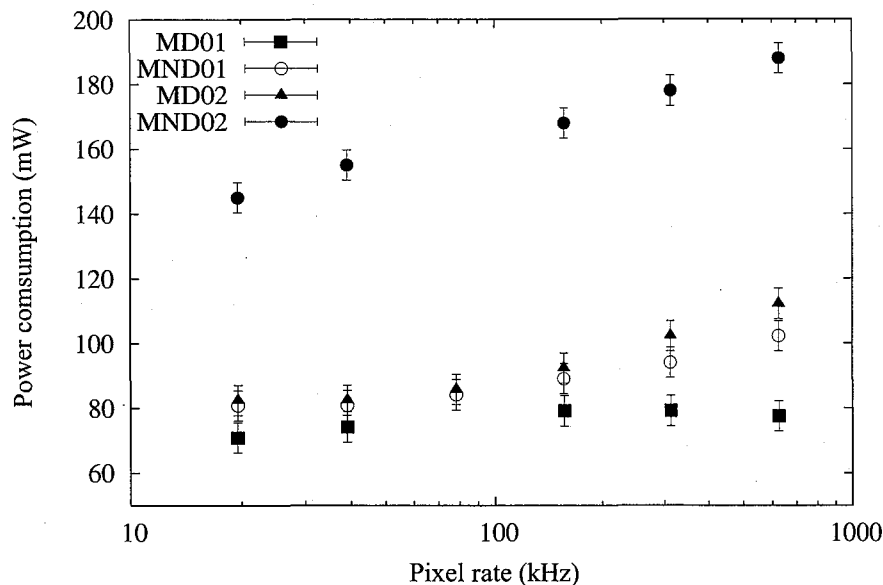


Figure 4.8: Power consumption of ASICs per chip as a function of the pixel rate.

Problem in MD01

We find that the highest pixel rate of MD01 is 155 kHz (sample rate = 12.5 MHz) as shown in Figs. 4.7 and 4.8, nevertheless there is no problem up to the pixel rate of 1 MHz in the simulation. We assumed that the malfunction of MD01 at the high pixel rate was caused by the n-channel MOS FET without a N-channel Lightly Doped Drain (NLDD) region. A MOS FET generally has a LDD region between a channel and source or drain regions. A LDD region prevents the high electrical field which leads the degradation of the FET function and break down. In the fabrication through the MOSIS service, if the NLDD layout data do not exist in the submission file, that is automatically derived from the thick oxide, n-well and n-channel plus select layers as detailed in (MOSIS web page). When the submission file contains its layout data, the NLDD region that is designed in the file is only produced. Since the layout file of MD01 contained the NLDD data only in the analog area, the NMOS in the digital circuit did not have the NLDD region. We learnt it was impossible to verify this effect by the currently available simulation program. We developed MND01 and confirmed that the ASIC properly functioned at the high pixel rate of up to 625 kHz (sample rate = 50 MHz).

Figure 4.9 shows the rise and fall times of Dout signal from 5-bit DAC in MD01 (top) and in MND01 (bottom). We measured these values by the oscilloscope with the capacitance of the probe = 12 pF. In the simulation results, the rise and fall times are 18 ns and

10 ns, respectively. The measured rise time of MD01 is almost equal to that of MND01 and simulation result. However, the measured fall time of MD01 is significantly slower than that of MND01. The fall time exhibits the property of NMOS in the digital circuits. These results directly indicate that the NMOS in MD01 has the problem.

MD01 had another problem that was the malfunction of the LVDS drivers. We thought that this problem also related to the NLDD region. Figure 4.10 shows the output signals of the LVDS driver in MD01 (top) and these in MND01 (bottom). The output current of the LVDS driver is $350\ \mu\text{A}$, which is 10 times lower than that of the standard LVDS level. Since we set the termination resistance to the standard LVDS resistance of $1\ \text{k}\Omega$, the voltage swing is equal to the standard LVDS level. We can see the proper differential signals with the voltage swing of about 350 mV in Fig. 4.10 (bottom), whereas the signals of MD01 shown in Fig. 4.10 (top) are far from the expected voltage difference between the signals ($350\ \mu\text{A} \times 2\ \text{k}\Omega = 700\ \text{mV}$). This is the malfunction of the LVDS driver in MD01.

Problem in MND01

MND01 had raised independent problems from those of MD01 such as the decrease of the dynamic range and the degradation of the INL and noise level. Figure 4.11 shows the scatter plots of channel-2 in MND01 as the input voltage differences are $-20\ \text{mV}$ and $18\ \text{mV}$. There are several gaps in the scatter plots when the input voltage difference is less than 0 V as shown in Fig. 4.11 (top). These gaps transiently appear and disappear in several readout channels. Since we cannot obtain the correct values within the input voltage from $-20\ \text{mV}$ to 0 V, the input range decreases by half compared with that of MD01. The even and odd outputs exhibit the different behavior with each other as shown in Fig. 4.11. We thought that these gaps were caused by the $\Delta\Sigma$ ADCs. However, the ADC in MND01 is the same circuit architecture as that of MD01.

We assumed that these problems were caused by the difference between the MOSIS service and the Cyber shuttle service. We recently found that there was the difference in the definition of a ElectroStatic Discharge (ESD) layer between two services. We issued a request to Digian Technology, Inc. for the design of the mask layout as shown in Sec. 3.7. They set a layout number of ESD layer to 30 in Graphic Data System (GDS) format. In the MOSIS service, a layer number of 5 V ESD is 36 in GDS format, and the layer of 30 is ignored as shown in (MOSIS web page). Therefore, the ESD layer is not implemented in the products by the MOSIS service, such as MD01, MD02 and MND02. In the Cyber shuttle service, the layer number of 5 V ESD is 36 and a layer number of 3 V ESD is 30 in GDS format. The 3 V ESD layer is implemented in the product of the

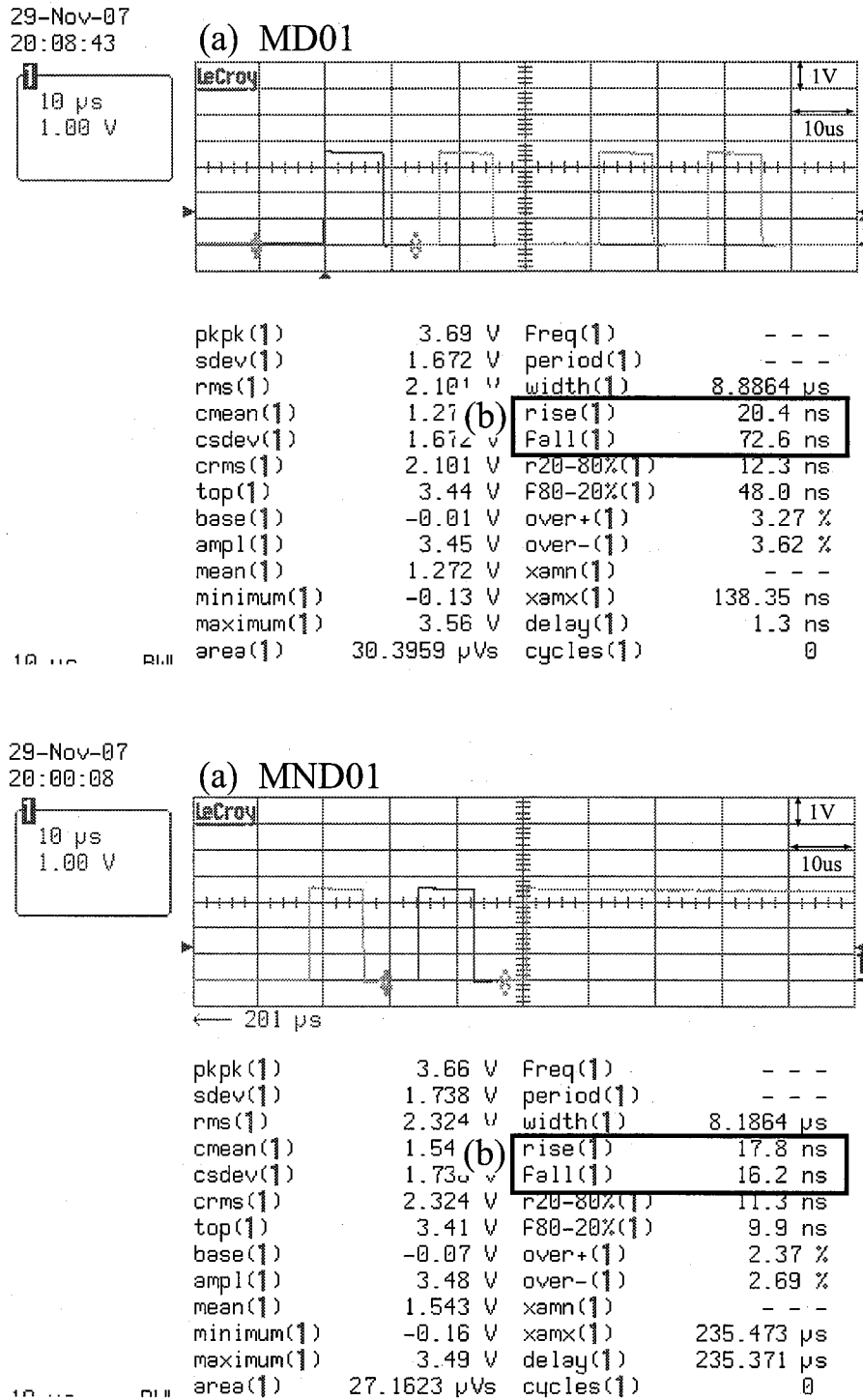


Figure 4.9: Rise and fall times of Dout signals in MD01 (top) and in MND01 (bottom). (a) is the signal waveforms and (b) shows the results measured by the oscilloscope with the capacitance of the probe = 12 pF.

Cyber shuttle service, MND01. To investigate the effect from this difference, we fabricated MD02 whose circuits were the identical to that of MD01 except for the NLDD layer by

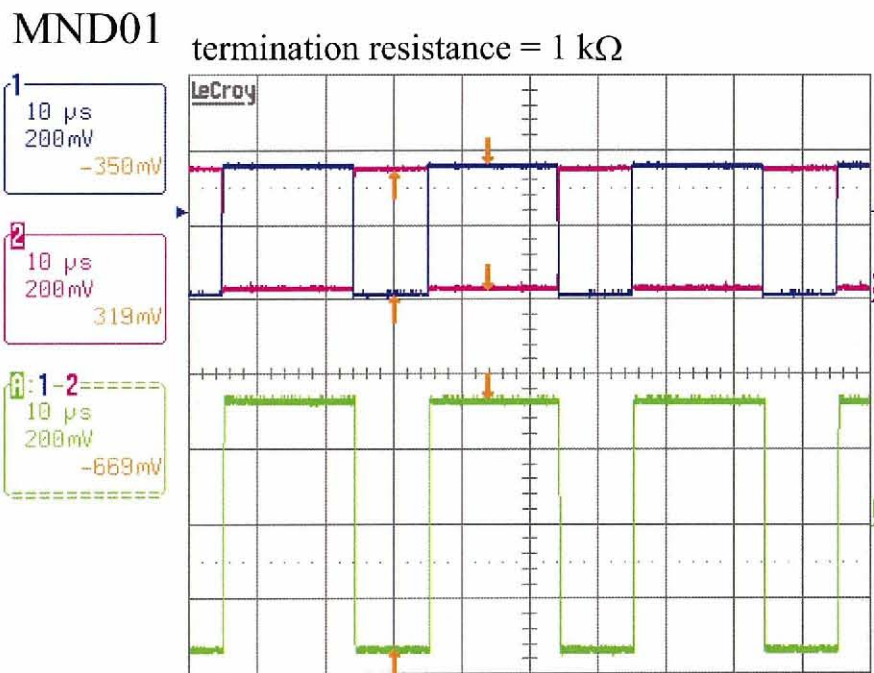
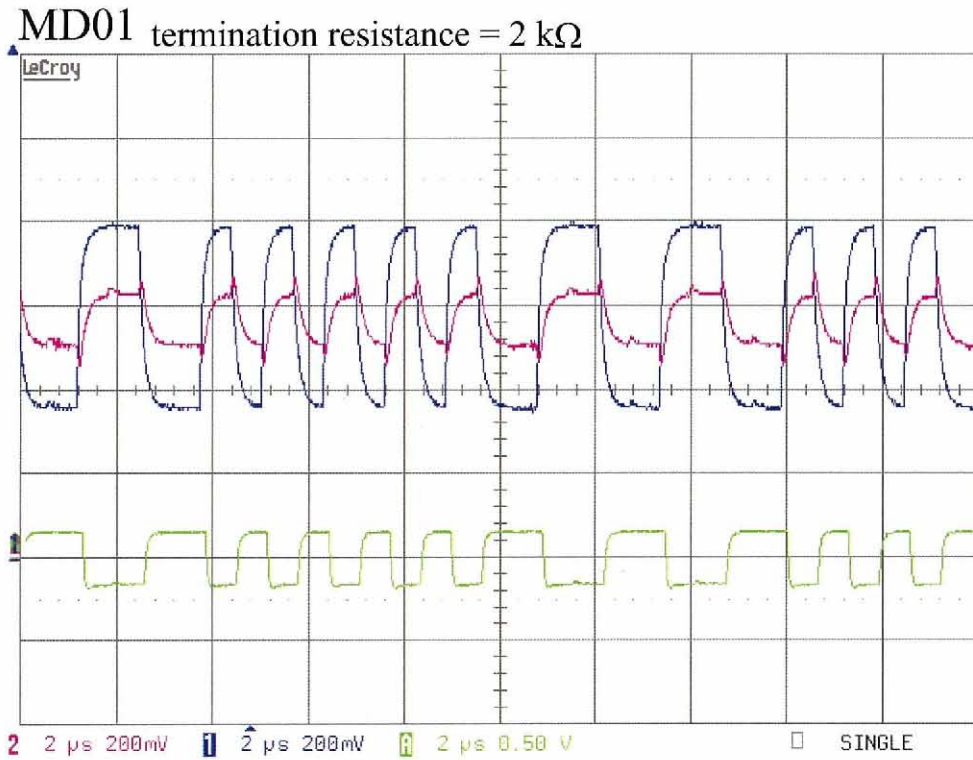


Figure 4.10: Output signals of the LVDS drivers in MD01 (top) and in MND01 (bottom). Red and blue show the voltages across the termination resistance, and green is the voltage difference between red and blue.

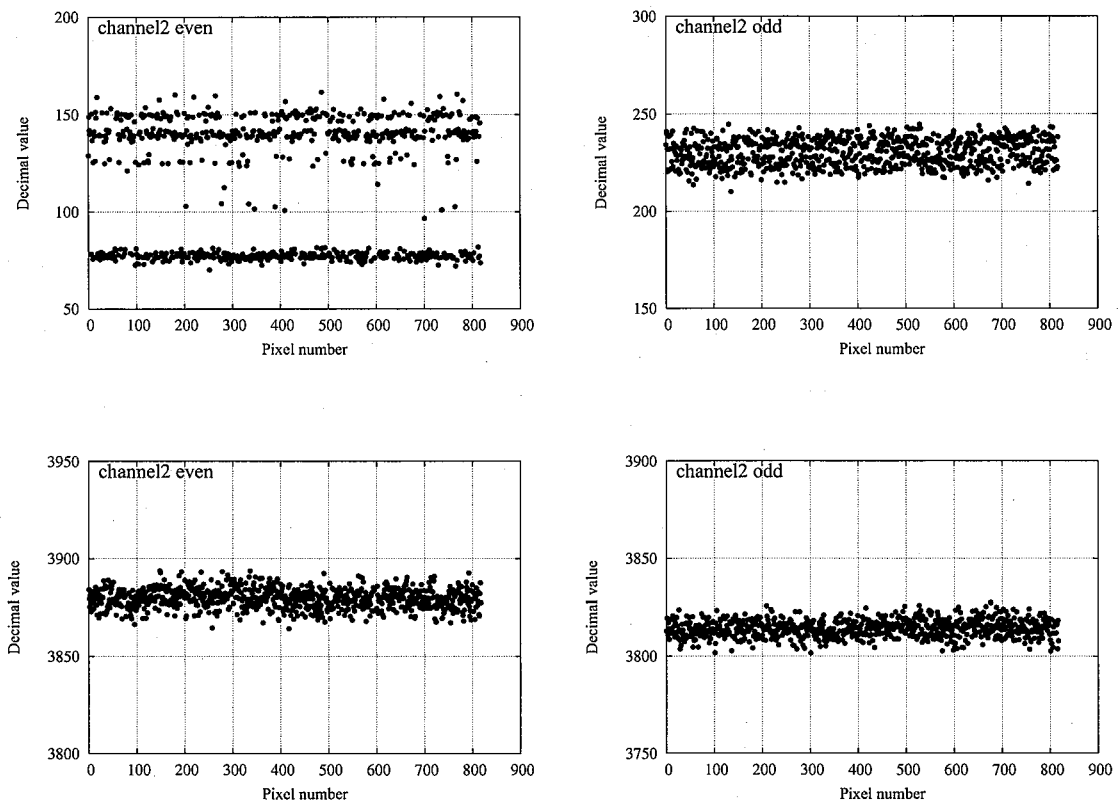


Figure 4.11: Scatter plots of channel-2 in MND01 when the input voltage differences are -20 mV (top) and 18 mV (bottom), respectively.

the MOSIS service. Through the test results as shown above, MD02 has the similar noise performance to that of MD01 and the similar maximum speed to that of MND01.

4.6 Radiation test

4.6.1 Motivation

The motivation of the radiation test is to study total ionization dose (TID) effects of our ASICs and verify that they can be employed as the front-end electronics onboard the satellites. We are now designing the X-ray CCD camera system using our ASICs for the SXI onboard ASTRO-H. The orbit of ASTRO-H will be the low earth orbit of 550 km similar to those of ASCA (Tanaka et al. 1994) and Suzaku (Mitsuda et al. 2007). The radiation damage mainly occurs by the high-energy protons during passing through the South Atlantic Anomaly (SAA). The estimated TID per year for the CCDs onboard ASCA satellite is ~ 0.2 krad (Yamashita et al. 1999). The CCDs are surrounded by the shields with the average thickness of 11 g cm^{-2} aluminum (Al) equivalent to protect them from protons and suppress the background level recorded by the CCDs. Since the readout system is placed outside of the thick shield, the total absorption dose of the readout system is generally estimated to ~ 1 krad per year in this orbit. The typical lifetime of the satellite is 5 years. The required radiation tolerance for our ASICs is more than 5 krad.

4.6.2 Test condition

We tested the radiation tolerance of MD01 using the accelerator proton beam from the medium-energy accelerator in the Heavy Ion Medical Accelerator in Chiba (HIMAC) at the National Institute of Radiological Science in Japan. The proton energy is 200 MeV and the beam size is $1 \text{ cm} \times 1 \text{ cm}$. We adjusted the position of the beam center by using a laser pointer and a phosphorplate. We measured the intensity of the proton beam by using a scintillation counter. The average of the beam count rate is variable from $10^2 \sim 10^8$ protons per second with accuracy of 20% (Nakajima, H. et al. 2008). We obtained the test data by 5 minutes to measure any degradations of the performance such as the noise, linearity and gain. The bias voltage was supplied to the ASIC, and the consumption current was monitored during the radiation test. Figure 4.12 shows the TID as a function of the radiation time. We increased the intensity of the proton beam by a factor of 10 after the radiation time of 2 hours. The ASIC used in the radiation test was annealed at the room temperature for 3 months. We measured the ASIC performance after the annealing and compared the results with those during the radiation test.

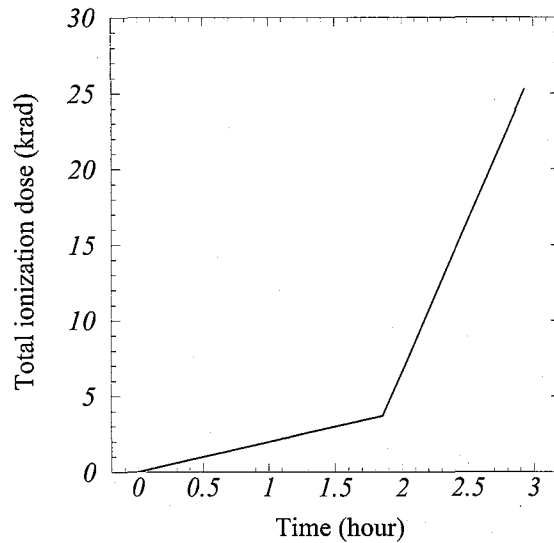


Figure 4.12: TID as a function of the radiation time.

4.6.3 Test results

The consumption current of MD01 was stable within the accuracy of 1 mA that is the current accuracy during the radiation test as shown in Fig. 4.13. These results indicate that the latch-up did not occur. Note that the results in Fig. 4.13 include the current of the ASIC as well as surrounding circuits on the test board. Figure 4.14 shows the decimal value as a function of input voltage at the total absorption dose of 0, 22 and 25 krad. The gains of all channels are reduced as the amount of the absorption dose increases. The relative gain of each channel is shown in Fig. 4.15. If the modulator has been damaged by the radiation effect, the gain change is not synchronized with each ADC output as shown in Fig. 4.15. Figure 4.16, additionally, shows the scatter plots of channel-0 and channel-1 at the absorption dose of 22 krad. We can see the jumps in the plots of channel-1 odd and even outputs at the same timing. Although we did not monitor the output of the preamplifier during the radiation test and could not directly study their output signals, the test results indicated that the preamplifier lost its function by the radiation damage.

Fig. 4.17 shows the relative standard deviation of the histogram obtained as a function of the TID and the ADC noise level of MD01. They are stable up to the total dose of ~ 17 krad. However, there are the peaks at 20 krad and the values asymptotically approach to the ADC noise. The effective mobility of electrons is higher than that of holes. When protons generated electrons and holes in the oxide layer, the electrons effectively escape from the oxide layer by the electric field in this layer. In this way, it is holes that are

trapped in the oxide layer. The trapped holes charge the oxide layer positively, which leads to the negative threshold voltage shift of MOS FETs and the degradation of $1/f$ noise (Yokoyama, M. et al. 2001, Matsushita, T. et al. 1995). The noise increase around 17krad in Fig. 4.17 can be explained by the effect of the trapped holes. We supposed the function of the preamplifier gradually degraded and was lost after 20krad as shown in Fig. 4.14. Since the preamplifier did not function, the noise from the preamplifier was removed and the entire ASIC noise approached to the ADC noise.

We investigated the effect of the negative threshold voltage shift of MOS FETs by the SPICE simulation. Figure 4.18 shows the simulation results with the voltage shift = 0 V (normal condition) and -0.6 V. The output of the operational amplifier (OP) with the voltage shift = 0.6 V is not different from that of the normal condition except for the DC voltage level. The inverter after OP dose not function. Through these results, the preamplifier malfunctioned in the voltage shift of 0.6 V. However, this inverter is used in the several circuit blocks such as 5-bit DAC and $\Delta\Sigma$ ADC. Since we think the ADC properly functions, there is a discrepancy between the test results and the simulation. We cannot figure out the source of these results from the current data, and will study about this problem in the next radiation test. The data list that we need to obtain in the next test are summarized below.

1. Monitor of the preamplifier output : We can directory investigate the total dose effects of the preamplifier.
2. Data using 5-bit DAC : We did not operate 5-bit DAC in this test. If the preamplifier malfunctions, we can distinguish which has the problem, the operational amplifier or the inverter, by the data using 5-bit DAC. The signal of 5-bit DAC is only amplified by the inverter as shown in Sec. 3.2. If the preamplifier only outputs the 5-bit DAC signal, the operational amplifier must be damaged.
3. Bitstreams : We should obtain not only filtered ASIC outputs but also bitstreams. We can study the operation of the $\Delta\Sigma$ ADC during the radiation test from the patters of the bitstreams.

In Figs. 4.14(b) and 4.17(b), we show the test results of MD01 after annealing at the room temperature for three months. Since the trapped holes are discharged by the tunneling effect during the annealing, we find that the ASIC performance is fully recovered. We concluded that the ASIC tentatively malfunctions due to high flux of protons. We think that the radiation tolerance of our ASIC is higher than 17krad under the practical proton beam. Figure 4.19 shows the simulation result of the TID in the low earth orbit

from 1 January 2012 to 1 January 2016 as a function of the thickness of Al shield. The integrated fluence of proton and electron defined in this simulation is shown in Fig. 4.20. The horizontal axis is the lower limit of proton and electron energy, and the vertical axis is the integrated fluence of them with energy of more than the lower limit. Figure 4.19 indicates that our ASICs covered by Al with thickness of several times of hundred μm can meet the radiation tolerance required for ASTRO-H.

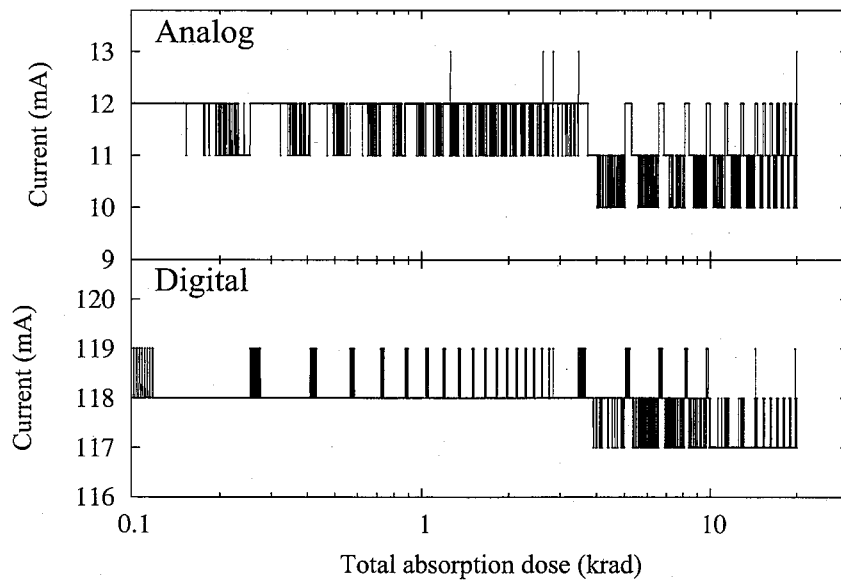


Figure 4.13: Monitors of analog and digital currents during the radiation test.

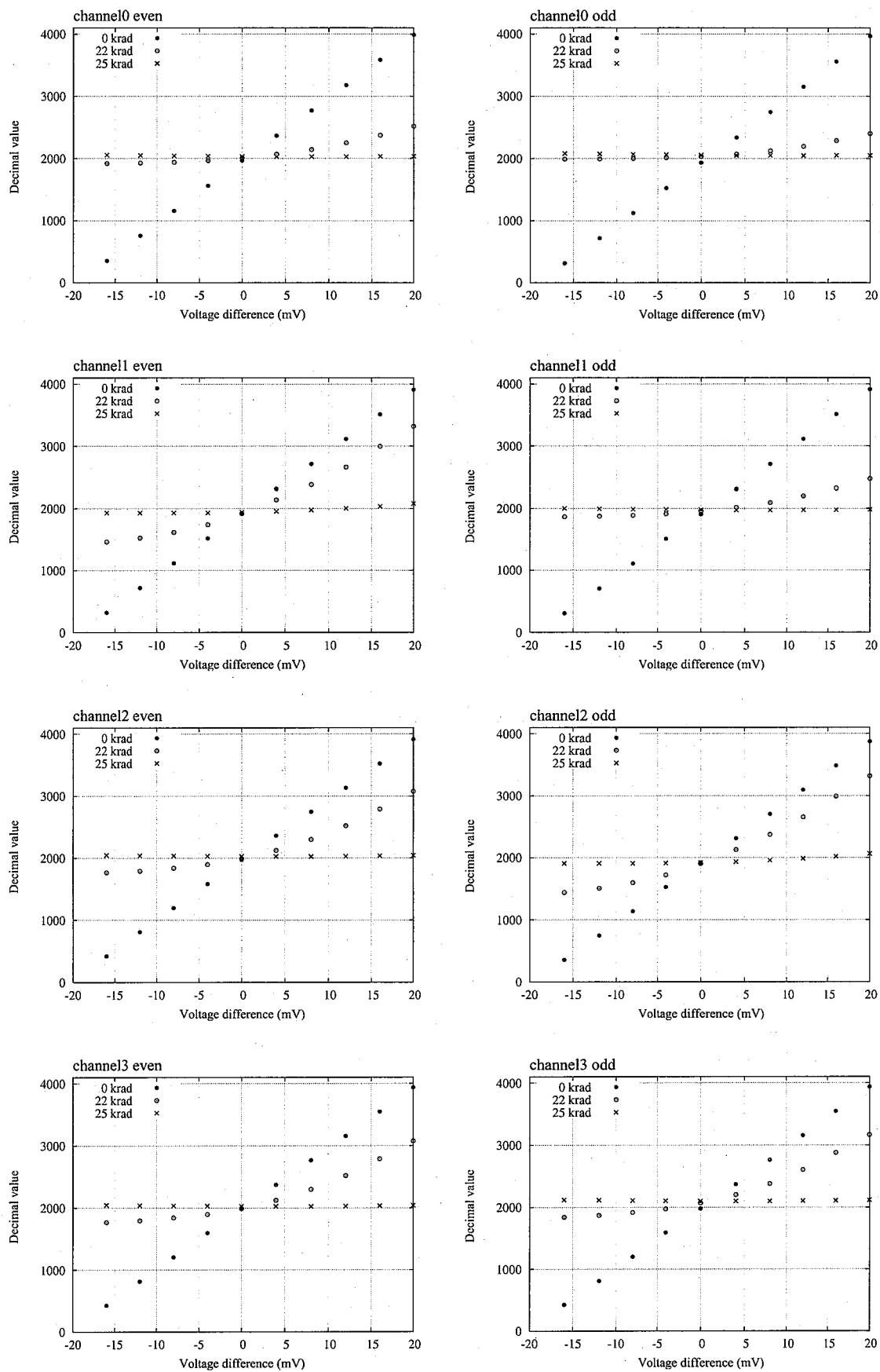


Figure 4.14: Linearity of each ADC output at the TID of 0, 22 and 25 krad.

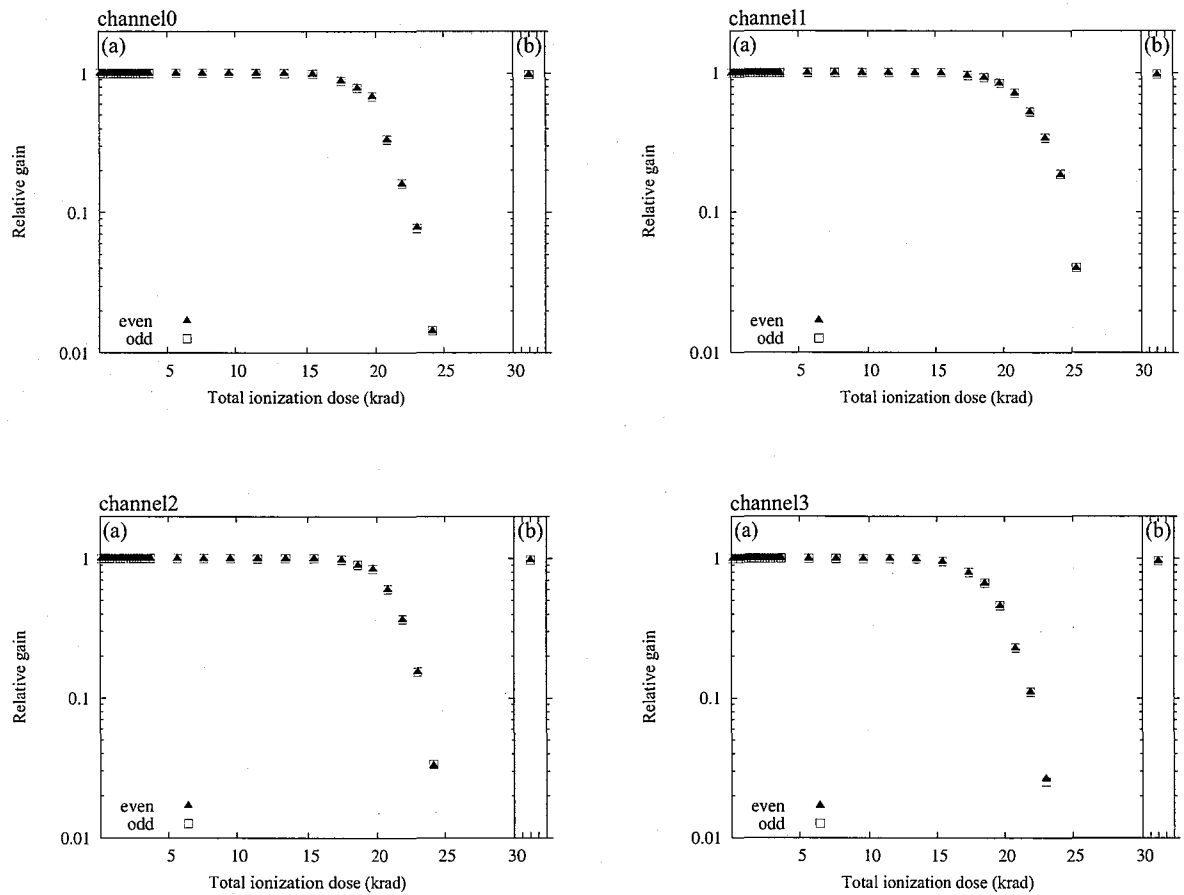


Figure 4.15: Relative gain of each readout channel in MD01 as a function of the TID. (a) is the results during the proton beam irradiation and (b) is the result after the annealing of 3 months.

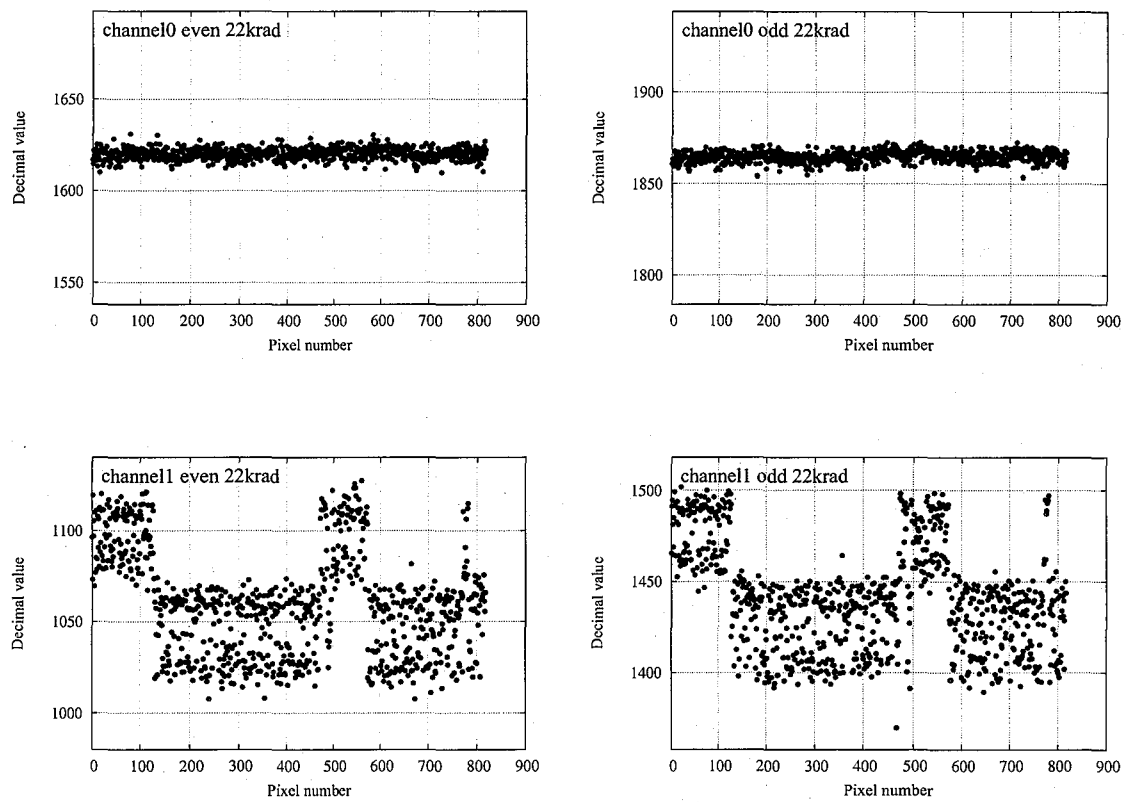


Figure 4.16: Scatter plots of channel-0 and channel-1 at the TID of 22 krad.

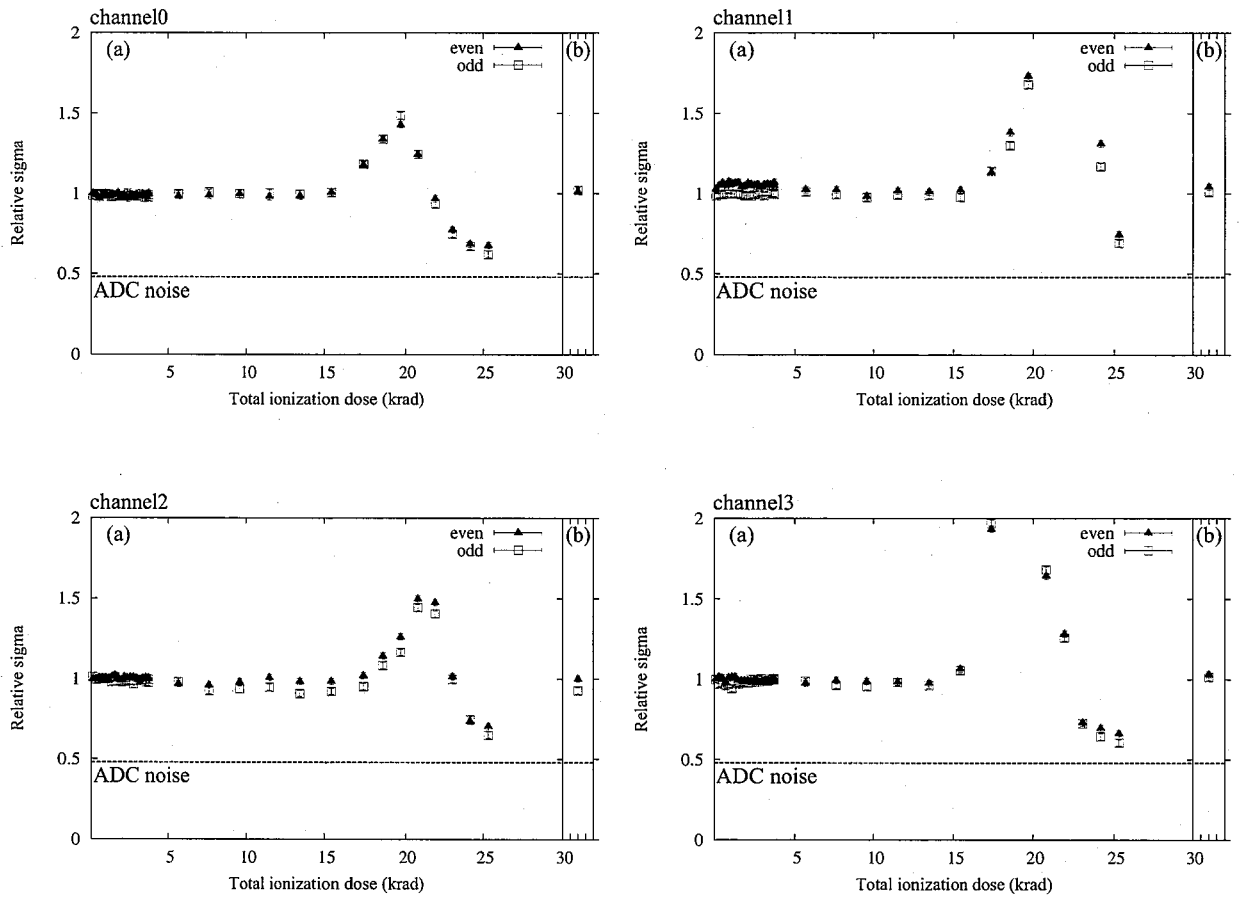


Figure 4.17: Relative sigma of histograms for each readout channel in MD01 as a function of the TID. (a) is the results during the proton beam irradiation and (b) is the result after the annealing of 3 months.

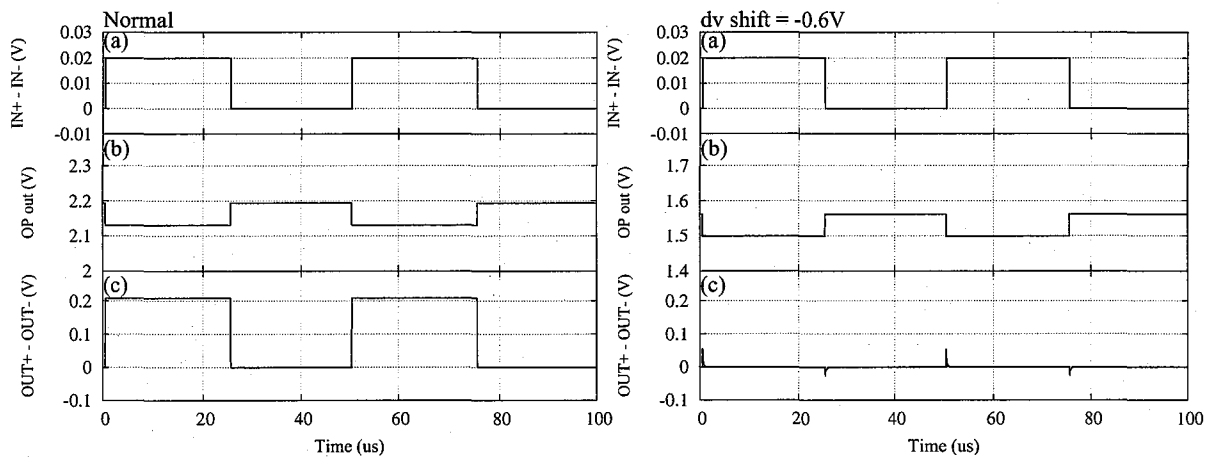


Figure 4.18: Simulation results of the preamplifier as the threshold voltage shift = 0 V (left) and 0.6 V (right). (a) is an input signal ($IN_+ - IN_-$), (b) is an output of OP and (c) is an output of the preamplifier ($OUT_+ - OUT_-$) as shown in Fig 3.4.

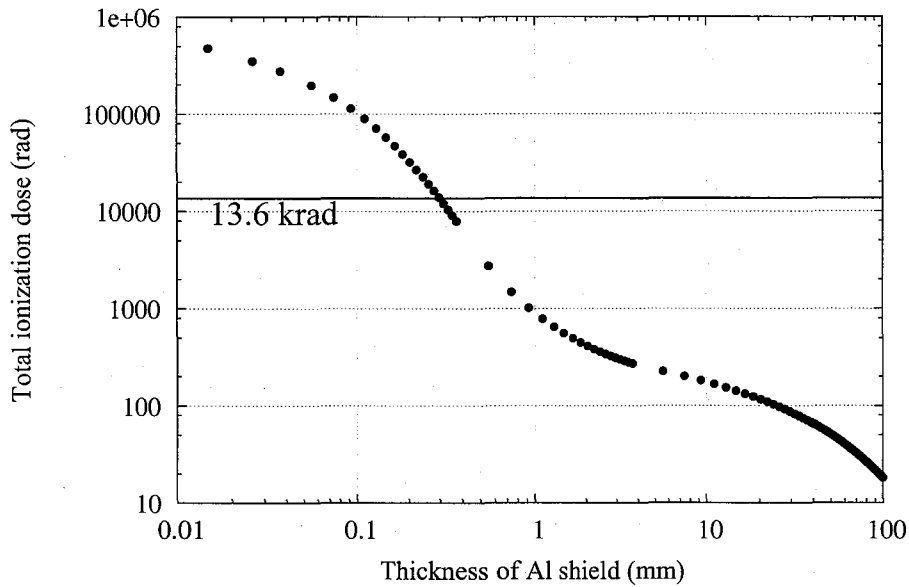


Figure 4.19: Simulation result of the TID (4 years) as a function of a thickness of Al shield in the low earth orbit. The solid line shows the TID of 13.6 krad ($17 \text{ krad} \times \frac{4}{5}$).

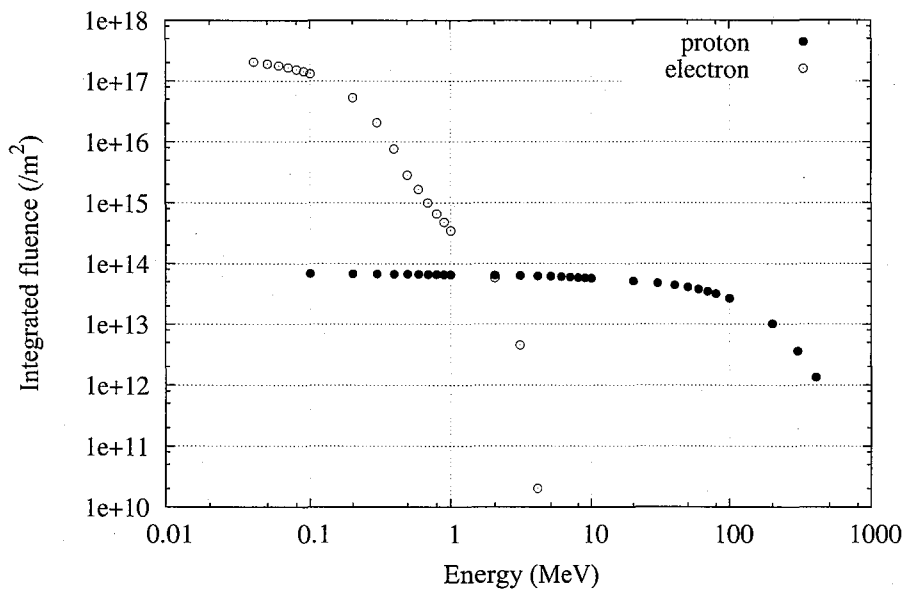


Figure 4.20: Integrated fluence of proton and electron defined in the simulation (Fig. 4.19). The horizontal axis is the lower limit of proton and electron energy, and the vertical axis is the integrated fluence of them with energy of more than the lower limit.

4.7 Test summary

The evaluation test results of each ASIC are summarized in table 4.1. We only showed the test results of one ADC output or one chip in this chapter. The distributions of the noise, INL and gain ($\frac{\text{Decimal value}}{\text{Input voltage difference}}$) of all chips and outputs are shown in Fig. 4.21, 4.22 and 4.23. Their average and standard deviation are given in Table 4.2.

Table 4.1: Performance summary of ASICs.

	MD01	MND01	MD02	MND02
Production service	MOSIS	Cyber shuttle	MOSIS	MOSIS
Power consumption/chip (mW) ¹	79	89	92	168
Maximum pixel rate (kHz)	156	625	625	625
INL (%)	0.2	1.2	0.2	0.2
Input range (mV)	40	20 ~ 200	40	40 ~ 400
Equivalent input noise (μV) ¹	42	48	41	29

¹ Pixel rate of 156 kHz.

Table 4.2: Average and deviation of noise, INL and gain.

	MD01		MND01		MD02		MND02	
	mean	sd ¹	mean	sd ¹	mean	sd ¹	mean	sd ¹
Noise (μV) ²	35.2	1.9	45.9	3.9	36.7	2.2	27.2	1.3
INL (%) ²	0.213	0.047	0.61	0.14	0.160	0.038	0.186	0.072
Gain (ch/mV) ²	99.0	1.8	91.0	2.4	100.8	2.3	114.0	2.7

¹ standard deviation.

² Pixel rate of 19.5 kHz.

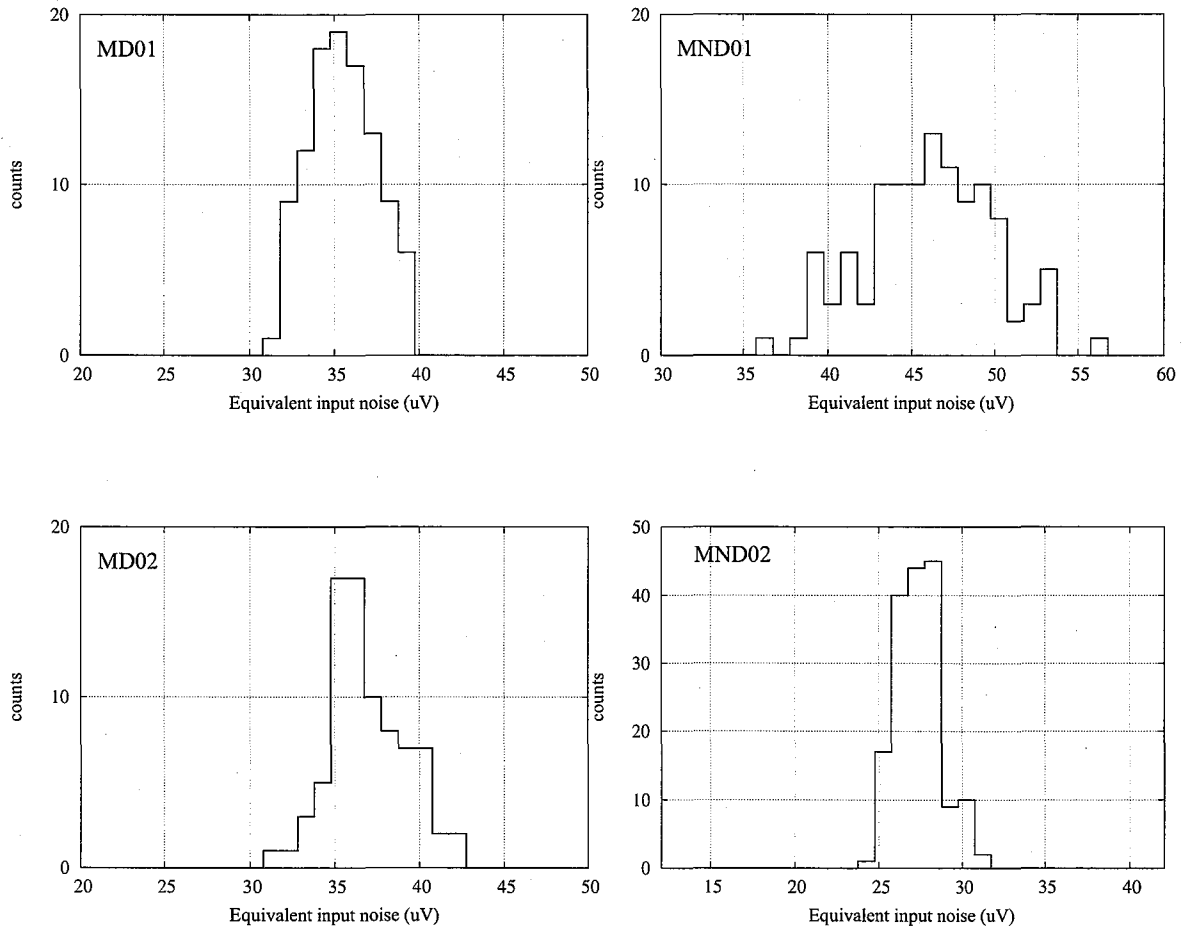


Figure 4.21: Noise distributions of MD01, MND01, MD02 and MND02. The number of samples is $8 \text{ ch} \times 10 \text{ chips} = 80$ in MD01, $8 \text{ ch} \times 13 \text{ chips} = 104$ in MND01, $8 \text{ ch} \times 13 \text{ chips} = 104$ in MD02, $8 \text{ ch} \times 21 \text{ chips} = 168$ in MND02.

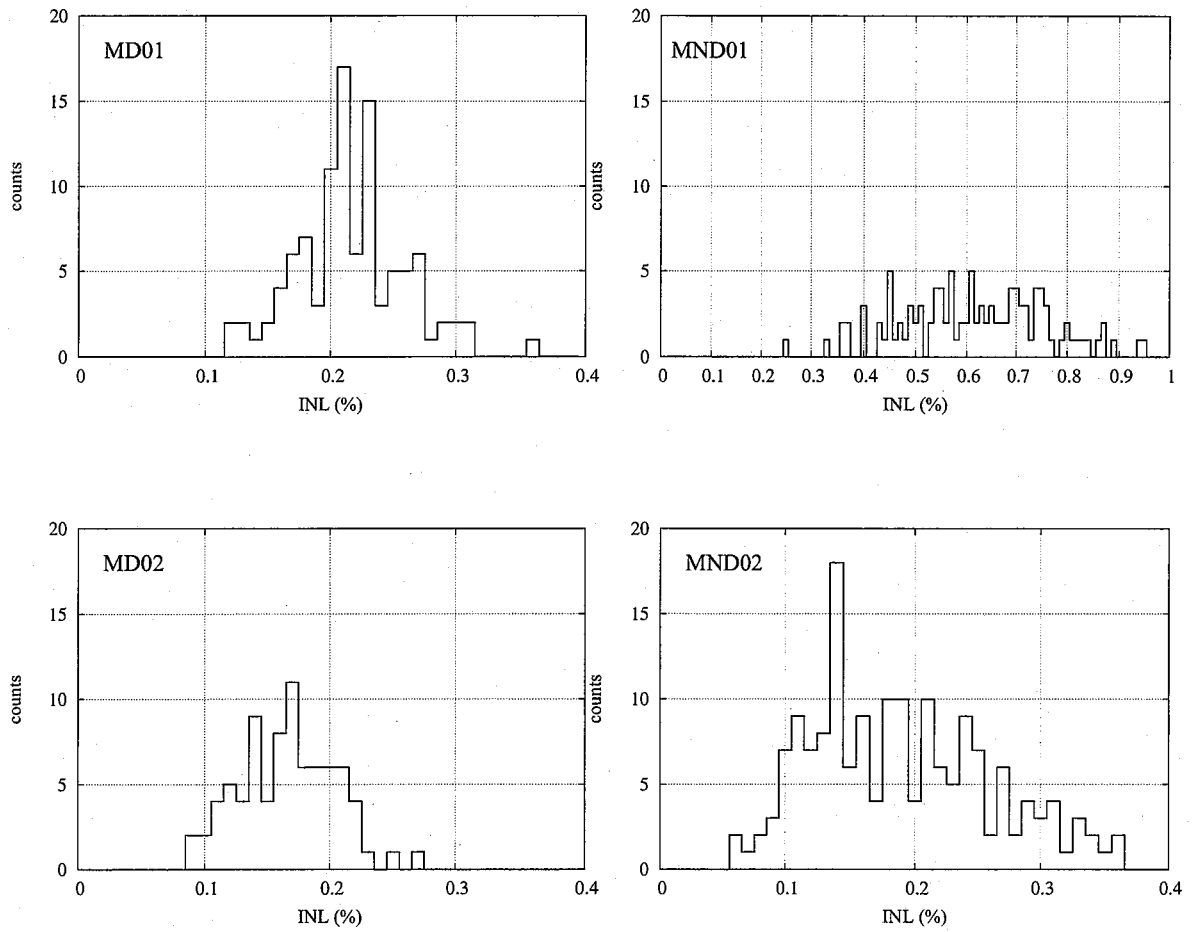


Figure 4.22: INL distributions of MD01, MND01, MD02 and MND02. The number of samples is $8 \text{ ch} \times 10 \text{ chips} = 80$ in MD01, $8 \text{ ch} \times 13 \text{ chips} = 104$ in MND01, $8 \text{ ch} \times 13 \text{ chips} = 104$ in MD02, $8 \text{ ch} \times 21 \text{ chips} = 168$ in MND02.

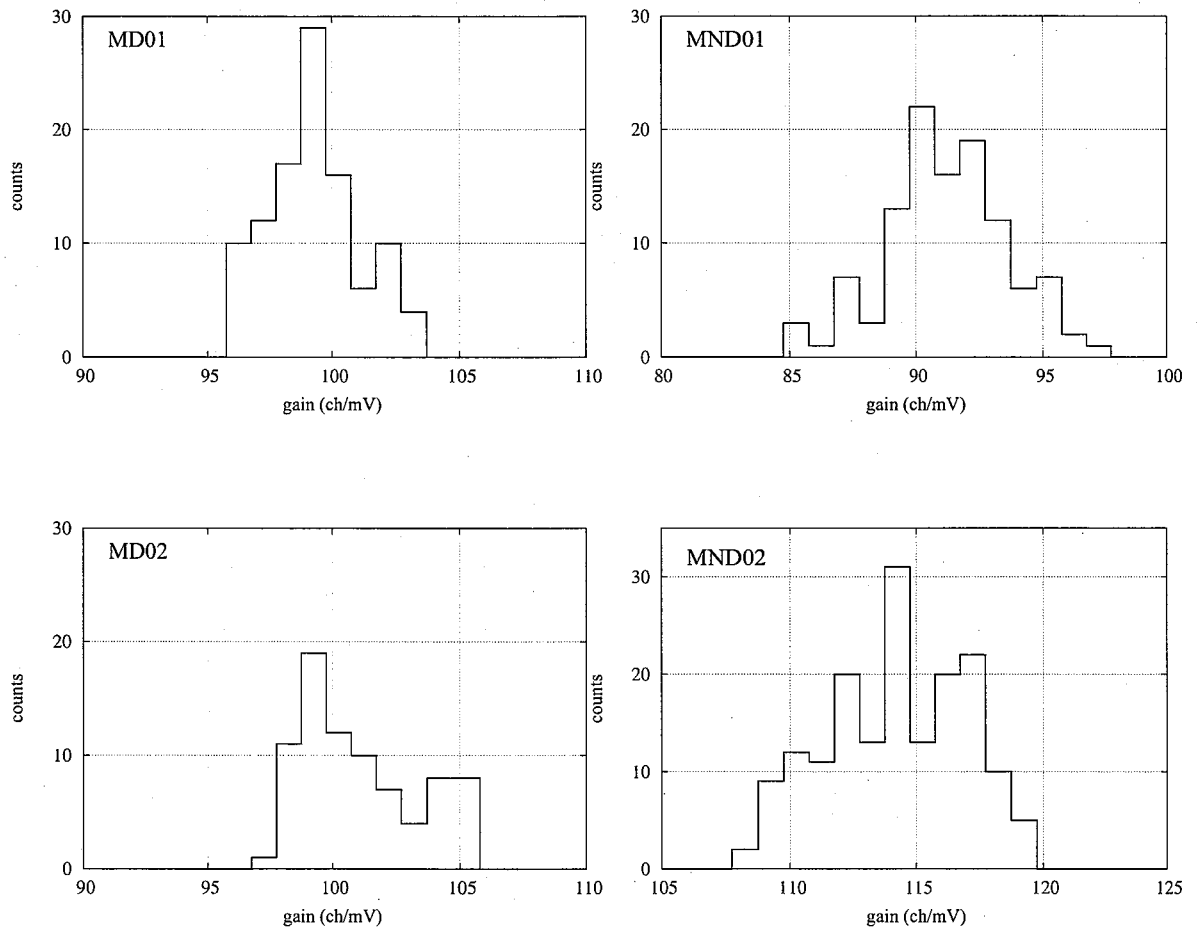


Figure 4.23: Gain distributions of MD01, MND01, MD02 and MND02. The number of samples is $8 \text{ ch} \times 10 \text{ chips} = 80$ in MD01, $8 \text{ ch} \times 13 \text{ chips} = 104$ in MND01, $8 \text{ ch} \times 13 \text{ chips} = 104$ in MD02, $8 \text{ ch} \times 21 \text{ chips} = 168$ in MND02.

Chapter 5

Performance of CCD camera systems using ASICs

5.1 Evaluation test setup

We confirmed that ASICs properly worked as we designed in the evaluation test using the pseudo signals. For the next step, we tested the readout of X-ray CCDs using MD01. The block diagram of the test system is shown in Fig. 5.1. The control signals for the ASIC and the drive signals for the CCD are provided by *MiKE* system shown in Fig. 5.2 (left) (Miyata, E. et al. 2001). *MiKE* system is the CCD test system developed in our laboratory. It provides 16 analog signals and 10 digital signals. The output range of analog signal is ± 12 V with resolution of 8-bit and the maximum toggle frequency of the signals is 7 MHz, which meets the requirement for the operation of wide variety of CCDs. The high DC voltages, over ± 12 V, for OD (the drain voltage used in an FDA) and the backside charging are given by other power supply units.

The analog and digital signals are generated by the signal pattern data loaded from the DP. The DP shown in Fig. 5.2 (right) consists of the CPU board (Armadillo-9) and the FPGA board. The former is a commercial product of Atmark Techno, Inc. and the latter is developed in our laboratory. The FPGA board is connected to the CPU board through PC/104 bus. Since the ASICs do not include the decimation filter as described in Sec. 3.4.2, we implemented the function in the FPGA and the filtered data were transmitted to the CPU board through PC/104 bus. The CPU board does not have a large memory enough to accept many CCD frame data. The CCD data are written to the hard disc drive (HDD) through network. *MiKE* system includes the readout system of CCD signals which consists of an iCDS circuit and ADC. Its noise level including CCD is 5 electrons and the energy resolution (FWHM) achieves 132 ± 2 eV as shown in

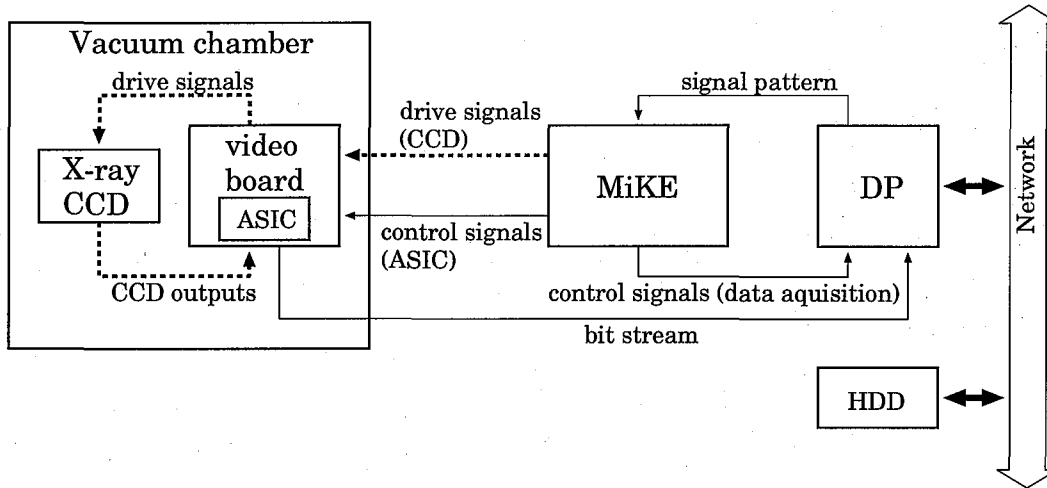


Figure 5.1: Block diagram of the readout system for X-ray CCDs. The dashed lines are analog signals and the solid lines are digital signals.

(Miyata, E. et al. 2005). We obtained the data by MD01 as well as by *MiKE* system for the comparison of their performance.

We developed the test board mounting an ASIC and connectors for CCDs (hereafter referred to the video board) to make the wire length between the CCD and the ASIC as short as possible. The X-ray CCD and the video board are placed in the vacuum chamber because the X-ray CCD need to be cooled to about -100°C in order to reduce the thermal noise. We irradiated CCDs with X-rays from Fe^{55} , $\text{Mn } K\alpha$ of 5.9 keV and $K\beta$ of 6.4 keV, for the evaluation of the readout noise and energy resolution. We are presently designing the X-ray CCD camera system for the SXI as shown in Sec. 4.6. One of the new approaches in the SXI is to utilize ASICs as the front-end electronics for the CCD signals. In this chapter, we show the performance of the CCD camera system using the ASIC and the X-ray CCDs developed for the prototype model of the SXI.

5.1.1 CCD-NeXT2

We developed the prototype CCD device for the SXI in the collaboration with Kyoto University and Hamamatsu Photonics K.K., Japan (hereafter referred to CCD-NeXT2). CCD-NeXT2 is a front-illuminated n-channel CCD with a large imaging area of $48\text{ mm} \times 42\text{ mm}$ (Tsunemi, H. et al. 2007). This device can operate either as in the full frame mode or in the frame transfer mode. Fig. 5.3 is photographs of CCD-NeXT2 and video board, and its specification is summarized in Table 5.1. The n-channel CCDs are employed as the focal plane detectors onboard many existing satellites, such as Suzaku, XMM-Newton, Chandra and so on. Since the n-channel CCDs have the high reliability for the space use,

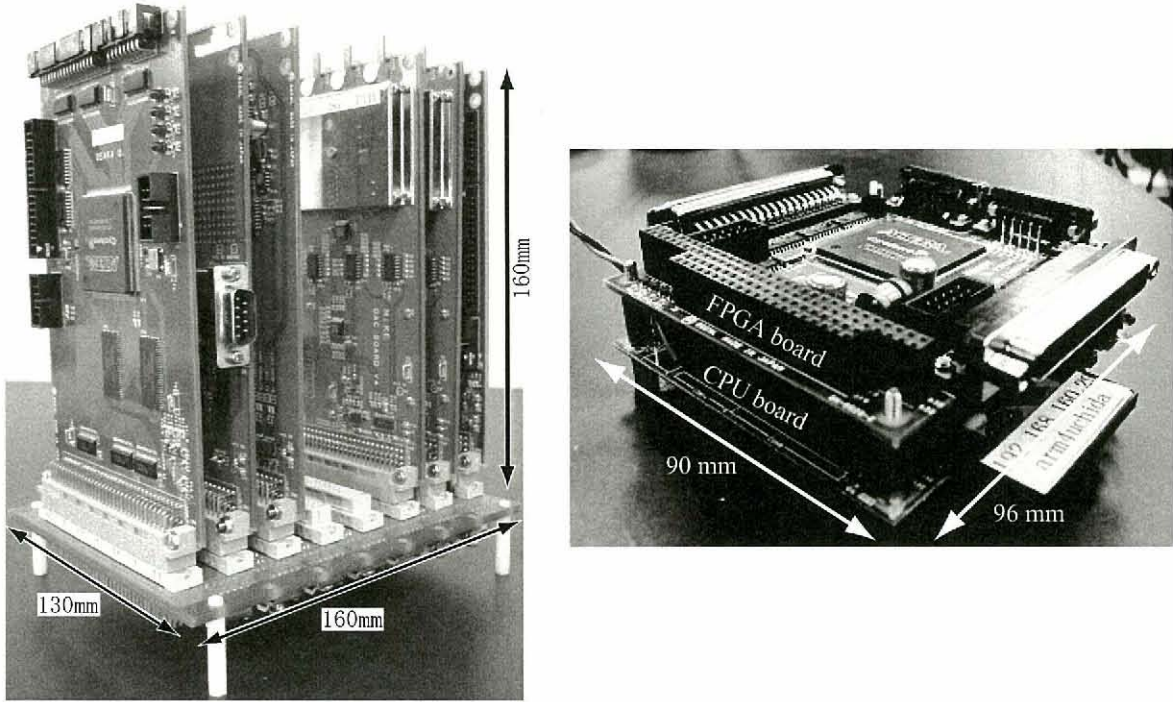


Figure 5.2: Photographs of MIKE system (left) and DP (right).

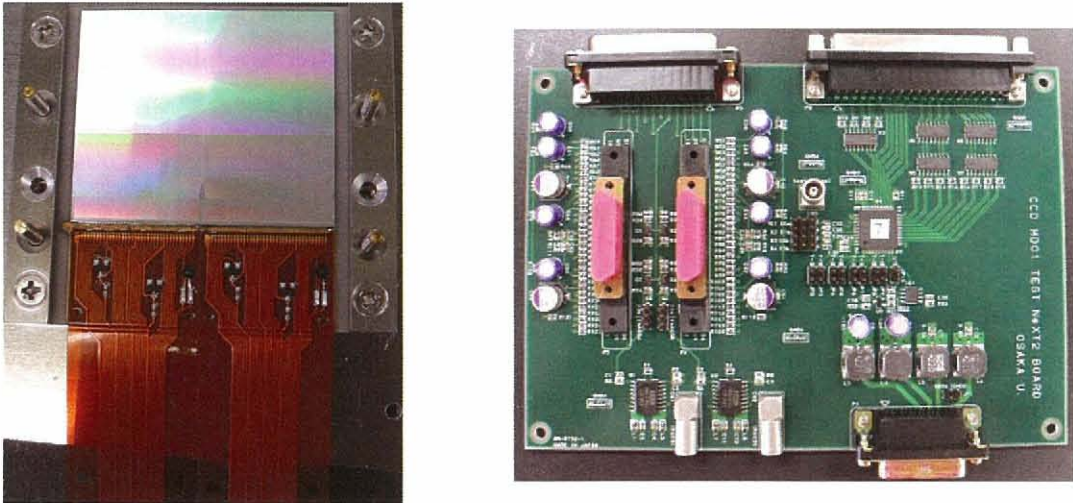


Figure 5.3: Photographs of CCD-NeXT2 (left) and its video board (right).

we first developed CCD-NeXT2 as the SXI prototype model. When we tested the ASIC by using CCD-NeXT2, the expected ENC of the ASIC at the pixel rate of 39 kHz is estimated as

$$\text{ENC}_{\text{ASIC-next2}} = \frac{\text{Equivalent input noise } (\mu\text{V})}{\text{Conversion factor } (\mu\text{V}/e^-)} = \frac{37 (\mu\text{V})}{4.1 (\mu\text{V}/e^-)} \approx 9.0 e^-. \quad (5.1)$$

5.1.2 Pch2k4k

We also have been developing the p-channel CCDs in parallel with the n-channel CCDs. Since we can employ the n-type silicon wafer with high resistivity compared with that of p-type silicon, the p-channel CCDs succeeded in extending the thickness of depletion layer to 200~300 μm , which is more than 3 times thicker than that of n-channel CCDs (Matsuura, D. et al. 2006a), (Matsuura, D. et al. 2006b). The thick depletion layer enables us to increase the detection efficiency in the energy band of more than 10 keV and easily fabricate a back-illuminated CCD. It is important to detect the low energy X-rays of less than 0.5 keV. The p-channel CCDs are initially developed by a group of Lawrence Berkeley National Laboratory (LBNL) in the collaboration with Lick Observatory of the University of California Observatories (UCO). In Japan, the National Astronomical Observatory Japan (NAOJ), Osaka University and Kyoto University have been developing the p-channel CCDs in collaboration with Hamamatsu Photonics K.K.. Pch2k4k is a back-illuminated CCD with large imaging area of 3 cm \times 6 cm and thick depletion layer of 200 μm (Tsunemi, H. et al. 2007) developed for SUBARU HyperSuprime-Cam (Nakaya, H. et al. 2008). This device can operate either as in the full frame mode and in the frame transfer mode. We plan to fabricate the prototype p-channel CCD for SXI based on the heritage of CCD-NeXT2 and Pch2k4k. Figure 5.4 shows the photographs of Pch2k4k and its video board. The CCD specification is summarized in table. 5.1.

Because Pch2k4k is a back-illuminated CCD and has the thick depletion layer, the signal charge clouds spread during the drift from the interaction point to the potential well. The number of single pixel events decrease compared with the results of a front-illuminated CCD. We operated Pch2k4k in the 4 \times 4 pixel sum-mode. This mode is to sum the charges in 4 \times 4 pixels during the vertical and horizontal charge transfers. Therefore, the effective pixel size corresponds to 60 μm \times 60 μm . When we tested the ASIC by using Pch2k4k, the expected ENC of the ASIC at the pixel rate of 39 kHz can be written as

$$\text{ENC}_{\text{ASIC-pch}} = \frac{\text{Equivalent input noise } (\mu\text{V})}{\text{Conversion factor } (\mu\text{V}/e^-)} = \frac{37 (\mu\text{V})}{5.5 (\mu\text{V}/e^-)} \approx 6.7 e^-. \quad (5.2)$$

5.2 Test results

We operated X-ray CCDs at the pixel rate of about 40 kHz, the maximum pixel rate of this system. Since Pch2k4k was driven in the 4 \times 4 pixel sum-mode, the pixel rate of Pch2k4k was a little lower than that of CCD-NeXT2. The operation temperatures of CCD-NeXT2 and Pch2k4k were -100°C and -70°C , respectively. Their temperatures

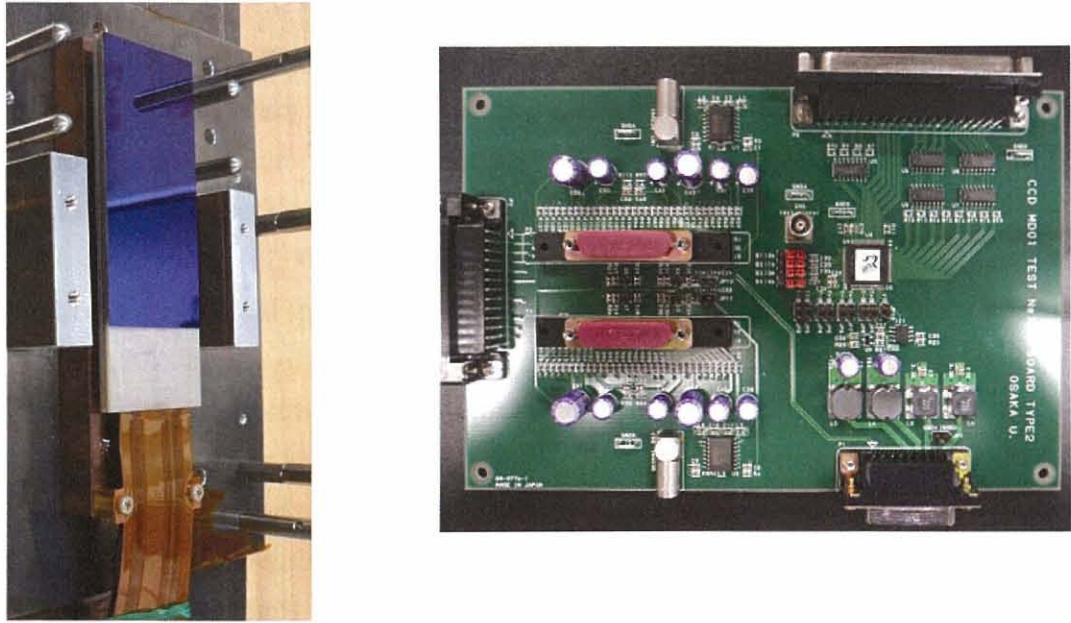


Figure 5.4: Photographs of Pch2k4k (left) and video board (right).

Table 5.1: Specification of X-ray CCDs.

	CCD-NeXT2	Pch2k4k
Pixel size (Imaging area)	$24 \mu\text{m} \times 24 \mu\text{m}$	$15 \mu\text{m} \times 15 \mu\text{m}$
Format (Imaging area)	1000×2000	2000×2000
Pixel size (Storage area)	$24 \mu\text{m} \times 18 \mu\text{m}$	$15 \mu\text{m} \times 15 \mu\text{m}$
Format (Storage area)	1000×2000	2000×2000
Number of readout node	4	4
Thickness of depletion layer	$100 \mu\text{m}$	$200 \mu\text{m}$
Si wafer	P-type	N-type
Conversion factor	$4.1 \mu\text{V}/e^-$	$5.5 \mu\text{V}/e^-$

were determined to optimize the charge transfer efficiency for each device. Fig. 5.5 shows an X-ray image with a mesh by using the X-ray generator whose beam source size is a few μm . We placed the metal mesh at the front of the CCD and the generator 2 meters apart from the CCD. The mesh pattern is clearly imaged, which shows the CCD signals are properly processed by the ASIC and the test system properly works.

We briefly explain about the event selection for the CCD data analysis here. The detailed analysis method is illustrated in (Hiraga, J. 2002). A pulse height of each pixel contains a signal component as well as a bias component that we call “dark level”. To

extract the signal component, we first determine the dark level of each pixel and subtract that from the pulse height. The dark level is the averaged pixel level of 32 frames in this analysis. The charge cloud splits into adjacent pixels when the interaction occurs at the pixel boundary. We determine the threshold, which we call “split threshold”, to distinguish whether the relevant pixel is the split one or the dark noise. We set the split threshold to 3 sigma of the readout noise level in this chapter. We should select only single pixel events to achieve the high energy resolution. However, we use a part of the split events to improve the detection efficiency. ASCA grades (A. Yamashita, A. et al. 1997) is employed to separate the events into 8 patterns (g0~g7), g0 is a single event and g1~g7 are split events. In XIS, the spectrum is created by using g0,2,3,4 and 6 events.

Figures 5.6~ 5.8 show the spectra of ^{55}Fe using g0 and g02346 events obtained by CCD-NeXT2 and Pch2k4k, respectively. Note that the pixel data of odd and even columns are processed by separate ADCs, odd and even ADCs. The standard deviation of the ADC gain in MD01 is 1.8 (ch/mV) as shown in Table 4.2. We compensated the difference of the ADC gain to prevent the degradation of energy resolution before the data combine. Two emission lines, Mn $K\alpha$ (5.9 keV) and $K\beta$ (6.5 keV), are clearly seen and the low energy tail of each peak is not found in these spectra. We fitted each line with a Gaussian function and a constant to evaluate energy resolution.

Readout noise

The readout noise each channel is shown in Tables 5.2 and 5.4. The noise of channel3 is worse than those of other channels by 30~100 %, which is a little larger than the noise distribution of MD01 shown in Fig. 4.21. Tables 5.3 and 5.5 exhibit the test results of MiKE system by using the same CCD devices. The noise level of channel3 shows no significant difference compared with other channels. Since the noise of CCDs and ASICs are proper from the test results, we suppose that the layout design of the video boards, especially for the analog line between the ASIC and CCD, leads to the noise degradation of channel3. We excluded the data of channel3 in the calculation of the averaged readout noise and energy resolution. The averaged readout noises of Channel0~Channel2 for CCD-NeXT2 and Pch2k4k are $9.8 e^-$ and $7.5 e^-$, respectively. The expected noise from the ASIC is $9.0 e^-$ in eq. 5.1 when we use CCD-NeXT2. The residual between the measured noise and the calculated one of the ASIC corresponds to the noise component from CCD-NeXT2. The noise from CCD-NeXT2 is given as

$$\text{ENC}_{\text{next2}} = \sqrt{(9.8 e^-)^2 - (9.0 e^-)^2} \approx 3.9 e^-. \quad (5.3)$$

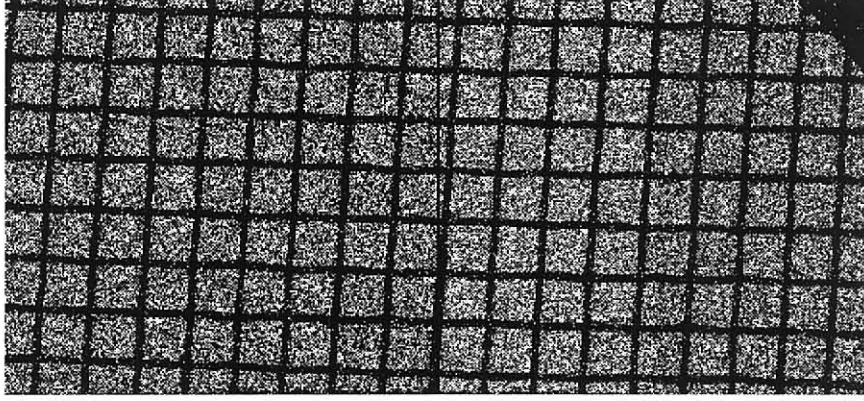


Figure 5.5: Frame image with a size of 24 mm \times 48 mm obtained by using CCD-NeXT2. The mesh pitch seen in the image is 3 mm.

In the case of Pch2k4k is

$$\text{ENC}_{\text{pch2k4k}} = \sqrt{(7.5 e^-)^2 - (6.7 e^-)^2} \approx 3.4 e^-. \quad (5.4)$$

We concluded that the ASIC noise is dominant in the total system noise from these test results.

Energy resolution

The energy resolution of each channel is shown in Tables 5.2 and 5.4. We merged the spectra of channel0~channel2 shown in Figs. 5.6~ 5.9 after the compensation for the gain difference. The energy resolution of the merged spectra using only single events for CCD-NeXT2 and Pch2k4k is 162 eV(FWHM) and 150 eV(FWHM) at 5.9 keV, respectively. Assuming only the Fano noise and the readout noise contribute to the degradation of energy resolution, we calculate the expected value by using CCD-NeXT2 as follows,

$$\text{Energy resolution}_{\text{next2}} = \sqrt{(117 \text{ eV})^2 + (2.35 \times 3.65 \text{ eV}/e^- \times 9.8 e^-)^2} \approx 144 \text{ eV}. \quad (5.5)$$

In the case of Pch2k4k is

$$\text{Energy resolution}_{\text{pch2k4k}} = \sqrt{(117 \text{ eV})^2 + (2.35 \times 3.65 \text{ eV}/e^- \times 7.5 e^-)^2} \approx 136 \text{ eV}. \quad (5.6)$$

The unknown noise is about 7~9 e^- in order to meet the test results. Figure 5.10 shows the energy resolution and relative event count of single pixel events as a function of the split threshold. From this result, the energy resolution clearly depends on the split threshold, and there is the trade-off between the energy resolution and event count. This is one of the unknown noise sources.

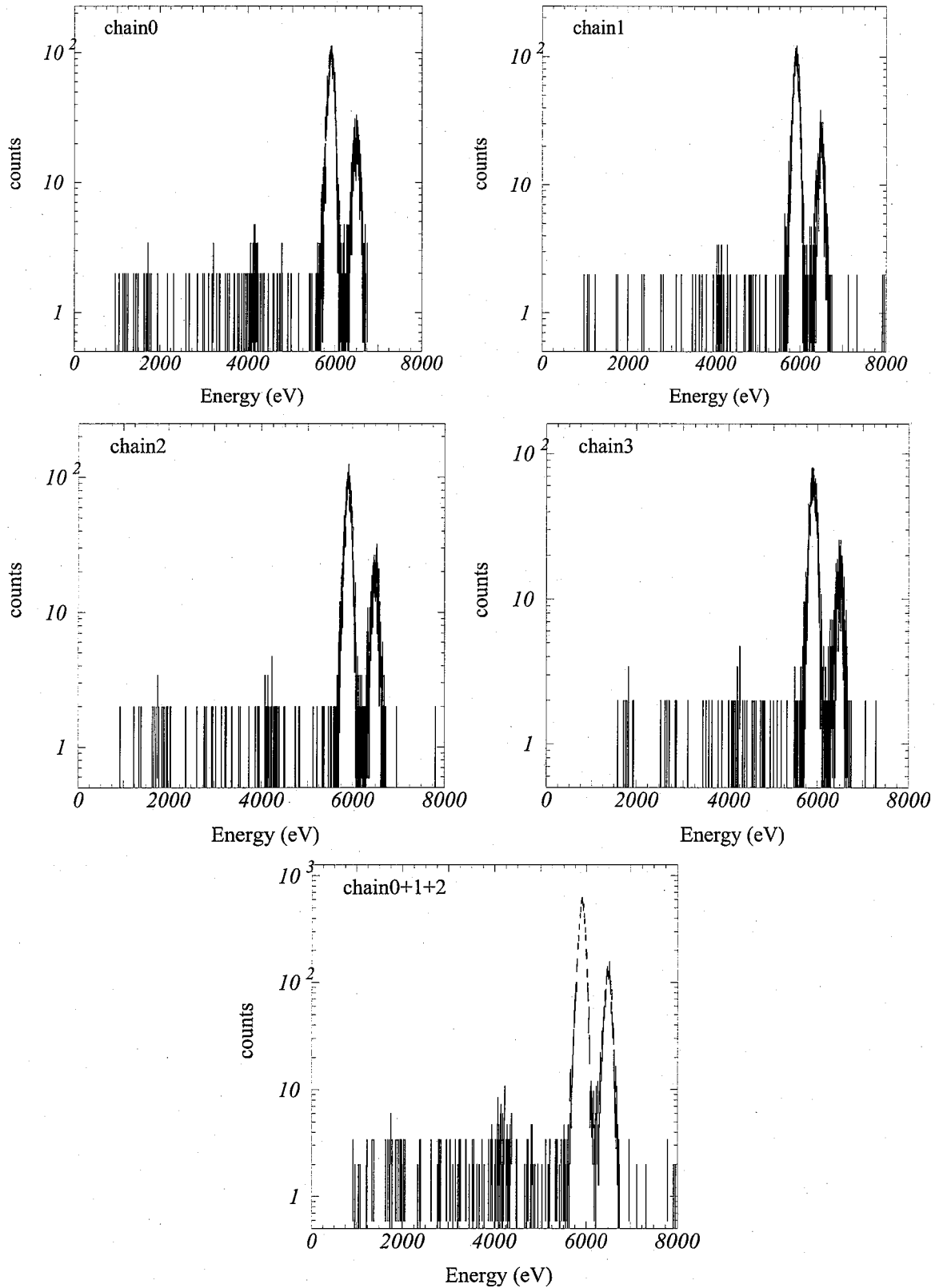


Figure 5.6: X-ray spectra (g_0) of ^{55}Fe obtained by CCD-NeXT2. Note that the peak of 1.7 keV is Si $K\alpha$ line, and that of 4.2 keV is Si escape line.

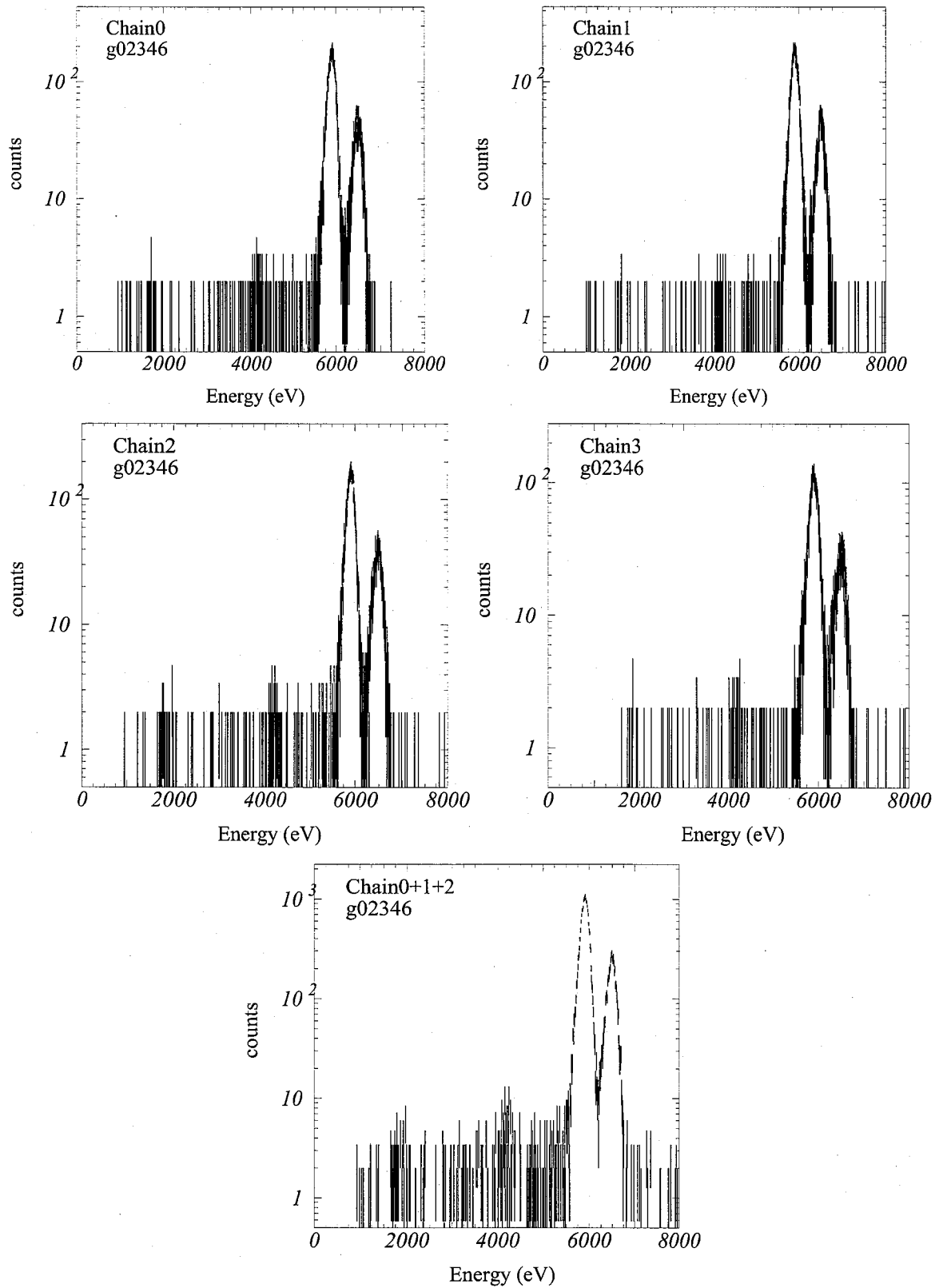


Figure 5.7: X-ray spectra(g02346) of ^{55}Fe obtained by CCD-NeXT2. Note that the peak of 1.7 keV is Si $K\alpha$ line, and that of 4.2 keV is Si escape line.

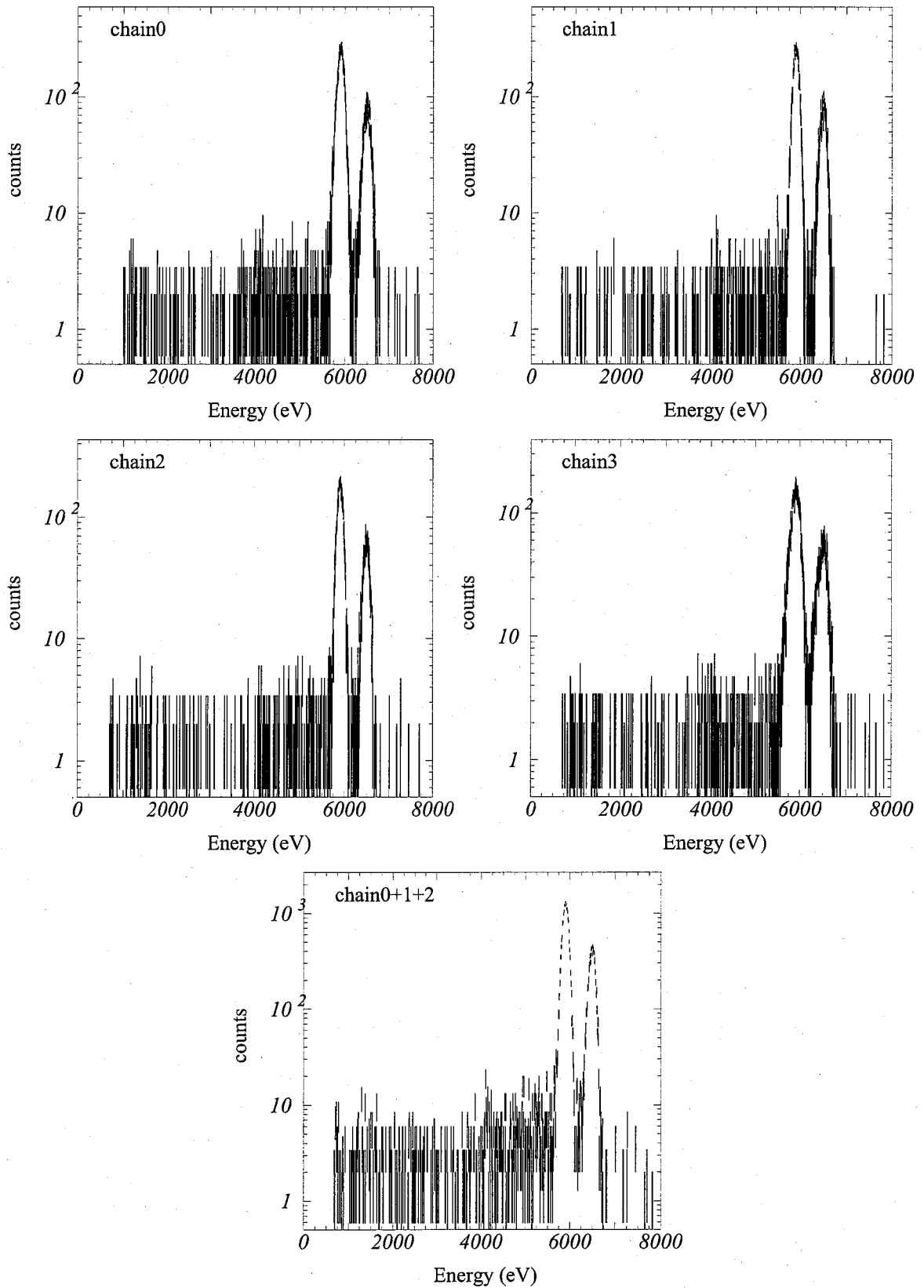


Figure 5.8: X-ray spectra (g0) of ⁵⁵Fe obtained by Pch2k4k. Note that the peak of 1.7 keV is Si K α line, and that of 4.2 keV is Si escape line.

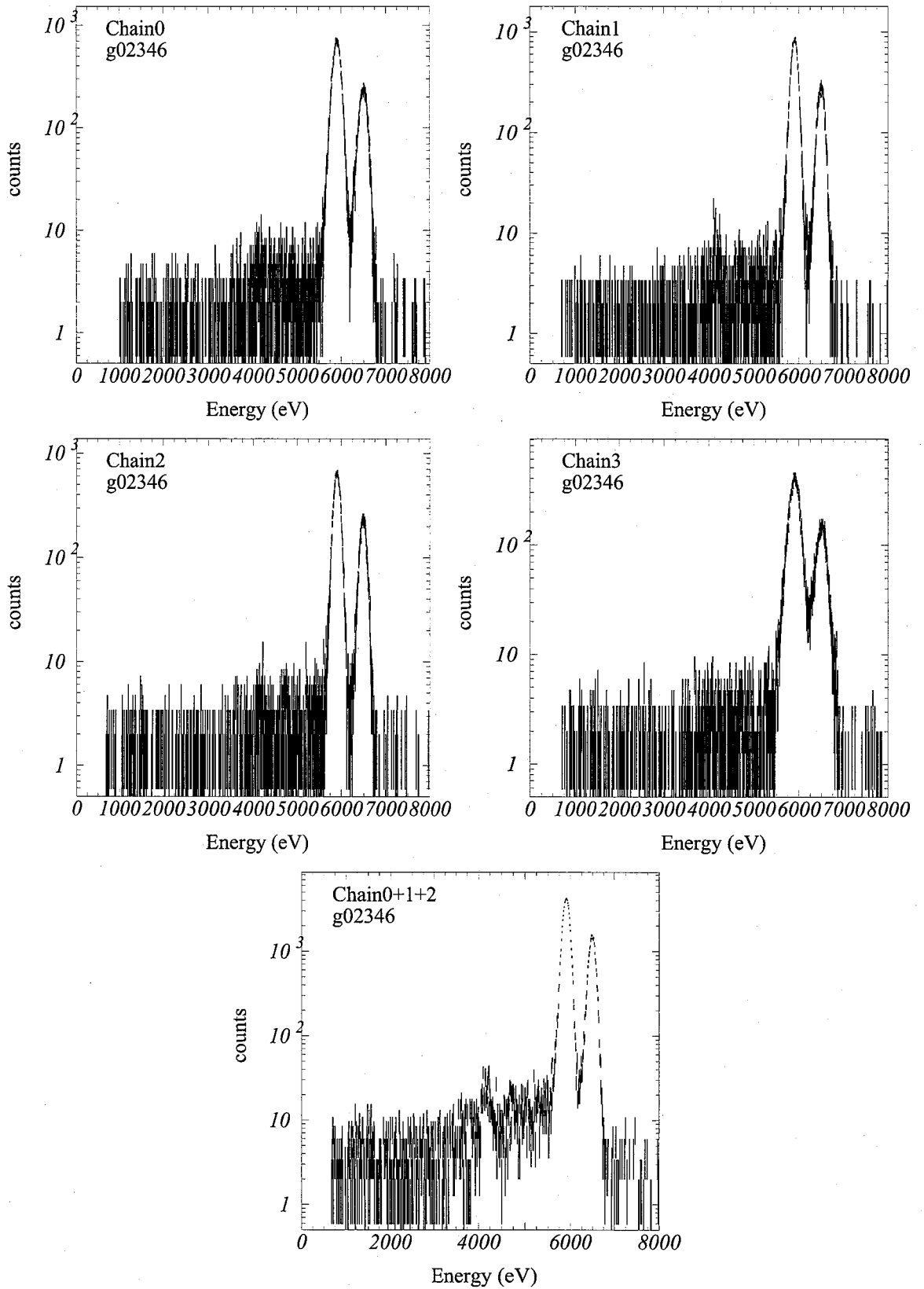


Figure 5.9: X-ray spectra (g02346) of ^{55}Fe obtained by Pch2k4k. Note that the peak of 1.7 keV is Si $K\alpha$ line, and that of 4.2 keV is Si escape line.

Table 5.2: Test condition and results (CCD-NeXT2) by MD01.

Operation temperature	-100 °C
Pixel rate	44 kHz
Ch0 ENC (even/odd)	10.3/10.2 e ⁻
Ch1 ENC (even/odd)	10.1/10.1 e ⁻
Ch2 ENC (even/odd)	9.1/9.0 e ⁻
Ch3 ENC (even/odd)	12.9/12.0 e ⁻
Ch0 Energy resolution (g0/g02346) [†]	168 ± 4 eV / 200 ± 4 eV
Ch1 Energy resolution (g0/g02346) [†]	156 ± 4 eV / 192 ± 3 eV
Ch2 Energy resolution (g0/g02346) [†]	158 ± 4 eV / 193 ± 3 eV
Ch3 Energy resolution (g0/g02346) [†]	176 ± 5 eV / 212 ± 3 eV
Ch0+1+2 Energy resolution (g0/g02346) [†]	162 ± 2 eV / 197 ± 1 eV
ENC* (even/odd)	5.5/5.5 e ⁻
Energy resolution (g0/g02346) ^{†*}	140 ± 2 eV / 153 ± 2 eV

[†] Energy resolution (FWHM) at 5.9 keV.

* Results in 4 average method.

Table 5.3: Test condition and results (CCD-NeXT2) by *MiKE* system.

Operation temperature	-105 °C
Pixel rate	133 kHz
Ch1 ENC	6.3 ± 0.1 e ⁻
Ch3 ENC	6.9 ± 0.1 e ⁻
Ch1 Energy resolution (g0/g02346) [†]	143 ± 5 eV / 167 ± 4 eV
Ch3 Energy resolution (g0/g02346) [†]	140 ± 4 eV / 166 ± 3 eV

[†] Energy resolution (FWHM) at 5.9 keV.

Table 5.4: Test condition and results (Pch2k4k) by MD01.

Operation temperature	$-70\text{ }^{\circ}\text{C}$
Pixel rate	41 kHz
Ch0 ENC (even/odd)	9.4/8.9, e^{-}
Ch1 ENC (even/odd)	6.6/6.2, e^{-}
Ch2 ENC (even/odd)	6.9/7.1, e^{-}
Ch3 ENC (even/odd)	14.2/15.7, e^{-}
Ch0 Energy resolution (g0/g02346) [†]	$176 \pm 2\text{ eV} / 207 \pm 2\text{ eV}$
Ch1 Energy resolution (g0/g02346) [†]	$150 \pm 2\text{ eV} / 171 \pm 1\text{ eV}$
Ch2 Energy resolution (g0/g02346) [†]	$146 \pm 2\text{ eV} / 168 \pm 1\text{ eV}$
Ch3 Energy resolution (g0/g02346) [†]	$228 \pm 4\text{ eV} / 273 \pm 3\text{ eV}$
Ch0+1+2 Energy resolution (g0/g02346) [†]	$150 \pm 1\text{ eV} / 171 \pm 1\text{ eV}$
ENC* (even/odd)	5.3/6.6, e^{-}
Energy resolution (g0/g02346) ^{†*}	$140 \pm 2\text{ eV} / 165 \pm 1\text{ eV}$

[†] Energy resolution (FWHM) at 5.9 keV.

* Results in 4 average method.

Table 5.5: Test condition and results (Pch2k4k) by *MiKE* system.

Operation temperature	$-70\text{ }^{\circ}\text{C}$
Pixel rate	52 kHz
Ch0 ENC	$6.76 \pm 0.08e^{-}$
Ch1 ENC	$6.39 \pm 0.08e^{-}$
Ch2 ENC	$6.74 \pm 0.08e^{-}$
Ch3 ENC	$6.28 \pm 0.08e^{-}$
Ch0 Energy resolution (g0/g02346) [†]	$138 \pm 3\text{ eV} / 160 \pm 2\text{ eV}$
Ch1 Energy resolution (g0/g02346) [†]	$142 \pm 3\text{ eV} / 158 \pm 2\text{ eV}$
Ch2 Energy resolution (g0/g02346) [†]	$139 \pm 3\text{ eV} / 157 \pm 2\text{ eV}$
Ch3 Energy resolution (g0/g02346) [†]	$137 \pm 3\text{ eV} / 158 \pm 2\text{ eV}$

[†] Energy resolution (FWHM) at 5.9 keV.

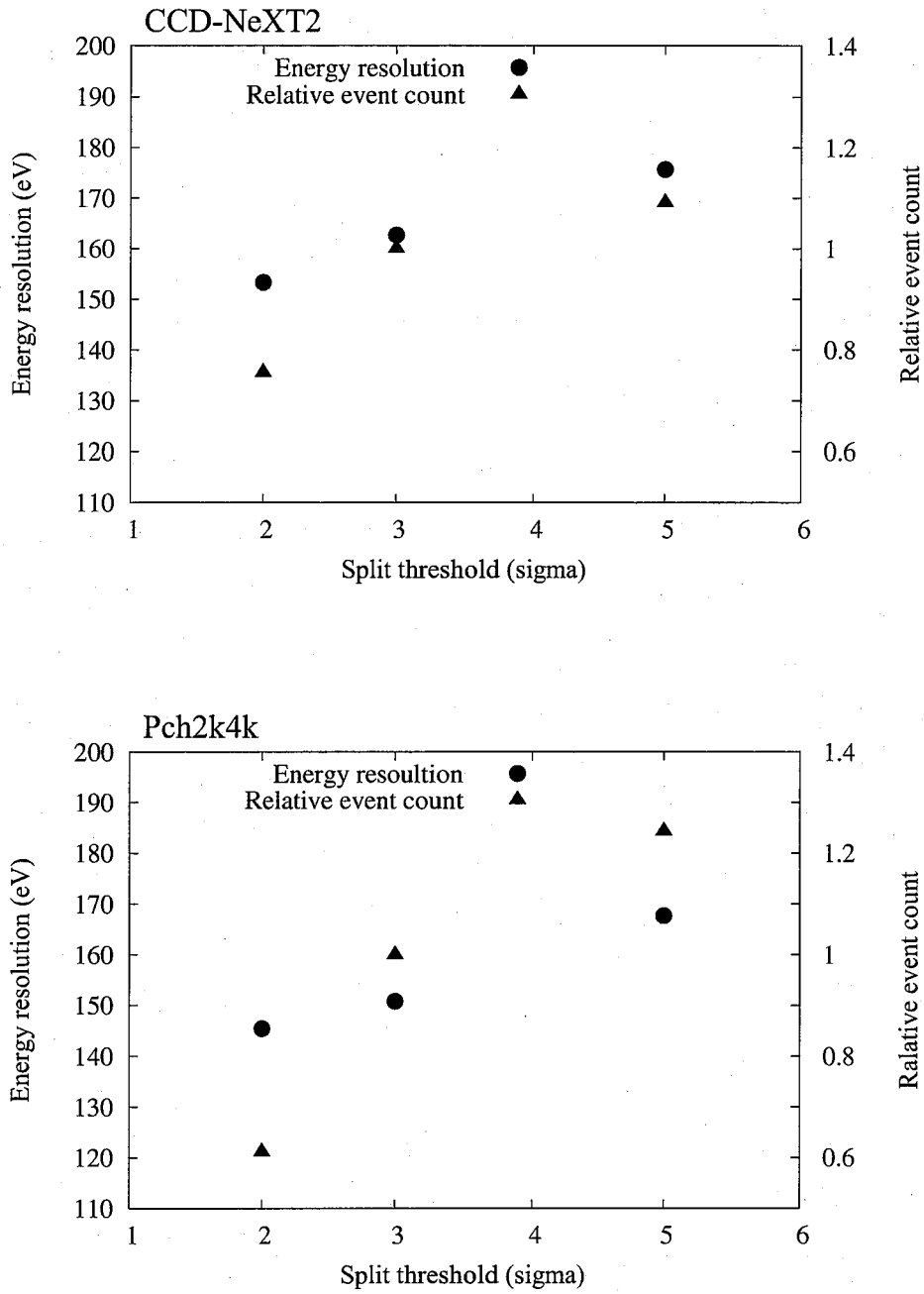


Figure 5.10: Relation between energy resolution or event count and split threshold in the test results of CCD-NeXT2 (top) and Pch2k4k (bottom).

5.3 Test results using 4 average method

We showed that the noise from the ASIC was dominant in that of the CCD camera system in Sec. 5.2. We tested another readout method as shown in Fig. 5.11 to improve the noise level of the ASIC without the reduction of pixel readout rate. In this readout method, one CCD signal is simultaneously processed by separate 4 readout channels and we obtain the average of 4 channel outputs (hereafter referred to 4 average method). Assuming the noise in each channel is not correlated to those in other channels, we can reduce the ASIC noise by 50% in this method.

We verified that the noise level decreased from $34 \mu\text{V}$ to $18 \mu\text{V}$ when we took 4 average method. In the actual readout test using X-ray CCDs, the readout noise and energy resolution at 5.9 keV are $5.5 e^-$ and 140 eV at the pixel readout rate of 44 kHz, respectively. Figure 5.12 shows the X-ray spectra of ^{55}Fe obtained by CCD-NeXT2 and Pch2k4k in 4 average method. These test results are summarized in Tables 5.2 and 5.4. The expected noise from CCD-NeXT2 is

$$\text{ENC}_{\text{next2-4ch}} = \sqrt{(5.5 e^-)^2 - \left(\frac{18 (\mu\text{V})}{4.1 (\mu\text{V}/e^-)} \right)^2} \approx 3.3 e^-. \quad (5.7)$$

In the case of Pch2k4k is

$$\text{ENC}_{\text{pch2k4k-4ch}} = \sqrt{(5.3 e^-)^2 - \left(\frac{18 (\mu\text{V})}{5.5 (\mu\text{V}/e^-)} \right)^2} \approx 4.2 e^-. \quad (5.8)$$

We can decrease the noise of MD01 down to that of CCDs. Our ASIC could be achieve the same noise level as the conventional readout system (*MiKE*) system shown in Tables 5.3 and 5.5.

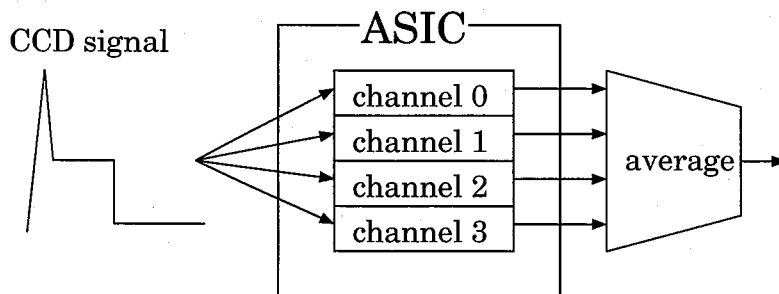


Figure 5.11: Block diagram to illustrate 4 average method.

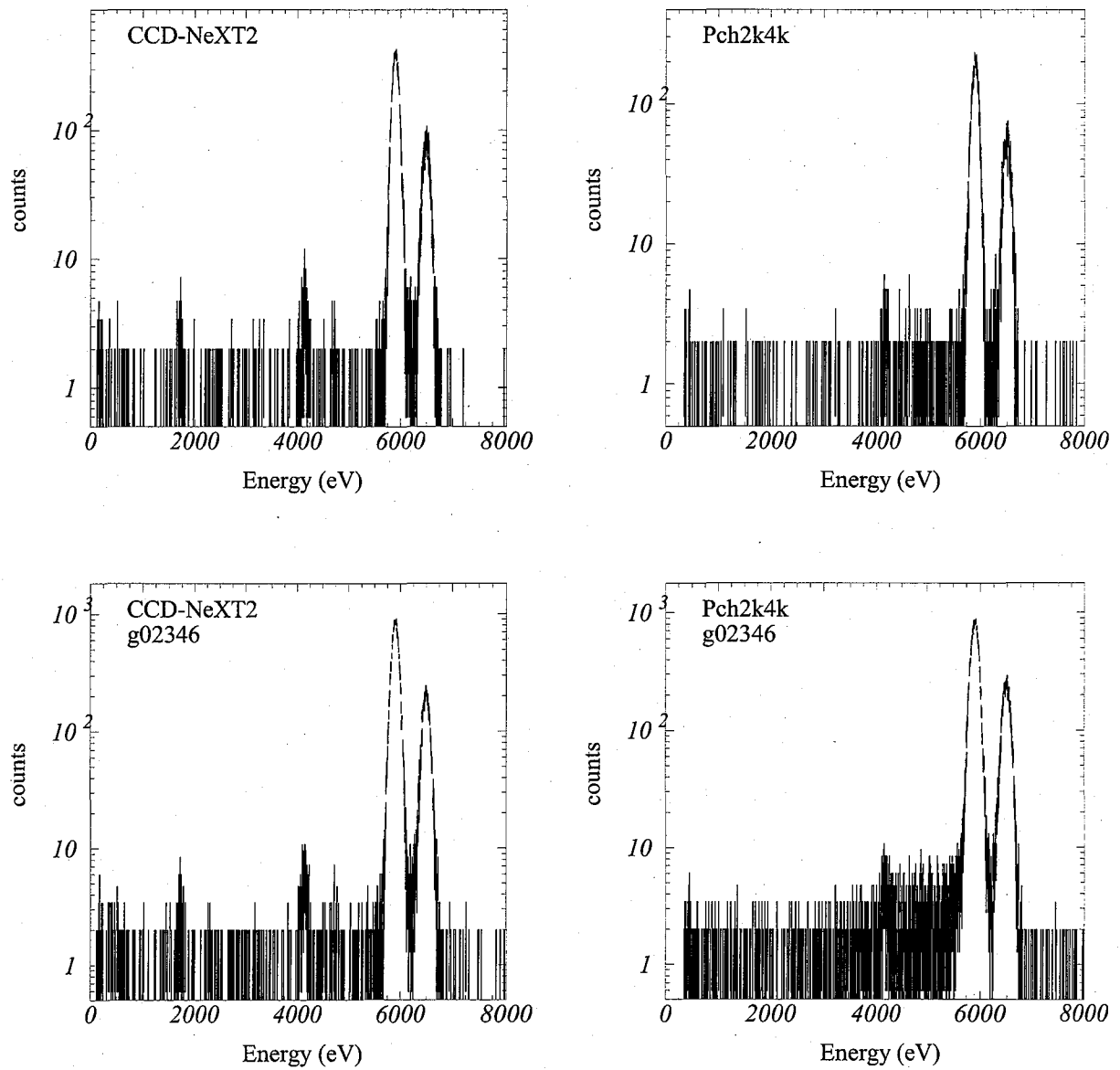


Figure 5.12: X-ray spectra of ^{55}Fe obtained by CCD-NeXT2 (left) and Pch2k4k (right) in 4 average method.

Chapter 6

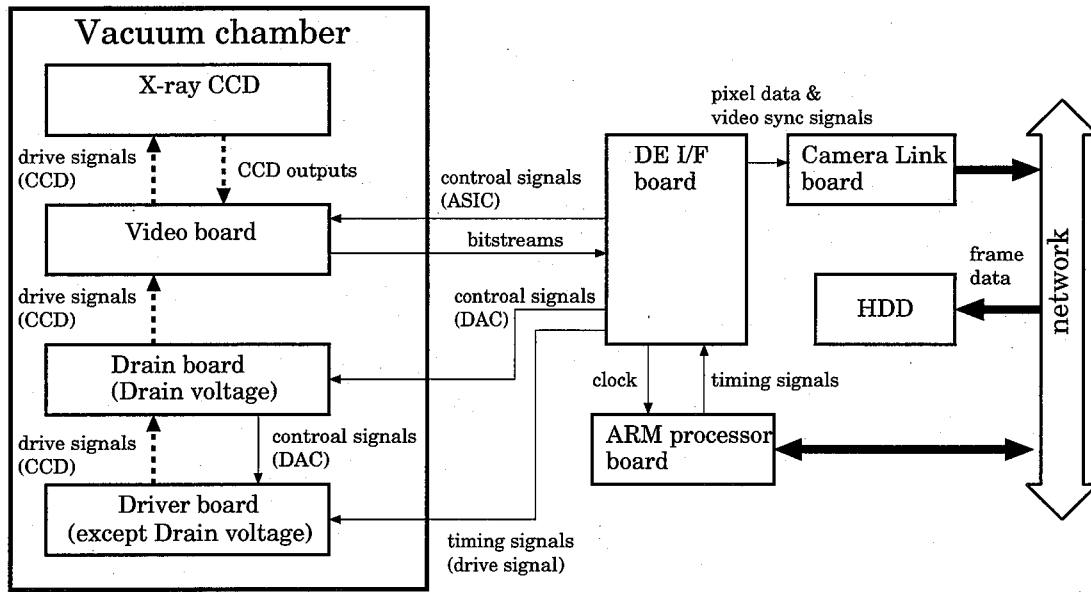
High speed drive and readout system for X-ray CCDs

6.1 *C-link system*

We evaluated the performance of the ASICs using the X-ray CCDs at the moderate pixel rate (40 kHz) as shown in Chapter 5. The ASICs properly work at the pixel rate up to 600 kHz as shown in Chapter 4. For the next step, we test the readout of X-ray CCDs at the high pixel rate of more than 100 kHz. The readout test of CCD using the ASIC previously had been performed by *MIKE* system. However, if we operate the ASIC at the pixel rate of more than 40 kHz by *MIKE* system, we need to considerably revise its system. Additionally, the data rate of PC/104 bus, which is utilized in our DP shown in Fig. 5.2 (left), is less than 8 MByte/sec. Assuming the pixel rate of 600 kHz and the data size is 2 byte/pixel, the maximum number of channels is up to 6. We should increase the number of readout nodes of CCDs to speed up the frame rate. We are developing the new readout system to realize the multi-readout employing ~ 10 ASICs at the high pixel rate. Figure 6.1 shows the block diagram of this new readout system (hereafter referred to *C-link system*). *C-link system* consists of Camera Link, ARM processor, Digital Electronics InterFace (DE I/F), driver, drain and video boards.

6.1.1 Camera Link board

We employed the commercial framegrabber board (PCI DV C-Link), which supports Camera Link, provided by Engineering Design Team (EDT), Inc. for data acquisition. Camera Link is an interface protocol to standardize the interconnects between cameras and framegrabbers as detailed in (Camera Link spec). Since the several camera and

Figure 6.1: Block diagram of *C-link* system.

framegrabber manufacturers employ Camera Link, their products are interchangeable. Figure 6.2 shows the data format of Camera Link in 1 data transfer cycle. 5 LVDS pairs, 4 data lines and 1 clock line, transmit the pixel data of 24 bits and video sync signals of 3 bits to the framegrabber board. The video sync signals are Frame Valid (FVAL), Line Valid (LVAL) and Data Valid (DVAL). When all signals of FVAL, LVAL and DVAL are clocked high as shown in Fig. 6.3, the pixel data is acquired. EDT's Camera Link solutions support the software for Windows, Linux, MacOS and so on. We developed the software for the data acquisition by utilizing the supported ones and CFITSIO (CFITIO web page). The obtained data format is Flexible Image Transport System (FITS), which is widely used in the astronomical investigation. The maximum data rate of PCI DV C-Link board is 117 MByte/sec at the bus clock rate of 33 MHz, which enables us to simultaneously obtain the data from 24 ASICs at the pixel rate of 600 kHz.

6.1.2 DE I/F and ARM processor boards

DE I/F board shown in Fig. 6.4 consists of the sequencer, FPGA and transmitter IC for Camera Link. The sequencer is the state counter and decoder to generate the control signals for the CCD drive, such as the vertical and horizontal transfer clocks and reset clock, and for the ASIC, such as `Clamp`, `Odd`, `Deint` and `Int` signals, based on the reference clock given by the FPGA. The sequencer received the signal pattern from the ARM processor board (AT91EB40A), which is the commercial product of Atmel Corporation.

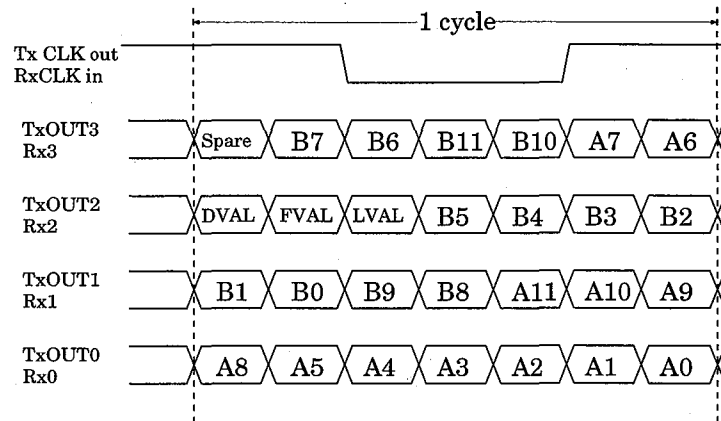


Figure 6.2: Data format of Camera Link in 1 data transfer cycle.

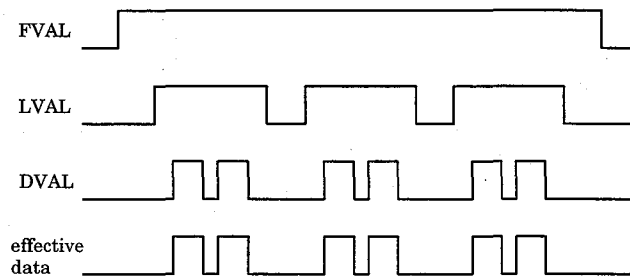


Figure 6.3: Signal diagram for the explanation of FVAL, LVAL and DVAL signals.

The ARM board also transmits the serial signals to 5-bit DAC in the ASIC and to DACs on the driver board to generate the CCD drive signals.

We implemented the clock divider, LVDS drivers, decimation filters and pixel data buffer in the FPGA. The clock divider provides the sample clock to the ASICs, which is the base clock of 100 MHz divided by even numbers, such as 50, 25, 12.5, 6.25, 3.125 and 1.5625 MHz. It also generates the reference clock used in the sequencer, which is the sample clock divided by 5. The LVDS drivers convert the LVCMOS signals of the control signals for the ASIC to LVDS pairs. The decimation filtered data is written in the pixel data buffer shown in Fig 6.5. The 2 buffers alternatively store the pixel data of 1 horizontal row. The rest buffer, which does not perform the data acquisition, outputs the stored data to the transmitter IC. The pixel data buffer minimizes the delay time and realizes the real-time data acquisition. The transmitter IC converts 28 bits parallel data from the FPGA to the data format of Camera Link, 4 LVDS data streams, shown in Fig. 6.2.

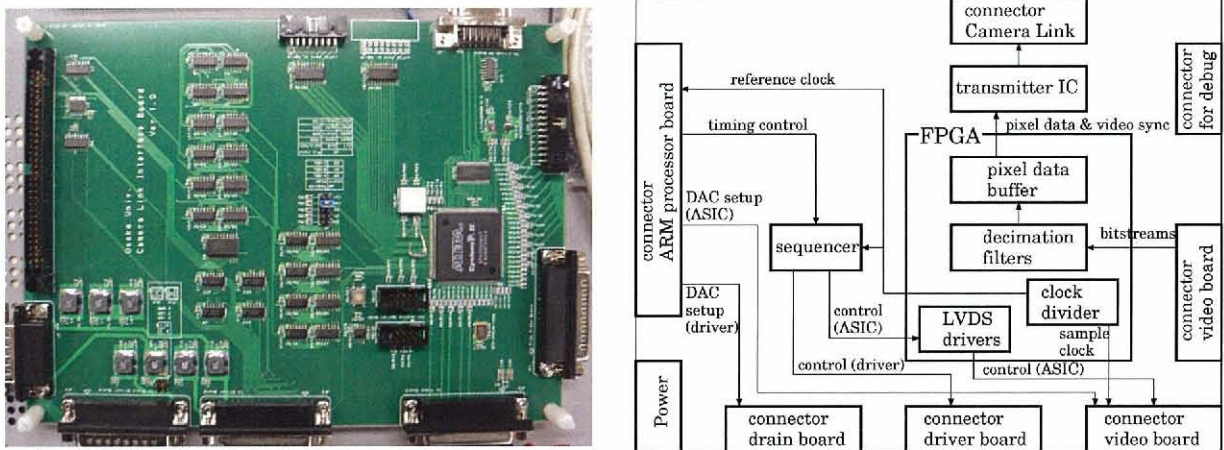


Figure 6.4: Photograph of the DE I/F board with the size of 23 cm×17 cm (left) and its block diagram(right).

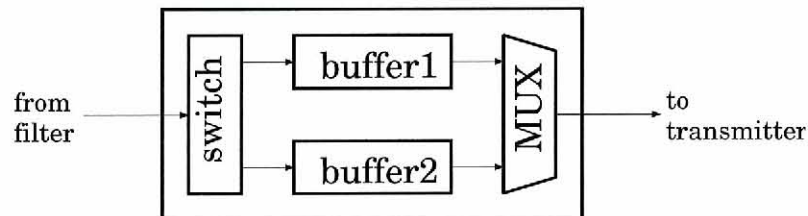


Figure 6.5: Block diagram of the pixel data buffer.

6.1.3 Driver, drain and video boards

Figure 6.6 shows photographs of the driver, drain and video boards. The driver and drain boards support the CCD drive signals shown in Table 6.1. They cover the signal range for the most CCD operation. We select the output voltage range for the drain voltage, OD and RD, with the types of CCDs, n-channel or p-channel CCDs. A CCD is considered as an array of a MOS capacitor. The mainly capacitance is the poly gate series oxide capacitance, depletion capacitance and poly-to-field oxide capacitance (Janesick, J. R. 2001). The effective capacitance of each signal line shown in Table 6.1 depends on the number of the derived pixel. The horizontal clock signals operate the pixels only in one horizontal row, while the vertical clock signals operate the pixels in whole imaging area. The effective capacitance of the vertical signal lines is significantly large compared with other lines. Since the clock driver circuits need to charge and discharge these capacitance during 1 pixel readout time, the high current capability is required especially for the drivers of the vertical transfer clocks. The power consumption for the charge transfer is

calculated by

$$P_R = N_{PH} C_{PIX} \Delta V_{CB}^2 f_c N_{PIX} \quad (6.1)$$

where P_R is the power, N_{PH} is the number of charge transfer phases, C_{PIX} is the capacitance per pixel per phase, ΔV_{CB} is the voltage swing of the transfer clock, f_c is the pixel rate and N_{PIX} is the number of pixels (Janesick, J. R. 2001). Assuming $N_{PH}=3$ phase, $C_{PIX}=18$ fF/pixel/phase, $\Delta V_{CB}=20$ V, $f_c=100$ kHz and $N_{PIX}=2000$ pixel \times 2000 pixel, the power of the vertical transfer driver is

$$P_R = 3 \times (18 \times 10^{-15}) \times 20^2 \times (100 \times 10^3) \times (2000 \times 2000) = 8.64 \text{ W}. \quad (6.2)$$

The required current capability for the vertical transfer clock is $\frac{8.64 \text{ W}}{20 \text{ V}} = 432$ mA in this condition. We designed the vertical clocks drivers with the current capability of ~ 1.8 A.

The CCD signals are processed by the ASIC mounting on the video board, and output the bitstream data to DE I/F board. The 3 boards, video, drain and driver boards, can be stacked as shown in Fig. 6.6 and placed in the vacuum chamber. The analog wire length between the CCD outputs and ASIC inputs can be minimized as much as possible, and the data handling between inside and outside the chamber is only digital signal, which suppresses the influence of the external noise.

6.2 Performance of C-link system

6.2.1 Unit testing

We, first, tested the readout system without CCDs. MD02 is mounted on the video board and all results in this Chapter are obtained by MD02. In this test, we made the histogram from the frame data and fit it with a Gaussian function. Figure 6.7 shows the equivalent input noise as a function of the pixel rate. The noise level of *C-link system* is equal to the test results in Fig. 4.7.

6.2.2 Test using an X-ray CCD

We evaluated the performance of *C-link system* by using Pch2k4k. Pch2k4k has the thick depletion layer of 200 μm and is the back-illuminated device. Since X-rays from ^{55}Fe are absorbed in the depletion layer of less than 100 μm , the signal charge cloud spreads during the drift from the interaction point to the potential well, and increase the split events. We cannot obtain the number of events enough to evaluate energy resolution by utilizing the grade method. Therefore, we operated the CCD in the 4 pixel \times 4 pixel sum-mode in

Table 6.1: Specification for the support signals of *C-link system*

Signal name	Function	Output voltage range
P1VI	vertical transfer clock (imaging area)	-10 V~10 V
P2VI	vertical transfer clock (imaging area)	-10 V~10 V
P3VI	vertical transfer clock (imaging area)	-10 V~10 V
P1VS	vertical transfer clock (storage area)	-10 V~10 V
P2VS	vertical transfer clock (storage area)	-10 V~10 V
P3VS	vertical transfer clock (storage area)	-10 V~10 V
P1H	horizontal transfer clock	-10 V~10 V
P2H	horizontal transfer clock	-10 V~10 V
SG	summing gate clock	-10 V~10 V
RG	gate clock of the reset transistor	-10 V~10 V
OG	output gate voltage (DC)	-10 V~10 V
RD	drain voltage of the reset transistor (DC)	-28 V~0 V or 0 V~30 V
OD	drain voltage of the output transistor (DC)	-28 V~0 V or 0 V~30 V
BB	back charging voltage (DC)	0 V~50 V

Chapter 5. However, the pixel sum-mode is not presently supported in C-link system. We irradiated the CCD with relatively high energy X-rays from ^{109}Cd , $\text{Ag } K\alpha = 22.1 \text{ keV}$ and $K\beta = 24.9 \text{ keV}$. Because the high energy X-rays is absorbed in a deep part of the depletion layer, the spread of the charge cloud is suppressed, and hence the ratio of the single events increases. Figure 6.8 shows the whole frame image and its closeup obtained by *C-link system*. We can clearly see X-ray events in Fig. 6.8 and confirm that the new system properly works.

The measured conversion factor of the CCD employed in this test is $4.5 (\mu\text{V}/e^-)$. The expected noise level at the pixel rate of 39 kHz is as

$$\text{ENC}_{\text{clink-pch}} = \frac{\text{Equivalent input noise } (\mu\text{V})}{\text{Conversion factor } (\mu\text{V}/e^-)} = \frac{37 (\mu\text{V})}{4.5 (\mu\text{V}/e^-)} \approx 8.2 e^-. \quad (6.3)$$

The measured ENC including the CCD is $9.9 e^-$ and the expected noise from the CCD is given by

$$\text{ENC}_{\text{clink-pch2k4k}} = \sqrt{(9.9 e^-)^2 - (8.2 e^-)^2} \approx 5.5 e^-. \quad (6.4)$$

The spectra of ^{109}Cd using the single pixel events is shown in Fig. 6.9. Note that there are 2 emission lines of yttrium (Y), $K\alpha=14.9 \text{ keV}$ and $K\beta=16.7 \text{ keV}$, derived from

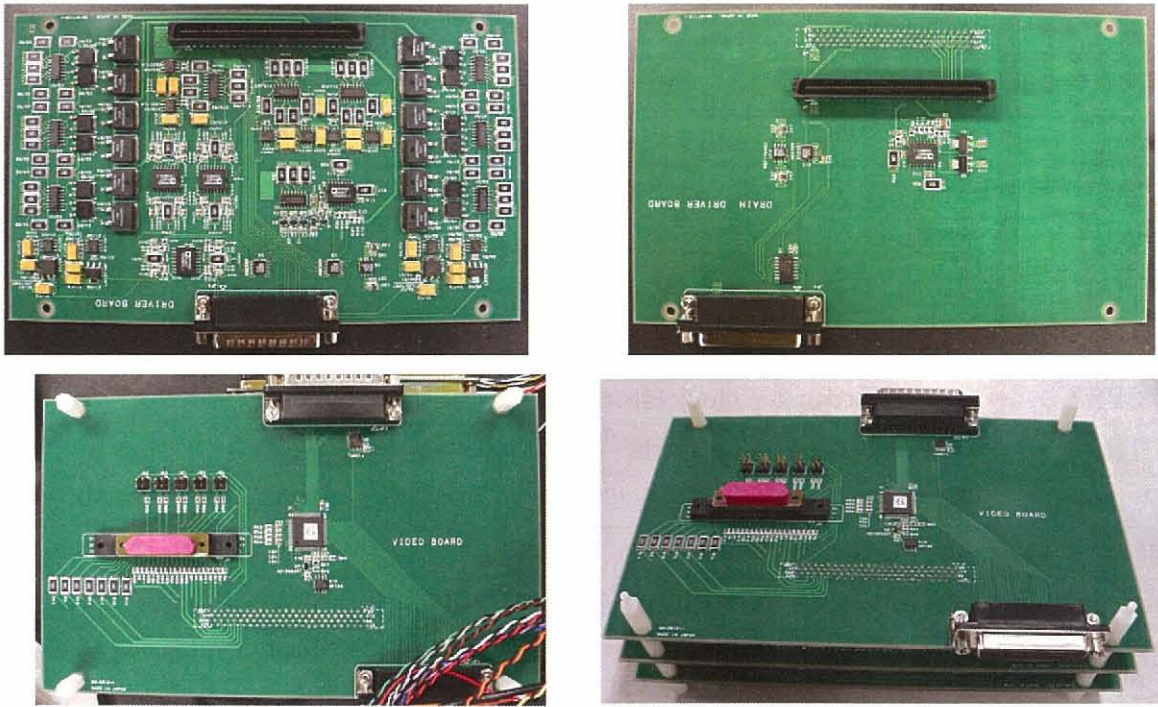


Figure 6.6: Photographs of the driver board (left top), drain board (right top), video board (left bottom) and stacked 3 boards (right bottom) with the size of $20\text{ cm(L)} \times 12\text{ cm(W)} \times 6\text{ cm(H)}$.

the bond used between the CCD device and its package. The test results are summarized in Table 6.2. The split threshold is 3 sigma of the readout noise level in these data analyses. The obtained energy resolution at 14.9 keV and 22.1 keV is 423 eV and 518 eV, respectively. *C-link system* properly drove an X-ray CCD with large imaging area, processed the CCD signals and acquired the frame data.

There are presently some problems in *C-link system*, such as the degradation of energy resolution, pixel sum-mode and high pixel rate operation. Figure 6.10 shows the comparison between the energy resolution obtained by *MiKE* system and that by *C-link system* at the readout noise of about 10 e^- . We are now investigating the cause for the degradation of the energy resolution. Additionally, we will test the readout of CCDs at the high frequency in the near future.

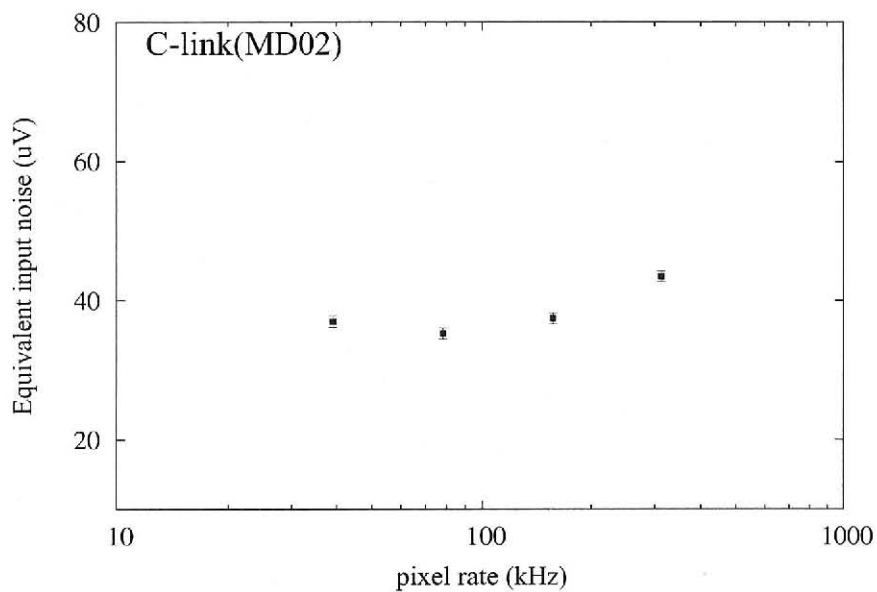


Figure 6.7: Equivalent input noise of *C-link* system without CCDs as a function the pixel rate.

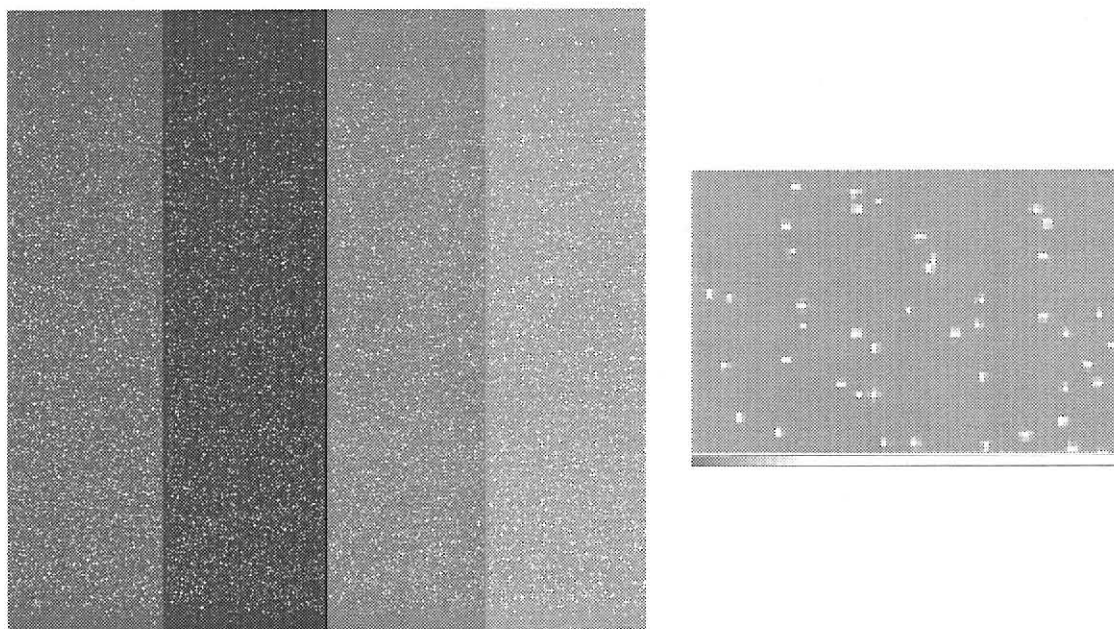


Figure 6.8: Whole frame image with the size of 2000 pixel \times 2000 pixel (left) and its partial closeup (right). White dots exhibit X-ray events in these figures.

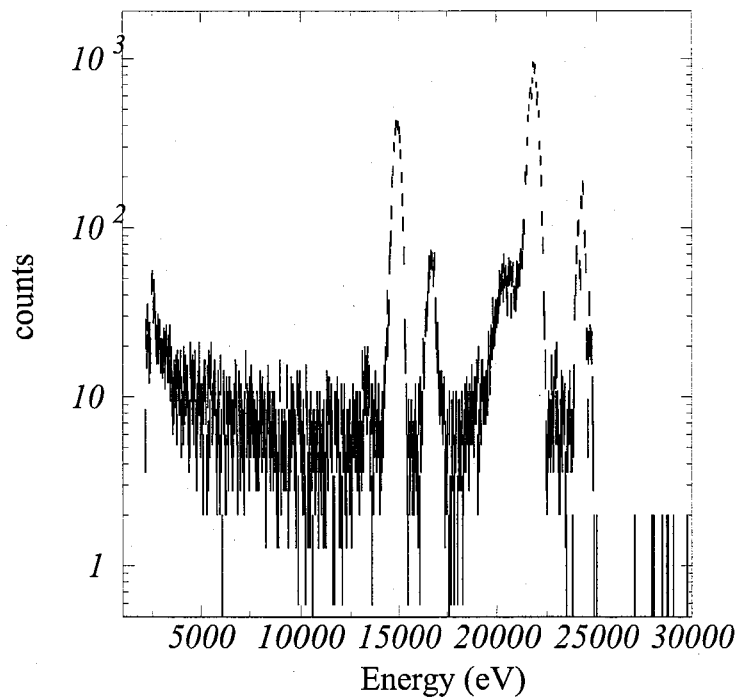


Figure 6.9: Spectrum (g0) of ^{109}Cd at the pixel rate of 39 kHz.

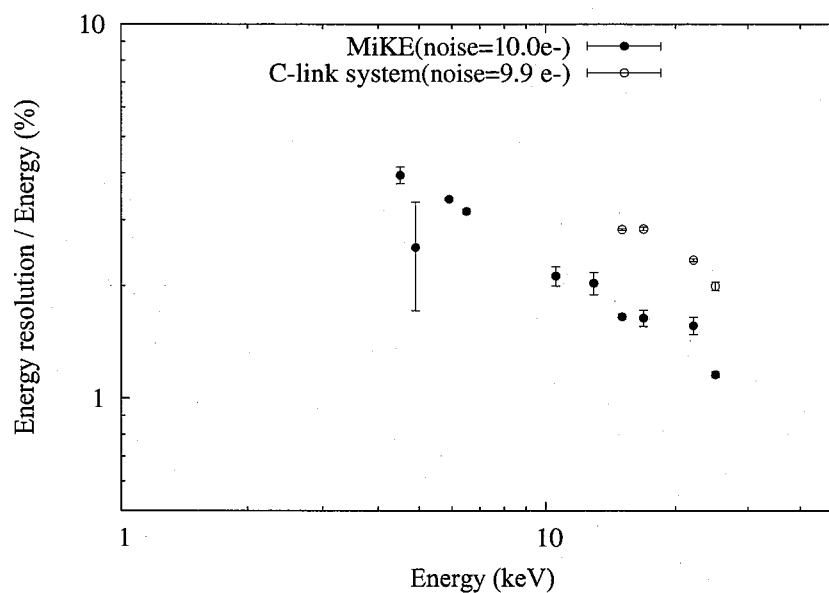


Figure 6.10: Comparison between the energy resolution by *MiKE* system and by *C-link* system at the readout noise of 10 e^- . The filled and open circles show the results of *MiKE* system and that of *C-link* system, respectively.

Table 6.2: Test condition and results by *C-link system*.

Operation temperature	-70°C
Pixel rate	39 kHz
ENC	$9.9 \pm 0.08 e^{-}$
Energy resolution [†] (Y K α :14.9 keV)	$423 \pm 2 \text{ eV}$
Energy resolution [†] (Y K β :16.7 keV)	$476 \pm 5 \text{ eV}$
Energy resolution [†] (Ag K α :22.1 keV)	$518.4 \pm 4 \text{ eV}$
Energy resolution [†] (Ag K β_1 :24.9 keV)	$499 \pm 13 \text{ eV}$

[†] Energy resolution (FWHM) using single events.

Chapter 7

Summary

The combination of an X-ray telescope and an X-ray CCD is the powerful tool for the observation in X-ray region, which is employed onboard the present X-ray astronomical satellites and produces excellent results. The X-ray CCDs significantly contribute to the progress of X-ray astronomy and will remain the standard detector for future missions.

The fabrication technology of the semiconductor is remarkably progressing in these years. We can develop the full-custom ASIC for the readout of X-ray CCDs by using the mixed-signal CMOS technology. The ASIC practically enables us to increase the number of the readout channels for high frame rate, and easily construct a CCD camera system under limitations of volume and power consumption onboard satellites. We fabricated ASICs with the size of $3\text{ mm} \times 3\text{ mm}$ by the TSMC $0.35\text{ }\mu\text{m}$ CMOS process. There are 4 readout channels in 1 chip. One channel is composed of a preamplifier, 5-bit DAC and $\Delta\Sigma$ ADC. We developed the new readout method for X-ray CCDs employing the $\Delta\Sigma$ ADC in our ASICs. This ADC functions not only as the ADC but also as the band-pass filter, which makes the circuit configuration relatively simple compared with the conventional systems. So far, we have fabricated 4 types of ASICs: MD01, MND01, MD02 and MND02. Their performances and problems are summarized in the following itemization.

1. MD01: The noise level is $42\text{ }\mu\text{V}$ and the power consumption is 79 mW at the pixel rate of 156 kHz . The input range is 40 mV and the INL is 0.2% . The maximum pixel rate is 156 kHz . The problems are the malfunction of the LVDS drivers and the low pixel rate, which is derived from the transistor without the NLDD region in the digital circuits.
2. MND01: The noise level is $48\text{ }\mu\text{V}$ and the power consumption is 89 mW at the pixel rate of 156 kHz . The input range is $20\text{ mV} \sim 200\text{ mV}$ and the INL is 1.2% . The maximum pixel rate is improved to be 625 kHz . The problems are the decrease of

the input range and the degradation of the noise level and the INL, which is derived from the ESD layer.

3. MD02: The noise level is $41 \mu\text{V}$ and the power consumption per chip is 92 mW at the pixel rate of 156 kHz . The input range is 40 mV and the INL is 0.2% . The maximum pixel rate is 625 kHz . We can confirm that all the fundamental problems have been solved.
4. MND02: We implemented the low noise operational amplifier in MND02. The noise level is $29 \mu\text{V}$ and the power consumption per chip is 168 mW at the pixel rate of 156 kHz . The input range is $40 \text{ mV} \sim 400 \text{ mV}$ and the INL is 0.2% . The maximum pixel rate is 625 kHz .

We are developing the SXI, X-ray CCD camera system for ASTRO-H. 2 types of X-ray CCDs for the SXI prototype models, called CCD-NeXT2 and Pch2k4k, presently have been developed. We evaluated the performance of the camera system using the ASIC (MD01) and these CCD devices. The readout noise and energy resolution (FWHM) at 5.9 keV were $7.5 e^-$ and 150 eV (g_0) at the pixel rate of 40 kHz when using Pch2k4k. Since the noise from the ASIC was dominant in the total readout noise, we simultaneously processed one CCD signal by separate 4 channels and obtained their average to reduce the noise component from the ASIC by half. This fact indicates that four channels in one chip are completely independent of each other, indicating the proper design of the analog circuit. In this readout method, we achieved the readout noise and energy resolution (FWHM) at 5.9 keV were $5.3 e^-$ and 140 eV (g_0) at the pixel rate of 40 kHz , respectively. We are now preparing the test setup for MND02 and expect to achieve the readout noise of a few electrons.

ASTRO-H will be launched into the low earth orbit of 550 km . The devices onboard the satellite will be mainly damaged by protons during the passage of the SAA. Therefore, we tested the TID effect of the ASIC (MD01) by using a 200 MeV proton beam at HIMAC. The indication of the radiation damage did not appear at the TID of up to 17 krad . Additionally, all function was recovered after the annealing at the room temperature. Through the test results, we can verify that the ASIC (MD01) surrounded by Al with the thickness of 1 mm meets the radiation tolerance in space required for ASTRO-H.

We are developing the new X-ray CCD camera system (*C-link system*) utilizing the ASIC and the Camera Link to realize the multi-readout of CCD signals at the high pixel rate. We obtained the proper frame image and spectrum at the pixel rate of 40 kHz . The readout noise and energy resolution (FWHM) at 22.1 keV are $9.9 e^-$ and 518 eV (g_0), respectively. We will test the readout of the CCD by *C-link system* at the high frequency

of more than 100 kHz in near future. We expect that the *C-link system* enables anyone to easily construct the compact readout system for X-ray CCDs with low noise and high pixel rate.

Acknowledgments

First of all, I sincerely thank to Prof. H.Tsunemi for giving me an excellent subject of research, an development of ASICs, and his continuous guidance. I thank to Prof. K.Hayashida and Dr. K.Torii for their useful advice in meetings and supports at the ground calibration of the XIS. I could see and test the FM model of the XIS, which is a valuable experience in my graduate period. I am grateful to Dr. E.Miyata for her technical supports of X-ray CCD experiments. These experiences were very useful in the development of ASICs. Dr. N.Anabuki supported me with the designs of VHDL and software in experiments. Dr. H.Nakajima helped me through the ASIC developments and checked my papers. Dr. H.Ozawa commented on my test results and gave me improvement plans. Dr. M.Namiki held a seminar for data analyses of X-ray astronomy. This was a valuable opportunity for me. They often took me out for drink, which made me feel relaxed. I wish to thank all of members in X-ray Astronomy Group in Osaka University.

I would like to thank to N.Kitamura, T.Mitani and T.Takashima for their technical supports at the radiation test of the ASIC in HIMAC/NIRS. The source data of figures 4.19 and 4.20 are by courtesy of JAXA Space Environment Group.

I especially thank to collaborators of Drs. J.P.Doty and H.Ikeda. Dr. J.P.Doty is a worldwide specialist for X-ray CCD camera systems. It is a great experience that I could develop the ASICs with him. Dr. H.Ikeda taught me a basics of CMOS circuits and a SPICE simulation, and also advised me as to what I should do in the experiments and data analyses through the graduate period. Additionally, OPEN IP that is implemented in our ASICs is designed by him. My research can't be successful without their collaboration.

This study was also carried out as part of the 21st Century COE Program, '*Towards a new basic science: depth and synthesis*'. I am supported by JSPS Research Fellowship for Young Scientists.

I would like to show my deepest appreciation for my family. Finally, I hope for a great success of ASTRO-H especially for the SXI.

February 2, 2009 Daiuske Matsuura

References

ASCA web page, <http://heasarc.gsfc.nasa.gov/docs/asca/>

Bookbinder, J. et al. 2008, Proc. SPIE, 7011, 2B

Camera Link spec, http://www.qmt.ch/_library/cameralink_specifications.1.1.pdf

CFITIO web page, <http://heasarc.nasa.gov/lheasoft/fitsio/fitsio.html>

comedi web page, <http://www.comedi.org/>

Cyber Shuttle web page, <http://www.toptdc.com/tsmc/index.html>

Digian web page, <http://www.digian.co.jp/>

Doty, J. P. 2006a, US patent application serial number 11/307435, international patent application serial number PCT/US2006/004330

Doty, J.P. et al. 2006b, Proc. SPIE, 6276, 62761P

gEDE web page, <http://www.geda.seul.org/>

Garmire, G.P. et al. 2003, Proc. SPIE, 4851, 28

Herrmann, S. et al. 2007, NSS '07, IEEE, 3, 2398

Hiraga, J. 2002, PHD thesis, Osaka University

Inose, H. et al. 1962 IRE Trans. on Space Electronics and Telemetry, 8, 204

Janesick, J. R. 2001, SPIE PRESS

Karcher, A. et al. 2007, NSS '07, IEEE, 2, 1069

Koyama, K. et al. 2007a, PASJ, 59, 23

LSE64 web page, <http://www.noqsi.com/images/lse64-0.3.zip>

- Matsuura, D. et al. 2006a, Proc. SPIE, 6276, 627612
- Matsuura, D. et al. 2006b, JJAP, 45, 8904
- Matsuura, D. et al. 2007, Nucl. Instr. and Meth. A, A570, 140
- Matsushita, T. et al. 1995, Nucl. Instr. and Meth. A, 336, 336
- Mitsuda, K. et al. 2007, PASJ, 59, 1
- Miyata, E. et al. 2006, Nucl. Instr. and Meth. A, 568, 149
- Miyata, E. et al. 2001, Nucl. Instr. and Meth. A, 459, 157
- Nakaya, H. et al. 2008, Proc. SPIE, 7014, 70144X
- MOSIS web page, <http://www.mosis.com/>
- Nakajima, H. et al. 2008, IEEE Press, now submitted
- Open IP web page, <http://research.kek.jp/people/ikeda/openIP/>
- Parmar, A. et al. 2006, Proc. SPIE, 6266, 50P
- Rainey, P.M. 1921, U.S. Patent 1, 608, 527
- Richard, S. et al. 2005, IEEE Press
- Strüder, L. et al. 2001, A&A, 365, 18
- SUN-S web page, <http://www.sun-s.jp/>
- Takahashi, T. et al. 2008, Proc. SPIE, 7011, 70110O
- Tanaka, Y. et al. 1994, PASJ, 46, 37
- TSMC web page, <http://www.mosis.com/products/fab/vendors/tsmc/tsmc035/>
- Tsunemi, H. et al. 2007, Nucl. Instr. and Meth. A, 579, 866
- Tsunemi, H. et al. 2008, Proc. SPIE, 7011, 70110Q
- Turner, M.L.J. et al. 2001, A&A, 365, 27
- Yamashita, A. et al. 1997, IEEE Trans. Nucl. Sci, 44, 847
- Yamashita, A. et al. 1999 Nucl. Instr. and Meth. A, 436, 68
- Yokoyama, M. et al. 2001, IEEE Trans. Nucl. Sci., 48, 440

